Politecnico di Milano
Department of Energy
Doctoral Programme in
Energy and Nuclear Science and Technology

Nanostructured Transparent Conducting Oxides for Advanced Photovoltaic Applications

Doctoral Dissertation of:
Paolo Gondoni

Supervisors:
Dr. Carlo S. Casari
Prof. Andrea Li Bassi

Tutor and Chair of the Doctoral Programme:
Prof. Carlo E. Bottani

Year 2014 – Cycle XXVI

And so each venture
Is a new beginning, a raid on the inarticulate
With shabby equipment always deteriorating
In the general mess of imprecision of feeling,
Undisciplined squads of emotion. And what there is to conquer
By strength and submission, has already been discovered
Once or twice, or several times, by men whom one cannot hope
To emulate - but there is no competition -
There is only the fight to recover what has been lost
And found and lost again and again: and now, under conditions
That seem unpropitious. But perhaps neither gain nor loss.
For us, there is only the trying. The rest is not our business.

— T. S. Eliot, *East Coker*, *Four Quartets*

Abstract

Transparent electrodes are a key component in new photovoltaic devices. With the development of organic and hybrid solar cells, electrical conductivity and optical transparency of transparent electrodes must be accompanied by other functionalities, such as large surface area, effective light management, preferential charge transport directions, mechanical flexibility and compatibility with polymer substrates. This work describes the investigation of the structure/property relation in nanostructured Al-doped ZnO (AZO), with the aim of obtaining multifunctional AZO transparent electrodes by room temperature Pulsed Laser Deposition, with the functional properties mentioned above.

By a deep investigation of the structure/property relation in AZO with different morphologies, state-of-the-art compact transparent conducting films and mesoporous forest-like hierarchically assembled layers, optimal for light scattering and trapping, were obtained at room temperature. The properties of interest were combined by two independent approaches, leading to the synthesis of electrically conducting AZO nano-forests and functionally graded architectures, which were tested to demonstrate a significant improvement in light harvesting for of organic photovoltaic applications.

Premessa

Gli elettrodi trasparenti sono un componente fondamentale dei dispositivi fotovoltaici di nuova generazione. Con l'avvento delle celle solari organiche e ibride, la conducibilità elettrica e la trasparenza alla luce visibile non sono più sufficienti, ma devono essere accompagnate da altre proprietà particolari, come un'elevata area superficiale, la capacità di intrappolare la luce, la presenza di direzioni di trasporto preferenziali per le cariche, la flessibilità e la compatibilità con substrati polimerici. Questo lavoro descrive lo studio della relazione struttura/proprietà in film nanostrutturati di ossido di zinco drogato con alluminio (AZO), per ottenere elettrodi trasparenti multifunzionali sintetizzati a temperatura ambiente mediante ablazione a laser pulsato, con le proprietà funzionali sopra elencate.

Attraverso un'indagine approfondita della relazione tra struttura e proprietà in film di AZO con diversa morfologia, sono stati ottenuti conduttori trasparenti compatti con proprietà allo stato dell'arte, e film mesoporosi con una struttura gerarchica a forma di foresta che garantisce la diffusione e l'intrappolamento della luce. La possibilità di combinare le proprietà d'interesse è stata ottenuta attraverso due approcci indipendenti, che hanno condotto allo sviluppo di nano-foreste conduttive di AZO e di architetture con variazioni graduali di morfologia, che sono state testate ottenendo un aumento significativo dell'efficienza di raccolta della luce solare per applicazioni ai dispositivi fotovoltaici organici.

Contents

Introduction

The last centuries have been characterized by an unprecedented increase of energy consumption, due to worldwide technological innovations and a rapid demographic expansion of the world population. The urgency of replacing fossil fuels such as oil and coal has become critical, leading the world of research to a fast development of efficient solutions, many of which are based on renewable sources. Harvesting energy from the sun, the oceans, the wind etc. is a complex matter, raising a number of technological issues related to the development of functional materials which need of course be preferably inexpensive, abundant and nontoxic.

The field of solar energy devices, in particular, is in constant evolution and conventional bulk Si-based PhotoVoltaic (PV) cells and modules are going to be replaced by low cost solutions with novel properties of interest, e.g. mechanical flexibility, capability of harvesting sunlight from different directions, compatibility with inexpensive, polymer-based substrates. In this new class of devices, mainly constituted by thin film, organic and hybrid solar cells, a component of primary importance is constituted by transparent electrodes. The basic role played by a transparent electrode is to let the solar light get through to the device active medium (which requires visible transparency) and, at the same time, to let the photogenerated charges exit the device to an external circuit (which requires electrical conductivity). The development of performing transparent conductors has been pursued and achieved over the last 2-3 decades, leading to the wide employment of compact thin films of Transparent Conducting Oxides (TCOs).

In general, TCOs are a class of materials based on wide bandgap (> 3 eV) metal

oxides, which become good electrical conductors upon degenerate doping (usually n-type) which fills their conduction band with nearly free electrons. Within this class, Indium-Tin Oxide (ITO) was soon identified as the most performing and brought to application at an industrial scale. However, indium is a scarce and expensive material, whose processing is not environmental friendly: this makes ITO unfit to carry on as a long-term lead material for TCO applications. Among the possible replacements for ITO, Al-doped Zinc Oxide (AZO) stands out as a low cost, abundant and highly performing candidate.

Compact AZO as a conventional TCO layer is now widely available, with optical transparency and electrical conductivity which are not far from reaching ITO-like values. However, the development of novel PV devices, as anticipated above, makes these basic TCO properties insufficient to cover the emerging needs. Several peculiar requirements must be met, both in terms of synthesis process and of functional properties: first, the compatibility with flexible devices and polymer-based substrates demands low temperature synthesis and processing. This is a non-standard requirement, cutting out the majority of synthesis techniques conventionally employed for TCO layers. Second, effective light management and trapping is hard to achieve in standard compact TCOs, suggesting that flat-surface films should be replaced by complex, 3-d morphologies. Another peculiarity connected with the development of new generation PV devices is the criticality of maximizing interfaces by increasing the surface-to-volume ratio, e.g. with the development of porous structures. Furthermore, in all thin-film, organic and hybrid PV devices, the identification and control of a preferential charge transport direction can positively affect the performance of transparent electrodes: this is the case with novel ordered hierarchical structures, whose synthesis requires a deep understanding of the modification of properties when moving to the micro- and nanoscale. This is in general a challenge for physics and nanotechnology, pointing at the understanding of the structure/property relation in nanostructured materials as one of the goals to pursue for the development of novel functional materials.

In this context, the main subject of this work is the development of nanostructured AZO layers to be employed as multifunctional transparent electrodes in novel PV devices. This is done by exploring the structure/property relation in strongly diversified AZO thin films, synthesized at room temperature with a variety of structures and morphologies. The synthesis technique of choice to perform this exploration is Pulsed Laser Deposition (PLD), whose versatility

allows to easily span across different deposition regimes - from conventional compact layers to complex, 3-d structured hierarchical morphologies - and to achieve control of the chemical composition and local properties down to the nanoscale. The identification of the means to achieve control of structural and functional properties will then be used as a starting point for the development of multifunctional AZO layers to meet the requirements listed above.

This work is structured in three parts according to the following scheme: Part I reviews the physics and state of the art of transparent electrodes in general (chapter 1) and of AZO specifically (chapter 2). Part II presents the investigation of the structure/property relation in nanostructured AZO grown by room temperature PLD (chapter 4), preceded by a description of the experimental techniques (chapter 3) employed for synthesis and characterization. In Part III, the results of this investigation are used to develop two approaches for the fabrication of multifunctional, large surface area, nanostructured AZO layers by achieving separate control of functional properties through chemical (chapter 5) or spatial (chapter 6) separation.

The experimental part of this work, i.e. synthesis and characterization of AZO layers, was personally carried out by the author, with the exception of X-Ray Diffraction (for which Dr. Javier Martí-Rujas at the Italian Institute of Technology, Milano, is to be acknowledged), Raman spectroscopy (provided by Dr. Valeria Russo, Politecnico di Milano) and micromanipulator-based electrical measurements (performed by Dr. Gian Carlo Gazzadi and Dr. Valentina De Renzi, University of Modena and Reggio Emilia).

The original contents of this PhD thesis have led to the publication of the following peer-reviewed papers, ordered by year:

- P. Gondoni, M. Ghidelli, F. Di Fonzo, V. Russo, P. Bruno, J. Martí-Rujas, C. E. Bottani, A. Li Bassi, and C. S. Casari, Structural and functional properties of Al:ZnO thin films grown by Pulsed Laser Deposition at room temperature, *Thin Solid Films* 520 (14), 4707-4711, 2012 (with data from chapter 4)

- P. Gondoni, M. Ghidelli, F. Di Fonzo, M. Carminati, V. Russo, C. E. Bottani, A. Li Bassi, C. S. Casari, Structure-dependent optical and electrical transport properties of nanostructured Al-doped ZnO, *Nanotechnology* 23, 365706, 2012 (with data from chapter 4)

- P. Gondoni, M. Ghidelli, F. Di Fonzo, V. Russo, P. Bruno, J. Martí-Rujas, C.E. Bottani, A. Li Bassi, C.S. Casari, Highly Performing Al:ZnO Thin Films Grown by Pulsed Laser Deposition at Room Temperature, *Nanoscience and Nanotechnology Letters* 5 (4), 484-486, 2013 (with data from chapters 4 and 6)

- P. Gondoni, M. Ghidelli, F. Di Fonzo, A. Li Bassi, C.S. Casari, Fabrication of nano-engineered transparent conducting oxides by Pulsed Laser Deposition, *Journal of Visualized Experiments* 72, e50297, 1-7, 2013 (with detailed descriptions of the experimental procedures employed in chapters 4 - 6)

- P. Gondoni, V. Russo, C.E. Bottani, A. Li Bassi, C.S. Casari, Tuning Hierarchical Cluster Assembly in Pulsed Laser Deposition of Al-doped ZnO, *Materials Research Society Symposium Proceedings 1497*, doi: 10.1557/opl.2013.329, 2013 (with data from chapter 4)

- V. Russo, M. Ghidelli, P. Gondoni, C. S. Casari and A. Li Bassi, Multi-wavelength Raman scattering of nanostructured Al-doped zinc oxide, *Journal of Applied Physics* 115 (7), 073508, 2014 (with data from chapter 4)

- P. Gondoni, P. Mazzolini, A. M. Pillado Pérez, V. Russo, A. Li Bassi, C. S. Casari, Morphology-driven electrical and optical properties in graded hierarchical transparent conducting Al:ZnO, *Materials Research Society Symposium Proceedings* 1699E., in press, 2014 (with data from chapter 6)
- P. Gondoni, P. Mazzolini, V. Russo, A. Petrozza, A. K. Srivastava, A. Li Bassi, C. S. Casari, Enhancing Light Harvesting by Hierarchical Functionally Graded Transparent Conducting Al-doped ZnO Nano- and Mesoarchitectures, *Solar Energy Materials and Solar Cells* 128, 248-253, 2014 (with data from chapter 6)
- P. Gondoni, P. Mazzolini, V. Russo, M. Diani, M. Amati, L. Gregoratti, V. De Renzi, G. C. Gazzadi, J. Martí-Rujas, A. Li Bassi, C. S. Casari, Tuning electrical and optical properties of hierarchically assembled Al-doped ZnO nanoforests by room temperature Pulsed Laser Deposition, *Semiconductor Science and Technology*, in preparation (with data from chapter 5)

and to the following presentations at international conferences:

- EMRS11 - European Materials Research Society Spring Meeting - May 9-13, 2011. Nice, France.
  Contribution type: Poster
  Title: Structural and functional properties of Al:ZnO thin films grown by Pulsed Laser Deposition at room temperature
- NN11 - International Conference on Nanosciences and Nanotechnologies - July 12-15, 2011. Thessaloniki, Greece.
  Contribution type: Poster
  Title: Nanoengineering of Al:ZnO Films by Pulsed Laser Deposition at Room Temperature for Photovoltaic Applications
- ICSFS16 - International Conference on Solid Films and Surfaces - July 1-6, 2012. Genova, Italy.
  Contribution type: Oral
  Title: Pulsed Laser Deposition of Al-doped ZnO: from compact films to nano-forests
- TCM2012 - International Symposium on Transparent Conducting Materials - October 21-26, 2012. Heraklion, Greece.
  Contribution type: Oral

Title: Nano- and mesoporous Al-doped ZnO grown by Pulsed Laser Deposition at room temperature

- MRS12 - Materials Research Society Fall Meeting - November 25-30, 2012. Boston, USA. Contribution type: Oral
  Title: Hierarchically assembled Al:ZnO nano-forests by Pulsed Laser Deposition for photovoltaic applications

- EMN12 - Energy Materials Nanotechnology Fall Meeting - November 30-Dec 2, 2012. Las Vegas, USA.
  Contribution type: Invited Oral
  Title: Hierarchically assembled Al-doped ZnO Grown by Pulsed Laser Deposition for Photovoltaic Applications

- FISMAT - Italian National Conference on Condensed Matter Physics - September 9-13, 2013. Milano, Italy
  Contribution type: Oral
  Title: Nanostructured Al-doped ZnO grown by Pulsed Laser Deposition as a Transparent Conducting Oxide for Advanced Photovoltaics

- JSAP13 - Japanese Society of Applied Physics and Material Research Society Joint Symposia - September 15-20, 2013. Kyoto, Japan.
  Contribution type: Oral
  Title: High Haze Transparent Conducting Al-doped ZnO: Nano- and Mesoscale Design by Pulsed Laser Deposition

- MRS14 - Materials Research Society Spring Meeting - April 21-25, 2014. San Francisco, USA
  Contribution type: Poster
  Title: High haze transparent conducting Al-doped ZnO: towards nanoscale design of flexible scattering electrodes

- CIMTEC14 - 6th Forum on New Materials - June 15-19, 2014. Montecatini Terme, Italy
  Contribution type: Oral
  Title: Nano- and mesoscale engineering of Al-doped ZnO by Pulsed Laser Deposition: towards flexible scattering electrodes

Part I

Transparent electrodes for photovoltaics

1

Transparent Conducting Oxides and related materials

RENEWABLE sources are required to increase their contribution to the ever-growing amount of world energy consumption, which is expected to rise from 13 TW-Year to 30 TW-Year by 2050 [1]. Since the amount of irradiated power by the sun which reaches the whole earth surface on a sunny day is of the order of 100 PW [2], PhotoVoltaic (PV) systems are expected to be significant contributors to help meet this requirement. A crucial element in the majority of PV devices is constituted by the top electrode, which must be simultaneously transparent to let the sunlight reach the active material and electrically conducting in order to allow the photogenerated charges exit to an external circuit [3]. In terms of basic semiconductors physics, the properties of optical transparency in the visible range and of electrical conductivity seem to contradict each other: in fact, such properties lead to opposite requirements in terms of bandgap, which must be large to avoid visible light absorption and small to allow the filling of the conduction band [4]. However, the phenomenon of electrical conductivity in metal oxides was first reported as early as in 1907 [5], for CdO. It was almost one century later, though, that the field of Transparent Conducting Oxides (TCOs) was brought to the spotlight of research on transparent contacts for optoelectronic and energy conversion devices [6]. This boost was significantly influenced by the discovery and optimization of the outstanding optical and electrical properties of what is still today the most widely employed transparent conductor, i.e. Indium-Tin Oxide (ITO) [7–9]. This material, constituted by a solid solution of SnO_2 in In_2O_3, has been optimized to have an electrical resistivity lower than $10^{-4}\ \Omega\,\mathrm{cm}$, that is to say less than

2 orders of magnitude higher than most bulk metals [10]. The scarcity and uncontrollable price of indium [11] have raised the need to develop alternative, In-free materials [12], following the increasing interest of research in transparent contacts for flat panel displays, low emissivity coatings, thin film transistors and PV devices. This has led to the development and study of several other TCOs, based on doped ZnO, SnO_2, TiO_2 and ternary/quaternary compounds [13–15]. All these doped metal oxide-based TCOs are n-type materials, i.e. their doping is achieved by filling the conduction band with electrons, while p-type TCOs are still far from application [16, 17] due to an extremely earlier degree of optimization of functional properties. More recently, new strategies have been explored to obtain performing transparent electrodes, the most successful being the development of amorphous TCOs [17, 18] and non-TCO based transparent electrodes (e.g. metal nanowire networks or graphene layers) [19, 20].

In such a wide and rapidly evolving field, the present section reviews the physical principles, state of the art, requirement and challenges for transparent electrodes, focusing on TCOs for PV devices. In particular, section 1.1 describes the basic physics of TCO materials, section 1.2 reviews the state of the art of TCOs and other transparent electrodes, section 1.3 focuses on the main requirements and challenges for application in organic and hybrid PV devices.

1.1 Basic physics of TCOs

1.1.1 Optical properties

The class of TCO materials is, in general, constituted by wide bandgap (i.e., transparent) metal oxides which are intrinsically or extrinsically doped in order to achieve electrical conductivity. In principle, the oxide bandgap must be sufficiently large (i.e. greater than 3 eV) to avoid visible light absorption, and the doping level must be sufficiently high to allow electrical conduction [21, 22].

Due to their large bandgap and high free carrier concentration, the optical properties of TCOs are typically characterized by a so-called window of optical transparency, which is limited at high photon energies (greater than the optical gap) by interband transitions, and at low photon energies (lower than the plasma energy) by free carrier absorption. To understand the complex interplay between optical and electrical properties, one must first note that both the optical gap and the plasma energy are directly influenced by charge carrier concentration [23]. In particular, the minimum photon energy to promote interband transitions (optical gap) is increased in heavily doped semiconductors (if the Fermi level is above the conduction band minimum [1] by the Moss-Burstein (MB) effect [24]. This effect is a direct consequence of the Pauli exclusion principle, which forbids transitions from the valence band maximum to the conduction band minimum (i.e. with energy equal to the bandgap) if the bottom of the conduction band is occupied. As a consequence, the minimum photon energy for an optical transition is increased proportionally to the filling of the conduction band, as can be seen from figure 1.1.a-b. In a simple free-electron model, the minimum energy interband transition occurs at the Fermi wave vector and the corresponding increase in the optical gap is proportional to the Fermi energy, according to the following relation:

$$\Delta E_g^{MB} = \frac{\hbar^2}{2m^*}\left(3\pi^2 n\right)^{\frac{2}{3}} \tag{1.1}$$

where ΔE_g is the increase in optical gap, n is the electron density and m^* is the reduced effective mass for the interband transition, defined as the reciprocal of the inverse sum of the effective masses of the hole and the electron, i.e.

$$\frac{1}{m^*} = \frac{1}{m_e^*} + \frac{1}{m_h^*} \tag{1.2}$$

[1] In this whole section, optical and electrical properties will be described referring to n-type semiconductors, in which charge carriers are electrons in the conduction band, rather than p-type materials in which electrical current is carried by holes in the valence band. The physical processes described here are equally valid for p-type semiconductors, but the field of TCOs is presently dominated by n-type. Some examples of p-type TCOs can be found in section 1.2

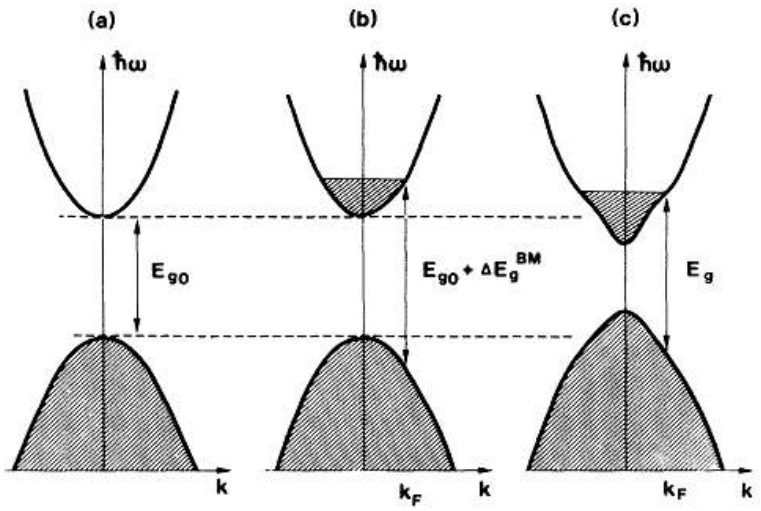

Figure 1.1: *(a) Schematic band structure of a direct gap semiconductor with parabolic bands separated by E_g^0. (b) Increase in optical gap by an amount ΔEg^{MB} upon heavy doping. (c) Perturbed band structure and resulting optical gap E_g as a consequence of many-body effects. (Shaded areas denote occupied states, k_F represents the Fermi wave vector. This picture is taken from ref. [25])*

This increase in the optical gap (i.e. in the near UV transparency) with increasing carrier concentration is beneficial for a TCO. However, if n is too high, other effects (mainly many-body type interactions) come into play which lead to a distortion of the band shape (nonparabolicity) and a shrinkage of the bandgap [25–27]. A scheme of these effects is shown in figure 1.1.c. The second limit to optical transparency in a TCO, manifesting itself at low photon energies, is constituted by free carrier absorption. If the bottom of the conduction band is partly filled as hypothesized above, the conduction electrons will form a Drude-like free electron gas, which can absorb electromagnetic radiation to sustain collective plasma oscillations at its resonance frequency [28]:

$$\omega_p = \sqrt{\frac{nq^2}{m_c^* \varepsilon_0 \varepsilon_\infty}} \tag{1.3}$$

where q is the electron charge, m_c^* is the electron conduction band effective mass, and ε_∞ the high-frequency dielectric permittivity. Since this plasma frequency constitutes the *lower* limit to the optical transparency window, eq. 1.3 shows why the doping level in TCOs cannot be increased arbitrarily without narrowing the transparency window to a smaller spectral range [29]. Furthermore, the absorption intensity is also increased at higher carrier densities: the combination

of the spectral and intensity dependence of plasma absorption (which for TCOs typically occurs in the near IR) can be seen in figure 1.2. In this graph, which

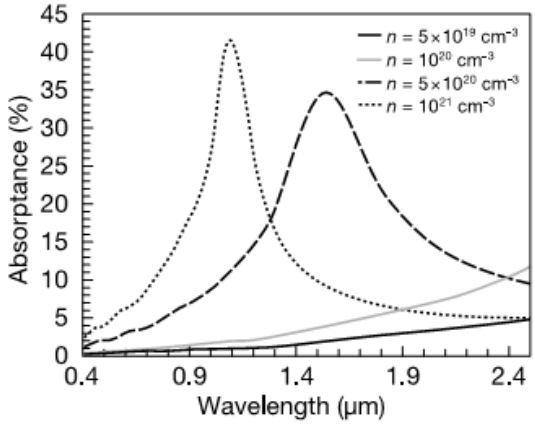

Figure 1.2: *Calculated near-infrared absorptance spectra of TCOs with different carrier concentrations. (Taken from ref. [28])*

reports calculated absorption profiles, the plasma peaks are shifting towards lower wavelengths with increasing carrier concentration, and the peak heights increase accordingly. This results in a shrinkage of the TCO transparency window at the high wavelength side, competing with the UV increase dictated by eq. 1.1. The result of these competing effects can be evaluated by looking at the full modeled spectra reported in figure 1.3 [8], where the optical transmittance spectra have been calculated for ITO thin films with different carrier concentrations. What can be noted from the figure is the different weight of the Moss-Burstein effect and the plasma onset in determining the width of the transparency window: this is due to the different multiplying coefficients in eqs. 1.1 and 1.3, and it allows to point out that if n is too high, the drawbacks of decreasing the plasma wavelength significantly overcome the advantages of increasing the optical gap [10].

Within the transparency window, which is usually slightly wider than the visible light spectral range for these reasons, the optical transmittance value of a TCO film is generally influenced by two main factors: the presence of intragap states, which mainly influences the mean value [30], and the interference fringes due to interfacial reflections, which mainly influence the spectral profile [31]. The role of defects in creating intragap states in TCOs has been widely studied by theoretical works over the last years [30, 32–38], which pointed out an extremely complex dependence of midgap states on point defects for known TCO materials. The overall description of TCO band structure and their modification by point

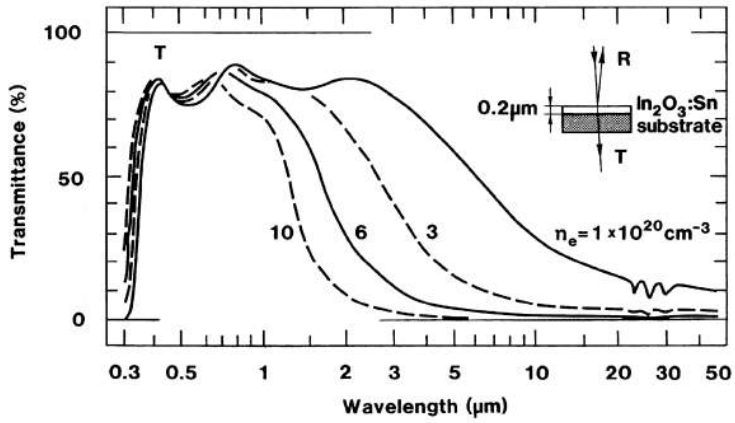

Figure 1.3: *Calculated transmittance spectra for ITO thin films with different carrier concentration values. Taken from ref. [10]*

defects is way beyond the scope of this work, and several issues are still open, but one point of agreement for theoreticians is significant for what will be discussed later: oxygen vacancies in ZnO-, In_2O_3- and SnO_2-based TCOs create available optical transitions with energy lower than the optical gap, and therefore decrease transparency in the visible range. Metal cation vacancies and interstitials are in general characterized by higher formation energies [33,35,36] and are therefore less easily formed, but they can contribute to the decrease of optical transmittance by creating defect states. Grain boundaries in polycrystalline TCOs can lead to the formation of deep states close to the valence band maximum if dangling bonds are present, but this effect can be compensated by O vacancies, which at any rate create shallower states and absorption at higher wavelengths [38]. Another defect-related phenomenon typical of heavily doped semiconductors occurs in the region close to the optical gap, i.e. the presence of an absorption edge with a logarithmic shape known as an Urbach tail [39]. Rather than briskly dropping to zero as predicted by basic semiconductor theory [21], the absorption coefficient at energies slightly lower than the optical gap shows a tail, i.e. a region of non-zero absorption, whose exact origin is still unclear but it has been repeatedly correlated with structural disorder [40, 41].

1.1.2 Electrical properties

As anticipated in the previous section, electrical conductivity in TCOs is caused by the heavy doping levels which allow the filling of the conduction band in spite of the large bandgap. However, the actual mechanism behind this filling process

is far from being fully understood still today [42]. In fact, the role of intrinsic and extrinsic dopants has not been fully clarified yet, and significant discrepancies still exist between theoretical predictions and experimental results in terms of electrical properties [43, 44]. In this section, a simplified picture for conductivity in TCOs will be given, then some of the open issues will be addressed in more detail, for the specific case of ZnO-based materials, in chapter 2.

To understand the insurgence of electrical conductivity as a consequence of heavy doping, the band composition of ITO can be considered as an example. Figure 1.4 shows a scheme of the energy bands of ITO in different doping conditions, i.e. $In_{2-x}Sn_xO_3$:In_2O_{3-x} for different x values [45]. This definition of

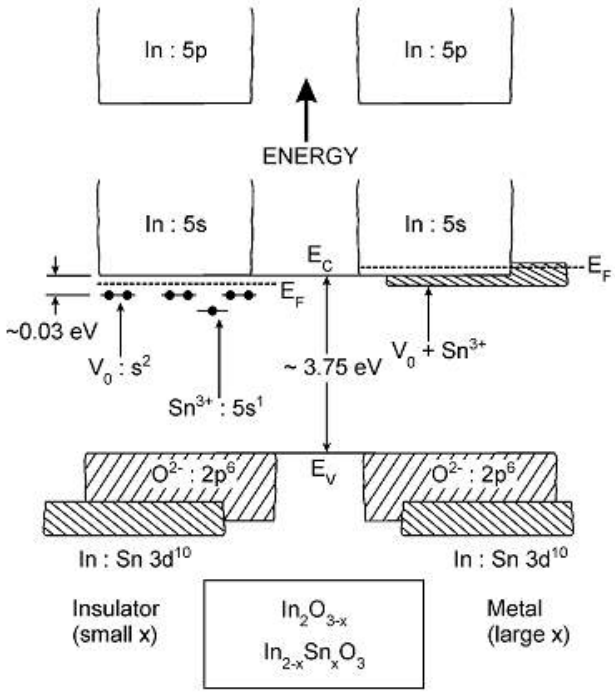

Figure 1.4: *Scheme of the energy bands of ITO as a function of doping level x. The left column represents low x values, the right column high x values. The impurity band appearing at large x is formed by contributions of O vacancies and substitutional Sn. (Taken from ref. [45])*

x as a doping level, adopted by Porch *et al.*, is quite convenient for explaining the electrical behavior of ITO, in that it considers the joint contribution of intrinsic (O vacancies) and extrinsic (Sn^{4+} ions) dopants rather than attempting to separate them, which is an extremely complex task as indicated above. The left part of the figure shows the full valence band, constituted by O $2p^6$ and In:Sn $3d^{10}$ orbitals, and the empty conduction band (In 5s and 5p), in low doping conditions. Available shallow states due to substitutional tin (occupying In^{3+} sites) and

oxygen vacancies are also reported, with an energy separation from the conduction band of around 30 meV (taken from earlier photoemission measurements by Fan *et al.* [7]). As the doping level x increases, these levels evolve into an impurity band which overlaps the conduction band, filling it with a degenerate Drude-like electron gas. An analogous process takes place in doped tin, zinc and titanium oxides [8, 46, 47].

This phenomenon, corresponding to an insulator-metal transition, is known as a Mott transition [48]. This transition occurs when the electron concentration exceeds a critical value n_c, identified by the following equation:

$$a_H n_c^{\frac{1}{3}} = 0.26 \pm 0.05 \tag{1.4}$$

where a_H is the (calculated) ground state Bohr radius associated to the donors. Theoretical results allowed to estimate that n_c for the most common TCOs is of the order of $10^{18} - 10^{19}$ cm^{-3} [45, 49].

Above this critical density, the conduction electrons in a TCO are therefore well modeled by a Drude-like gas of free electrons [4, 50]. In this picture, the electrical conductivity of the material is defined by the relation

$$\sigma = ne\mu \tag{1.5}$$

where e is the electron charge and μ is the carrier mobility, which in turn is defined as

$$\mu = \frac{e\tau}{m_c^*} \tag{1.6}$$

where τ is the mean time between two electron-lattice ion collisions, and m_c^* the electron conduction band effective mass.

Examining equation 1.5 shows that electrical conductivity can be increased either by increasing carrier concentration or mobility. From what has been discussed in section 1.1.1, an arbitrary increase in n is not possible without compromising optical transparency, therefore it is very important to understand how electron mobility can be controlled. Several phenomena can limit electron mobility by decreasing the τ parameter of eq. 1.6, i.e. by making scattering events more frequent. If the mean time between scattering events of one type is denoted by τ_i, the overall lattice τ can be estimated with the so-called Mathiessen rule [50]:

$$\frac{1}{\tau} = \sum_i \frac{1}{\tau_i} \tag{1.7}$$

Interestingly, each of the τ_i is strongly dependent on carrier concentration, i.e. different scattering mechanisms are dominant at different carrier concentration.

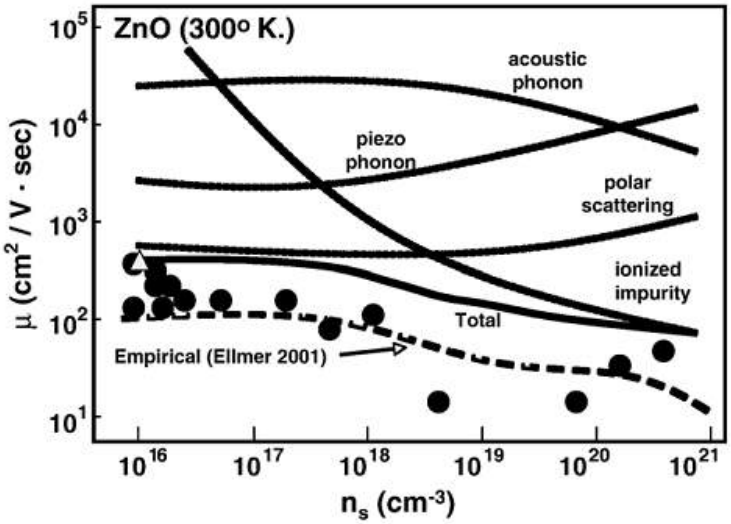

Figure 1.5: *Scattering mechanisms in ZnO as a function of carrier concentration. Continuous lines show calculated mobility limitations due to the individual scattering phenomena, and their sum is also shown as a continuous line. The dashed curve shows a fit of empirical data from literature. (Taken from ref. [15])*

An overview of the dominant scattering mechanisms at different n values can be seen in figure 1.5, which shows the calculated mobility as a function of carrier concentration for different scattering phenomena in ZnO, and the corresponding curve calculated from Mathiessen's rule(continuous lines), along with a comparison taken from a fit of empirical data [15,50]. The dominant mechanism (lower curve) is polar optical phonon scattering at low carrier concentrations (less than 10^{18} cm^{-3}), whereas for higher carrier concentrations mobility is limited by ionized-impurity scattering. A few things should be pointed out about this analysis: first of all, the theoretical calculations leading to the curves shown in figure 1.5 are performed according to a model [51] which does not explictly consider grain boundary scattering, which is extremely important (sometimes dominant) in the case of polycrystalline films [14,52,53]. Second, the fact that at the n values typical of TCOs the dominant mechanism is constituted by ionized impurity scattering allowed theoreticians to consider this contribution in detail in order to calculate an upper limit to mobility in doped TCOs, which was found to be relatively independent of the type of material chosen, around 90 cm^2/Vs [54].

1.2 Transparent electrodes: state of the art

1.2.1 Conventional TCO films

Transparent electrodes in the form of compact thin TCO films are nowadays available commercially on an industrial scale for optoelectronic devices, energy-efficient windows, flat panel displays and various types of photovoltaic devices [9, 10,55,56]. In order to optimize the performance and the cost-effectiveness of TCO films, a great variety of synthesis techniques have been explored over the years. Physical Vapor Deposition (PVD) techniques, like Magnetron Sputtering (MS) or Pulsed Laser Deposition (PLD) allow to obtain extremely low resistivity and sheet resistance (i.e. specific resistivity per unit thickness) in the most common TCOs. In this section, the state of the art of main TCO materials will be reviewed focusing on electrical properties, since transmittances of the order of 80-90% are commonly available for all investigated TCOs [57]. The majority of PVD processes to obtain TCO materials are performed at high temperatures (around 200-300° C for MS and 200-400° for PLD).

In the case of ITO, the best available sputtered thin films commonly have resistivities slightly lower than $10^{-4}\ \Omega\,\mathrm{cm}$, with sheet resistances typically smaller than 10 $\Omega/\square$ [58]. With PLD (which will be described in detail in part II of this work) even lower resistivity values can be obtained (down to $7\ \cdot 10^{-5}\ \Omega\,\mathrm{cm}$ [59]) with the drawback of decreasing the deposited area. Also with doped ZnO (in particular Al-doped ZnO, AZO and Ga-doped ZnO, GZO) resistivities below $10^{-4}\ \Omega\,\mathrm{cm}$ have been obtained by PLD [60], slightly lower than those obtained by MS [61]. Room temperature MS has also been reported for the development of Ga-doped ZnO films with resistivity of the same order of magnitude [62]. For Fluorine-doped Tin Oxide (FTO), deposition by PVD is rarely performed [57] and can lead to resistivities of the order of few $10^{-3}\ \Omega\,\mathrm{cm}$ [63]. For this material, the most common deposition technique available also on an industrial scale, for large-area substrates, is Chemical Spray Pyrolysis, with which resistivities of the order of $10^{-4}\ \Omega\,\mathrm{cm}$ can be obtained [64]. This inexpensive technique has also been used to grow doped ZnO films [65, 66], obtaining resistivities of the order of the $\mathrm{m}\Omega\,\mathrm{cm}$, and ITO films with $10^{-4}\ \Omega\,\mathrm{cm}$ [67]. In the field of wet chemically based deposition processes, Metal Organic Chemical Vapor Deposition (MOCVD) and related techniques are also widely employed: for doped tin oxide (with fluorine or tantalum) it is possible to achieve resistivities of the order of $10^{-4}\ \Omega\,\mathrm{cm}$ even at moderate ($\approx$ 200°C) temperatures [64]. CVD-deposited TCO films based on

(Al, Ga or F) doped ZnO and ITO have also been synthesized with resistivity comparable to those obtained by PVD (higher by a factor 2-5) [57]. Other chemical-based processes such as sol-gel coating or Atomic Layer Deposition have also been used to develop ZnO, SnO_2 and In_2O_3 based TCOs: in this case the electrical conductivity is generally lower than the optimized materials of the same family by about one order of magnitude [57]. As a concluding remark, the majority of the results listed in this section involve some deposition steps performed at non-room temperature: in the following sections, the importance of room temperature deposition for some devices will be discussed.

1.2.2 Latest developments in Transparent Conductors

The goal of increasing carrier mobility in TCOs, as pointed out in section 1.1, is a key point to be addressed in order to improve electrical performance without compromising optical transparency. One possible means to obtain high mobility values has been discovered by Hosono *et al.* in 1996 [18] and is based on replacing conventional heavily doped metal oxides with amorphous ternary compounds. The idea behind this approach is to exploit the great overlap between the ns orbitals of heavy metals, which constitute the bottom of the conduction band in their oxide compounds, to obtain a greater electron mobility in that band, as opposed to amorphous covalent solids (e.g. a-Si:H) where the conduction band is made of p orbitals which have a small spatial overlap [17, 18, 68]. A scheme of the spatial distribution of electron orbitals in such materials is reported in figure 1.6. This structure of the conduction band allows a significant orbital overlap even if short range order is broken, as happens in amorphous systems: this can be seen in figure 1.6, and holds for materials based on metals with a $(n-1)d^{10}ns^0$ configuration, i.e. post transition metals. The most performing amorphous oxides in terms of mobility are based on In or Sn, and with room temperature sputtered Indium-Gallium-Zinc-Oxide mobilities greater than 50 cm^2/Vs are easily obtained [69], leading to a quick application in most flexible transparent touch-screen displays on an industrial scale since 2011 [70]. These kind of device require room temperature deposition to ensure compatibility with flexible substrates.

In the field of crystalline oxide-based materials, recently, other TCO materials have been increasingly explored, such as Nb- or Ta-doped TiO_2 [71, 72] and many ternary compounds [14, 56, 73] obtaining resistivity values around one order of magnitude higher than the best binary TCO materials. Other peculiar TCO-

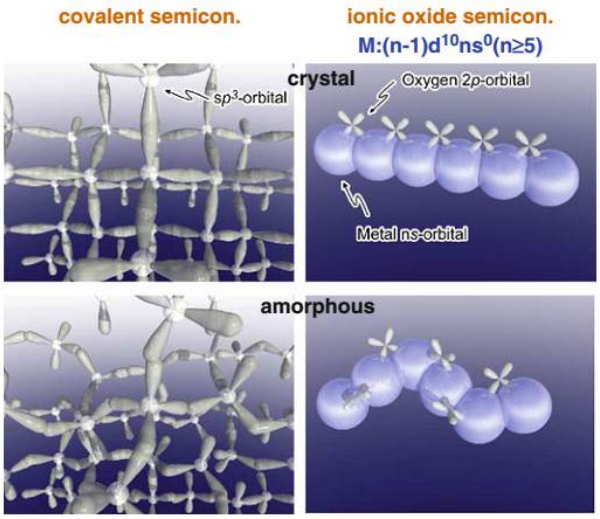

Figure 1.6: *Schematic orbital drawing of electron pathway (conduction band bottom) in conventional compound semiconductor and ionic oxide semiconductors. (Taken from ref. [69])*

based structures have also been investigated recently, mainly multi-layered stacks of TCOs and ultrathin metal layers [10] and electron-doped UV-transparent oxides. In these materials (the most notorious examples being $\beta-Ga_2O_3$ and $12CaO \cdot 7Al_2O_3$) the optical gap is wider than in conventional TCOs (5-7 eV) and electrical conductivity is obtained by forming a very narrow mid-gap band of available electronic states which does not compromise optical transparency [74].

Another important class of alternative transparent conductors has started to be investigated more recently, based on metal nanowire networks or grids as a replacement to oxide thin films [20]. Among the potential advantages of such approach, it may be worth to mention mechanical resistance, processing rapidity and low cost. Sheet resistances of the order of 10-50 $\Omega/\square$ and visible transparencies of the order of 70% - 90% have been obtained with metal nanowire and carbon nanotube grids [75]. At the present moment, the degree of optimization and applicability of such structures is still low due to the early stage of research, but reports of PV devices working with Ag nanowire network-based transparent electrodes have recently appeared [19].

In the latest years, graphene-based transparent conducting layers have also been investigated, due to the potentially unbeatable electron mobility in graphene layers (≈ 10000 cm^2/Vs), which could in principle compensate its low dopability [56]. Sheet resistances of the order of 30 $\Omega/\square$ have been reported for transparent graphene layers [76].

Finally, much effort has been put over the last decades in the development

of p-type TCO materials. The possibility to create transparent $p-n$ junctions would be of paramount importance for fully transparent electronics, but a number of physical and technical issues have limited the progress in this direction [77]. This is due to several reasons, the most important being the low hole mobility in the valence band (large effective mass and complex band structure), and the low dopability due to the ease of formation of oxygen vacancies which act as *hole killing defects* [15, 16]. P-type conductivity was succesfully obtained on TCOs based on Cu_xO, NiO, Sn_xO and ternary compounds including the same metals with Sr or Y [12, 17, 77–79]. All the investigated compounds suffered from either low bandgap (≈ 2 eV) or low obtainable carrier concentration ($p \approx 10^{18}\text{cm}^{-3}$). A promising candidate which has been recently indicated as a p-type TCO is B_6O, but its research is still at a very early stage [80, 81].

1.3 Requirements for transparent PV contacts

Among the various applications of transparent electrodes described in the previous sections, this work is going to focus on PV devices, in particular on their latest generations, namely thin-film solar cells and Hybrid-Organic PhotoVoltaics (HOPV). An overview of the main devices which currently employ one or more transparent conducting layers is presented in figure 1.7 [57]. Some important features and corresponding requirements can be pointed out considering these devices. In amorphous silicon-based devices, a primary feature which needs to

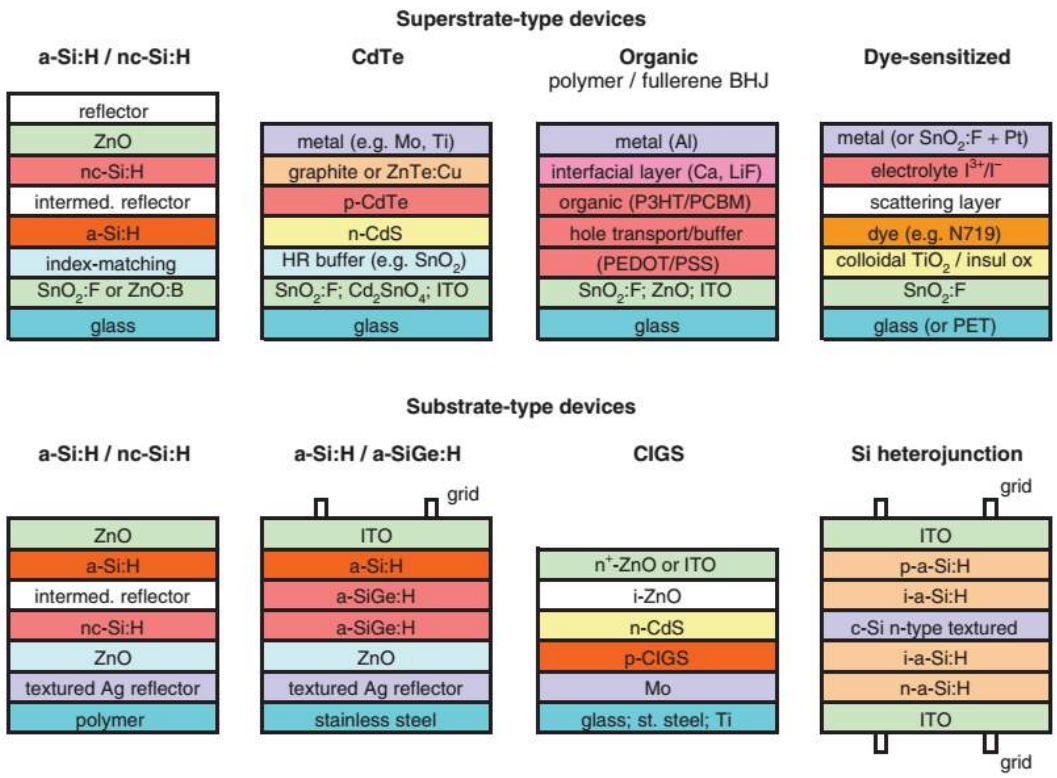

Figure 1.7: *Overview of photovoltaic devices which employ transparent conducting layers (green color). Taken from ref. [57]*

be provided by the transparent electrode is light trapping. In order to maximize light absorption by the active layer, whose thickness must be kept low to reduce costs and to control recombination effects, the path traveled by light inside it can be increased by trapping the photons inside the device. This can be achieved by textured coatings, plasmonic effects or controlled light scattering [82, 83].

For CdTe-based and Copper-Indium-Selenide cells, the absorption properties of the active layer need to be matched by the near-infrared transmittance of the TCO: as discussed previously, this can be achieved by developing high mobility,

low carrier density TCOs. Furthermore, the high deposition temperature required to obtain CdTe layers needs to be sustained by all the parts of the device, including the transparent electrode [57, 84].

In Dye-Sensitized Cells (DSCs), two main components are constituted by oxide-based layers: the transparent electrode and the electron transport layer/photoanode. The electrode, besides conventional high transparency and conductivity, needs to have a careful energy level matching to collect the dye photogenerated charges. The transport layer, which is conventionally constituted by a TiO_2 paste, needs the fundamental properties of large surface area and mesoscale porosity, in order to maximize dye infiltration. In the case of liquid electrolyte DSCs, chemical stability is also a key issue [85]. In the development of oxides for DSCs, compact TCOs and commercial pastes are being replaced by 3-dimensional architectures [86–88], which can also be used to perform the task of light scattering (figure 1.7 contains a scattering layer). Lately, new DSC-like devices employing perovskite-based materials as an active layers have been developed with promising efficiencies, but their optimization is still far from application [89].

If organic cells are considered, other critical properties emerge: since the typical thickness of the active layer (typically P3HT:PCBM blends or related materials) is of the order of few hundred nanometers, the transparent electrode needs to have low surface roughness to avoid the arisal of short circuits in the cell [86]. To minimize internal energy losses, control of band alignment (work function) becomes a matter of great importance in these devices as well [9]; furthermore, this type of devices have the peculiarity of being fabricated at room temperature to be compatible with flexible substrates. This is an extremely significant challenge: it may be worth to remark that nearly all of the conventional TCOs described in section 1.2 are synthesized or processed at high temperature.

2

Al-doped ZnO as a transparent conductor

This chapter is dedicated to reviewing the main properties and applications of Al-doped Zinc Oxide (AZO) as a transparent conductor. The main physical background of TCOs presented in section 1.1 and the main requirements for new PV devices discussed in section 1.3 will be used as a starting point to introduce the specific issues, results and challenges connected to the application of AZO as a transparent electrode in PV cells. Finally, section 2.3 presents the specific goals of this work in the introduced framework.

2.1 Physical properties of doped and undoped ZnO

Zinc oxide is an oxidic compound naturally available in the wurtzitic hexagonal crystal structure, with a direct bandgap of 3.3 - 3.4 eV [90,91]. Since its discovery in the form of the zincite mineral in 1810, ZnO has been widely studied and applied in several fields, e.g. photovoltaic devices, thin film transistors, light emitting diodes, gas sensors, nanogenerators [90–93]. An overview of some important physical properties of ZnO, adapted from ref [90], is presented in Table 2.1. Some important features can be pointed out: the abundance of ZnO in the earth's crust is higher by a factor 400 with respect to In_2O_3, which makes doped ZnO a promising candidate for a low cost replacement of ITO, also considering the similar bandgap which is optimal for a TCO. The dielectric permittivity is higher in ZnO, which is in principle beneficial for the width of the transparency window (see eq. 1.3 for the relation between permittivity and plasma energy). Finally, piezoelectricity in ZnO is a peculiarity which led to its application in many kind of devices, and has lately been exploited to increase the efficiency of PV devices [94].

A picture of the calculated band structure of ZnO is reported in figure 2.1. On the left, the calculated bands of a single crystal ZnO are presented. The valence band is constituted by O 2p states close to the Fermi level, and the Zn 3d states form the flatter band at lower energies, whereas the bottom of the conduction band is constituted by Zn 4s states [43]. It should be pointed out that Density Functional Theory (DFT) calculations for ZnO always require the introduction of self-interaction corrections due to the strong localization of O 2p orbitals, which constitute the top of the valence band [38, 95] and lead to an unphysical shrinkage of the band gap if not taken into account [96]. The right part of figure 2.1 shows the modifications of the band structures due to

Parameter	ZnO	In_2O_3
Earth crust abundance	40 ppm	0.1 ppm
Eg	3.4 eV (direct)	3.6 (direct)
Lattice structure	Hexagonal wurtzite	Cubic Bixbyite
Lattice parameters	$a = 3.25$ Å, $c = 5.21$ Å	$a = 10.12$ Å
Mass density	5.67 g/cm^3	7.12 g/cm^3
High frequency dielectric permittivity	$\varepsilon_{\infty,\|\|} = 3.75$, $\varepsilon_{\infty,\perp} = 3.70$	4.6
Melting temperature	1975 °C	1910 °C
Piezoelectric coupling factor	0.47	-

Table 2.1: *General properties of zinc oxide, compared to indium oxide (adapted from ref. [90])*

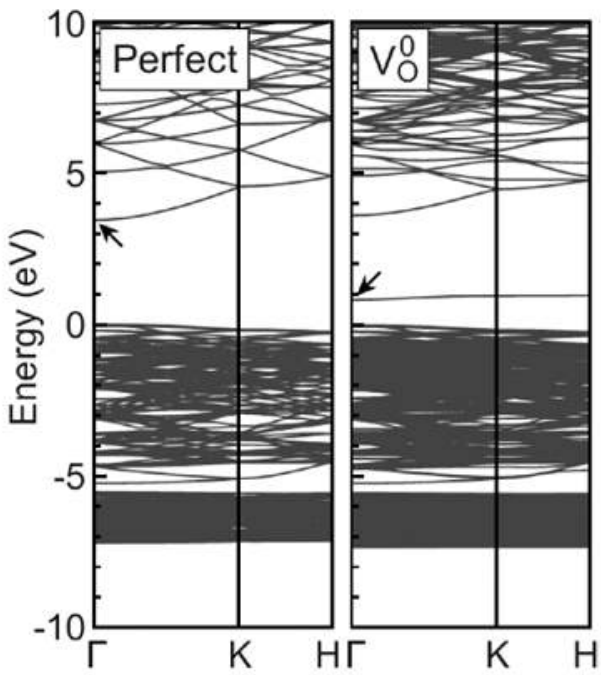

Figure 2.1: *Calculated band structure of ZnO in perfect crystal conditions (left) and with a neutral oxygen vacancy state (right). The zero of energy corresponds to the valence band maximum. Taken from ref. [43]*

the formation of oxygen vacancies. The role played by oxygen vacancies in ZnO has been (and still is) a debated subject [35, 36, 97, 98]: the intrinsic n-type conductivity of undoped ZnO has been historically attributed to electrons deriving from ionized O vacancies, supposedly acting as doubly charged electron donors [99, 100]. However, theoretical calculations have repeatedly questioned this explanation, asserting that oxygen vacancies cannot act as shallow donors and generate room temperature conductivity due to the distance between the level (see fig. 2.1 and the conduction band). There is now sufficient agreement among theoreticians in identifying hydrogen as an unintentional donor providing n-type conductivity in undoped ZnO [37,101]. The calculated ionization energy of intersitial H atoms in the ZnO lattice is of approximately 40 meV, as opposed to the 300 meV for the ionization of oxygen vacancies, and the energy level associated with neutral H impurities falls within the conduction band [101]. From the experimental point of view, however, accurate determination of H incorporation in a crystal is extremely difficult, due to the difficulty of controlling H content both during preparation and measurement [102]: for this reason, and due to a widely accepted empirical correlation between oxygen content and electrical conductivity

in ZnO-based materials, caution is still required when discussing this matter. To account for this correlation, theoreticians have demonstrated that substitutional H_O (hydrogen atoms occupying O lattice sites) can also play an important role and have a similar ionization energy to H interstitials [43]: this would explain why it is experimentally easier to obtain high carrier density values in oxygen-deficient ZnO, where H could occupy the empty O sites and act as donors. If polycrystalline materials or thin films are considered, other important effects due to surfaces and grain boundaries come into play [12]: the Density of States (DoS, see fig. 2.2.(a)) is modified by the introduction of deep levels above the valence band maximum, due to O 2p dangling bonds [38]. These states are occupied at room temperature, leading to a decrease in optical transmittance at energies slightly lower than the bandgap. It is interesting to note how grain boundaries

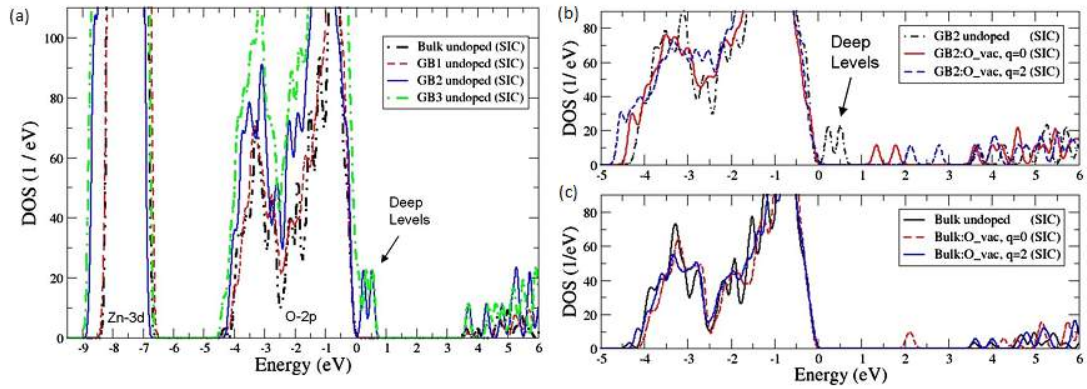

Figure 2.2: *(a) Calculated DoS for bulk ZnO and for ZnO supercells with different types of grain boundaries. (b) Calculated DoS for ZnO supercells without defects (black), with neutral oxygen vacancy (red) and with ionized oxygen vacancy (blue). (c) Calculated DoS for bulk ZnO without defects (black), with neutral oxygen vacancy (red) and with ionized oxygen vacancy (blue). The acronym SIC stands for Self-Interaction-Corrections (DFT method introduced above). Taken from ref. [38].*

and oxygen vacancies can exhibit a significant interplay in ZnO: if the DoS curves shown in fig. 2.2.b are considered, the deep levels originating from O dangling bonds at grain boundaries are canceled by the introduction of O vacancies, which decrease the possibility of having O atoms at grain boundaries. New available states are formed, which in the case of ionized oxygen vacancies (blue curve in fig 2.2.b) are closer to the conduction band and may indeed contribute to charge carrier density. Conversely, the presence of grain boundaries can compensate the defect states arising from oxygen vacancies: an example is presented in figure 2.2.c, where the mid-gap defect state associated to the oxygen vacancy in bulk

ZnO (red) is visible. Such state is not present in the polycrystalline DoS shown in figure 2.2.b, due to competing effects of grain boundaries and oxygen vacancies. Another intrinsic defect indicated as a possible source of conduction electrons is the Zn interstitial. Although the defect state associated with Zn_i is close to the conduction band ($\approx$ 46 meV [103]), its high formation energy makes it a less plausible candidate for the source of n-type conductivity.

Finally, the introduction of available states and the corresponding filling of the conduction band can be achieved by intentional extrinsic doping. As in the majority of TCOs, ZnO has been successfully n-doped with different elements (mainly trivalent metals substituting Zn), but p-type doping has been reported with less significant results to date, in spite of several attempts with monovalent metals or with group-V elements in the place of O [56, 103]. Focusing on n-type donors, the most widely used dopants for ZnO are Al, Ga and In, although available reports of B, Cr, F and also Si-doped ZnO are present in literature [43, 103, 104]. A summary of intrinsic and extrinsic donors for ZnO, for which the calculated energy position is available, is reported in Table 2.2.

Element	Structure	Energy ($E_{CB} - E$)
Al	Al_{Zn}	60 meV
Ga	Ga_{Zn}	54.5 meV
H	H_i	40 meV
In	In_{Zn}	63 meV
O	V_O	300 meV
Zn	Zn_i	46 meV

Table 2.2: *Intrinsic and extrinsic donors in zinc oxide and energy position with respect to the conduction band minimum. Adapted from ref. [103]*

After discussing the possible means of filling of the conduction band, it is possible to consider carrier mobility. As discussed in section 1.1, electron mobility in transparent conductors is influenced by different scattering phenomena. In the case of bulk ZnO, the most important scattering mechanisms are determined by piezo and polar phonons, neutral and ionized impurities [50, 51, 56]. If polycrystalline ZnO is considered, dislocations and (especially) grain boundaries become another major scattering source [53, 103]. While phonon and dislocation-driven scattering processes are extremely complex to model [50, 103], scattering at grain boundaries is relatively simple to describe in terms of a potential barrier

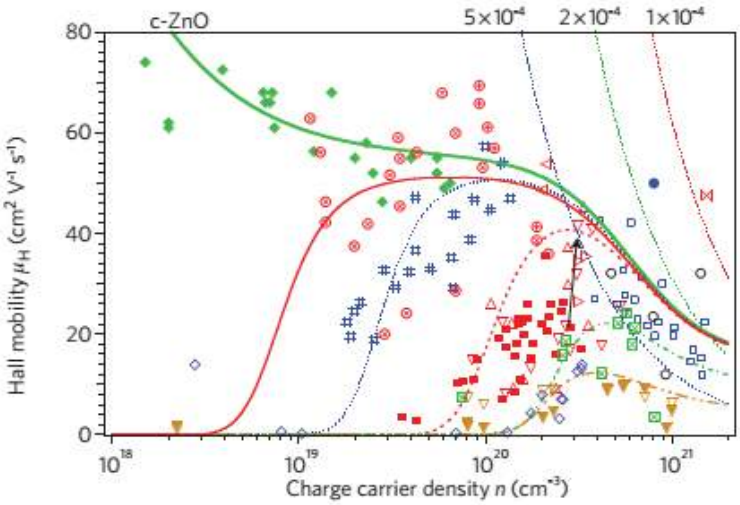

Figure 2.3: *Carrier mobility as a function of carrier concentration in polycrystalline ZnO: all the isolated points are experimental data, bell-shaped curves are their fits combining the effects of grain boundary and ionized impurity scattering, dashed lines show constant resistivity curves. The green line corresponds to single-crystal ZnO (as in figure 1.5.) Taken from ref. [56].*

of height Φ_B, leading to a mobility of the form

$$\mu_{EFF} = \mu_0 \exp\left(-\frac{\Phi_B}{kT}\right) \tag{2.1}$$

where μ_0 is the intragrain mobility and depends on the grain size, and Φ_B depends on charge carrier trap density at the boundary. Interestingly, several authors have demonstrated that Φ_B is increased in the case of O-rich ZnO polycrystals, where excess O atoms accumulate at grain boundaries constituting trap states for electrons [53, 105, 106]. In the case of heavily doped ZnO, the extrinsic dopant cations can also segregate at grain boundaries and decrease the mobility [41, 107]. A comprehensive analysis of carrier mobility in ZnO as a function of carrier concentration, combining theoretical calculations and fits from experimental data, is reported in figure 2.3 [103]. This graphs shows a collection of experimental (n, μ) values for ZnO obtained by various deposition techniques, identified by isolated points with different shapes. The data have been fitted with bell-shaped curves which consider both ionized impurity and grain boundary scattering as mobility-limiting mechanisms. The green line on the top represents the fit curve for single crystal ZnO (as in figure 1.5). It is interesting to notice how, for high carrier density values ($n > 5 - 6 \cdot 10^{20}\text{cm}^{-3}$) the fitted data for doped and undoped polycrystals approach the monocrystal trend: this is an indicator of the fact that ionized impurity scattering, which is the dominant mechanisms

for bulk ZnO as discussed in section 1.1, dominates carrier transport also in polycrystals. The steep decrease of mobility and greater separation from single crystal ZnO at lower concentrations indicate that grain boundary scattering is the dominant mechanisms for lower carrier concentration values. The dashed curves representing constant resistivity values are also shown as a reference: noticeably, the experimental points in the top-right corner (lowest resistivities), correspond to doped ZnO films grown by PLD on heated ($\approx 300°C$) substrates (refs. [108,109]).

2.2 AZO as a transparent electrode: requirements and state of the art

This section is focused on Al-doped Zinc Oxide (AZO) as a transparent electrode for PV devices, which will be the main subject of the experimental research described in parts II and III of this work. The first reports of extrinsic n-doping of ZnO by aluminum date back to the 1950s [103], and the application of AZO to PV technology is nowadays mainly found in chalcopyrite-based (Copper-Indium-Gallium-Selenide, CIGS) and amorphous silicon solar cells [57]. As anticipated in section 1.3, Hybrid and Organic PhotoVoltaic (HOPV) devices are now being intensively investigated as a low cost flexible alternative to thin-film based solar cells: AZO can find application in Bulk HeteroJunction (BHJ) devices as a replacement to ITO [110], and in Dye-Sensitized Cells (DSCs) as a higher-mobility substitute of TiO_2 in the photoanode or as a transparent contact instead of FTO [87,111].

For the devices mentioned above, the properties of electrical conductivity and optical transparency of AZO are not sufficient: first, in order to decrease the thickness of active layers, effective light trapping and management is required [57]. Second, the possibility to obtain structures with large surface area is important (especially for DSCs, where AZO can be used also as a mesoporous photoanode) when interfaces need to be maximized [85]. Third, HOPV cells (and flexible devices in general) require room temperature deposition to ensure compatibility with polymer substrates: as discussed in section 1.2 the majority of PVD and CVD processes involve steps performed at high temperature [57]. Furthermore, the most common ways to achieve light trapping involve the texturing of AZO layers by chemical processes [112], which create further obstacles in the quest for compatibility with polymer substrates. One possible solution to meet all the requirements without introducing high temperature or chemically

aggressive processes is developing nanostructured AZO layers, exploiting the unique properties which emerge in nanostructured materials. ZnO is known to be extremely versatile in terms of nanostructurability, with a variety of different morphologies obtainable by several techniques [91, 113–115]. Although reports of these structures are more frequent for undoped ZnO, large surface area AZO layers have been synthesized in the form of ordered quasi 1-d structure arrays [116, 117], nano-combs [118] and nano-cones [119]. The development of ordered, hierarchical structures can also improve electrical transport along a preferential direction: especially in the case of high temperature synthesis, high carrier mobilities are easily achieved for metal oxide hierarchical structures [114, 120, 121].

In general, AZO layers in the form of conventional compact films can be optimized to have an electrical resistivity of the order of $10^{-4}\Omega\,\mathrm{cm}$ or less, as introduced in the previous sections: the best results were obtained so far with PLD on heated substrates ($T \approx 300°$ C, $\rho \approx 8.5 \cdot 10^{-5}\Omega\,\mathrm{cm}$, $n \approx 10^{21}\mathrm{cm}^{-3}$, $\mu \approx 50$ $\mathrm{cm}^2/\mathrm{Vs}$ [108, 109]), but only few and recent reports of AZO synthesized at room temperature are available, either with PLD [122, 123] or MS [124, 125], with resistivities rarely lower than 10^{-3} $\Omega\,\mathrm{cm}$. However, the possibility to grow other metal oxide nanostructures by PLD at room temperature has been demonstrated [88, 126] and will be exploited in this work to obtain large surface area and light trapping in room temperature-grown transparent conducting layers.

Light trapping in AZO films, as pointed out above, is generally achieved by chemical texturing (i.e. etching) processes [112] which modify the top surface in order to trap the light inside the device by internal reflections. This is considered of primary importance not only for thin film devices, but also for HOPV cells [127], where decreasing the thickness of the active layer can improve device performance [128]. Other light trapping techniques have been studied recently, such as nanotexturing induced by crystal orientation [129], plasmonics [83], laser patterning [130], AZO nanosphere embedding [131]. An example of the effects of texturing in an AZO layer on the external quantum efficiency (EQE) of a thin film silicon solar cell is presented in figure 2.4 [132]. The light trapping effect is clearly visible by comparing the decrease in reflectance − i.e. the increase in (1-R_{TOT}) in figure 2.4.a − of a compact AZO film (dots) and a hydrogen-textured AZO (HAZO) layer (squares). This means that light is scattered and reflected inside the cell, allowing for an increase in absorption in the active layer, which increases the photon-to-electron conversion efficiency (i.e., the EQE). An example of the obtained texturing is reported in figure 2.4(b). The EQE curve shows

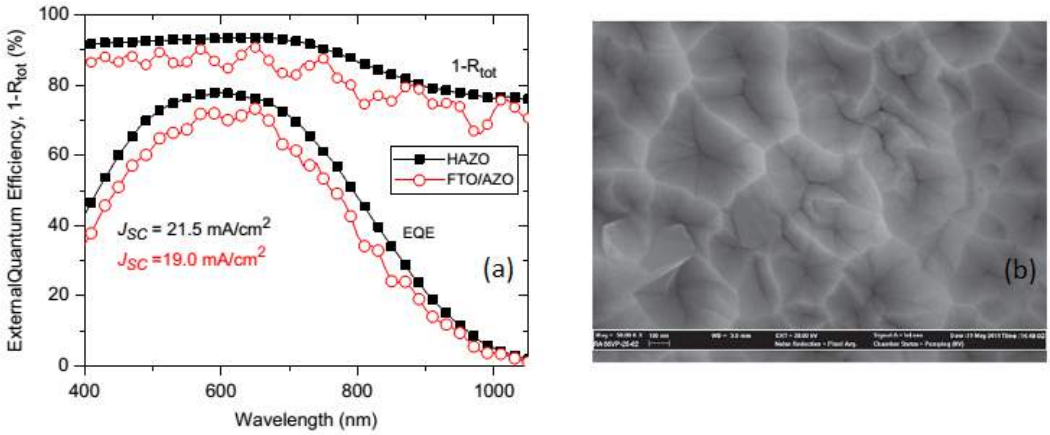

Figure 2.4: *(a) External Quantum Efficiency (EQE) and anti-reflection effect (1-R_{TOT}) of amorphous silicon solar cells with compact AZO on FTO substrate (dots) and with hydrogen-textured AZO (HAZO, squares). The increase in short circuit current density is also reported. (b) SEM micrograph of a textured AZO surface. Taken from ref. [132].*

an increase due to texturing, which causes a 13% gain in short current circuit density (in this example, the authors report a 20% increase in power conversion efficiency [132]). An indicator commonly used to characterize the light scattering ability of a TCO is the haze factor, defined as the ratio of diffuse transmittance to total transmittance: in order to achieve successful light trapping in the device, the haze factor must be of the order of 30-40% in the visible range (in this example the authors report $H \approx 45\%$). Other quantities can be used to characterize the light trapping capability of a TCO, such as Angular Resolved Scattering, which however is important for selected applications where particular light incidence directions are required [133].

2.3 Objectives of this work

The outlined framework of research on AZO as a transparent electrode with non-conventional properties can be used to define the main goals of this work as follows:

- The synthesis of transparent and conducting AZO layers with electrical and optical properties compatible with the state of the art, performed at room temperature to ensure compatibility with polymer substrates and flexible devices. As discussed above, the majority of AZO layers obtained at level of research or on an industrial scale require high temperature deposition:

the first goal of this work will be to investigate the possibility to achieve transparent and conducting AZO films at room temperature.

- The achievement of light scattering and trapping by controlling light-matter interaction at the nanoscale. Rather than proceeding with conventional techniques such as chemical texturing, this work aims at obtaining effective light management by engineering nano- and microscale structure and morphology during film synthesis, without making use of any post-treatments requiring chemical or thermal processing.

- A deep understanding of the modification of electronic and optical properties in nanostructured AZO is still required. Several open issues related to the role of defects and the electrical conduction mechanisms are present, and the relation between structure and properties needs further investigation. In this work, the investigation of structure/property relationship in nanostructured AZO will be exploited to obtain control of the functional properties which are required for application in new generation PV devices.

- The possibility to obtain state-of-the-art transparent conductors by PLD, along with the versatility of this technique in obtaining nanostructured materials, have already been demonstrated. In this work, room temperature PLD will be exploited to synthesize strongly diversified materials in order to deeply explore the structure/property relation of AZO layers. The possibility to obtain quasi-1d hierarchical structures, with expected preferential transport and light management, which has been demonstrated for other materials, will be investigated for AZO in order to meet the requirements described above.

Part II

Control of structure/property relation in Al:ZnO

3

Materials and methods

In this chapter the main experimental techniques employed during this work will be described. Only the main physical principles and concepts needed for the following discussion are reported here; for technical experimental details, the reader is referred to appendix A, where deposition and measurement equipments are described.

3.1 Pulsed Laser Deposition

Nanosecond Pulsed Laser Deposition (PLD) belongs to the class of Physical Vapour Deposition (PVD) techniques. Its working principle can be summarized as follows: first, a high energy pulsed laser spot is focused onto the surface of a solid target, whose surface is ablated. The vaporized species subsequently expand in the form of a supersonic plasma with a characteristic *plume* shape until they reach the deposition substrate placed in front of the target, where condensation and film growth take place. The physics of ablation and plume expansion is extremely complex and depends also on the timescale of the pulses (which in this case is of the order of ns, which is the most typical condition) [134–137]. A detailed description of laser ablation processes is beyond the scope of this work: in this section only the main aspects relevant to the following chapters will be considered. A scheme of the PLD system is presented in figure 3.1. The laser

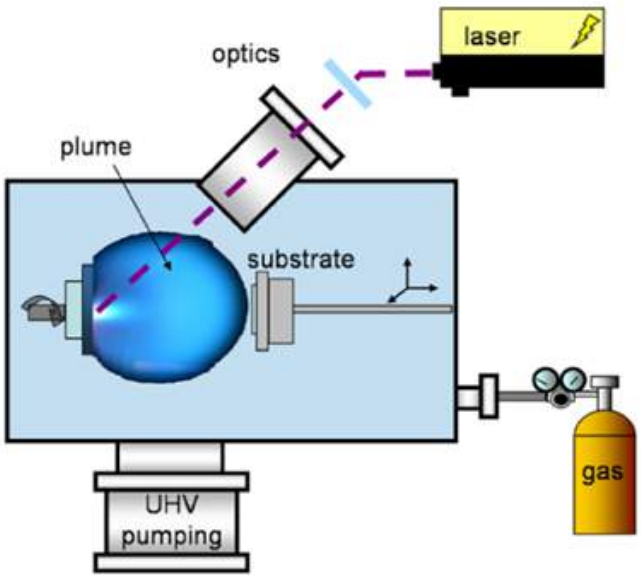

Figure 3.1: *Scheme of the PLD apparatus. The laser path is indicated by the purple dashed line.*

pulses are focused by an optical system onto the target surface (the laser path is marked by the purple dashed line in fig. 3.1). The size of the focused spot and the pulse energy determine the energy density on the target, which is one of the critical parameters of PLD. In fact, the ablation process originates from the interaction between the laser pulse and the target surface. In typical ablation conditions for ns PLD, the laser power on the target is of the order of 10-100 MW, corresponding

to energy density (fluence) values of several J/cm^2 and electric field intensities of the order of 10^5 V/cm [136]. The movement of the ablated species towards the substrate occurs in a plume-shaped partially ionized plasma of supersonic particles (blue plume in figure 3.1) whose properties are strongly dependent both on the laser fluence and on the atmosphere inside the deposition chamber. The chamber is evacuated to high vacuum conditions by a pumping system, and can then be filled with a background gas at a controlled pressure and in known flow conditions. The background atmosphere (gas type and pressure) can be modified to achieve control of the plume shape, length and degree of ionization, by affecting the plume expansion dynamics, allowing to move between different deposition regimes, which can be sketched as follows [138]:

- a low-pressure "vacuum-like" regime with a forward directed flow and a reduced scattering of the ablated species,
- a transition regime with strong momentum transfer to the background gas and formation of a shock wave, and
- a regime characterized by diffusion of the ablated particles at high pressure.

In low pressure conditions, the species ablated from the target proceed almost without collisions and reach the substrate with high kinetic energy, leading to atom-by-atom deposition of compact and bulk-like dense films. If pressure is increased, the background gas molecules and the ablated species undergo collisions which can lead to the spatial confinement of the ablation plume: the plume edge is better defined due to the presence of a travelling shock wave front which slows down until it reaches the so-called stopping distance. Upon collisions, clusters are formed in the gas phase and the kinetic energy with which the substrate is reached is lower. At higher pressures the diffusion of clusters in the gas is favored, and their kinetic energy is further decreased. A convenient way to identify these deposition conditions consists in introducing an adimensional parameter L, defined as the ratio of the target-to-substrate distance d_{TS} to the time-integrated visible plume length l_p at each laser pulse [136]. As depicted in figure 3.2, when $L < 1$ the substrate is placed "in plume" and collisions are not sufficient to induce significant clustering, resulting in a compact film. If $L > 1$, plume confinement induced by collisions favors cluster nucleation [139] and leads to the deposition of cluster-assembled nanostructured materials. Control of morphology can be achieved by variations on the properties of the ablation plume, which depend both on laser

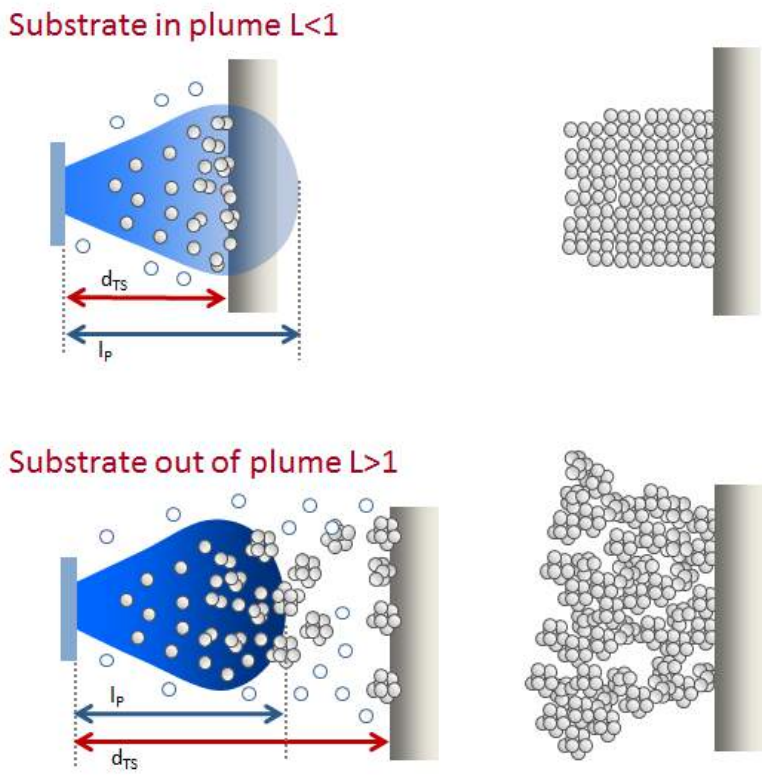

Figure 3.2: *Schematic picture of PLD conditions for different L values. Adapted from ref. [136].*

fluence and deposition pressure, or by varying d_{TS}. Finally, in the case of PLD of oxide materials, the effects of a reactive (oxygen-rich) deposition atmosphere must be taken into account. In fact, when a solid oxide target is ablated, oxygen from the background atmosphere can interact with the "building blocks" which assemble into the film in order to obtain different stoichiometry in the film, which is of primary importance for functional properties as discussed in the previous chapters.

A few drawbacks of PLD as a deposition technique should also be mentioned: first, the deposited films have uniform thickness only over a small area (of the order of 1 cm^2). Thickness uniformity can be increased by performing off-axis depositions and rotating the substrates, in order to obtain a circular corona of several cm^2 with uniform thickness, at the expense of decreasing the total deposition rate. Second, during the ablation phase molten particles are ejected in the form of *droplets*, which appear in the film as spherical protrusions which are detrimental in case low surface roughness is required.

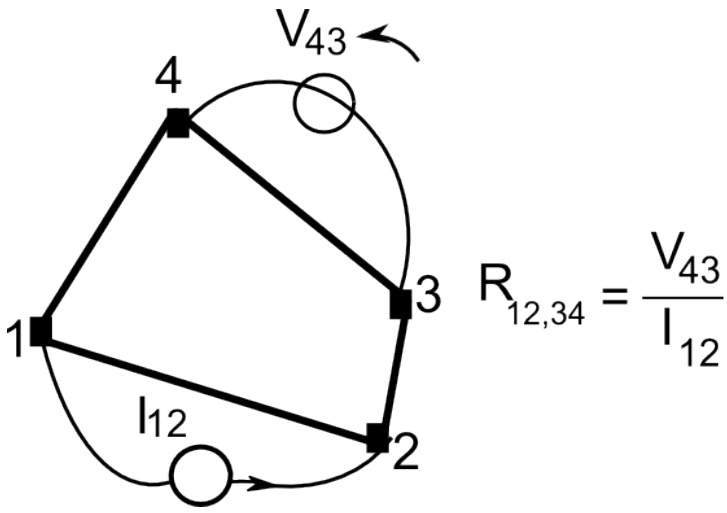

Figure 3.3: *Scheme of the 4-point probe Van der Pauw measurements*

3.2 Electrical measurements

The characterization of electrical properties of thin films is almost universally performed following the 4-point probe approach introduced by Van der Pauw in 1958 [140]. According to this approach, in a connected film (i.e. without holes) of uniform thickness, if 4 electrical contacts with negligible dimensions with respect to their distance are placed on the corners of the sample, then it is possible to extract the electrical resistance of the material regardless of its geometry. In particular, two electrodes are used to inject a known current, and the corresponding voltage drop is measured across the opposite electrodes (see figure 3.3) to determine the resistance on one sample side. Then the measurement is repeated by reversing the current flow, and by exchanging the current carrying electrodes with the voltage readers. The same approach is repeated on the 4 sides of the sample in order to average over the 8 possible combinations. The 8 measured resistance values must satisfy the following reciprocity and symmetry conditions:

$$
\begin{aligned}
R_{21,34} &= R_{12,43} \\
R_{32,41} &= R_{23,14} \\
R_{43,12} &= R_{34,21} \\
R_{14,23} &= R_{41,32} \\
R_{21,34} + R_{12,43} &= R_{43,12} + R_{34,21} \\
R_{32,41} + R_{23,14} &= R_{14,23} + R_{41,32}
\end{aligned} \tag{3.1}
$$

If these relations hold, the Van der Pauw hypotheses are valid, and it is possible to extract the resistivity of the material if its thickness is known: if we call R_A and R_B the average resistance values on the two sides of the samples, then the sheet resistance (i.e. resistivity per unit thickness) R_S is the solution of the following equation

$$e^{-\pi \frac{R_A}{R_S}} + e^{-\pi \frac{R_B}{R_S}} = 1 \tag{3.2}$$

from which the resistivity ρ can be calculated as the product between R_S and film thickness d:

$$\rho = R_S d \tag{3.3}$$

In the case of a square sample, with R_A=$R_B = R$, equation 3.2 reduces to

$$R_S = \frac{\pi}{\ln 2} R \tag{3.4}$$

and can be solved analytically, otherwise a numerical solution is necessary.

Using a 4-point probe configuration, it is also possible to separate the contribution of carrier concentration and mobility by performing Hall effect measurements. If current flows in a metal-like material in the presence of a magnetic field orthogonal to the current density vector, the Lorentz force acting on charge carriers induces a transverse potential difference known as the Hall voltage V_H, which depends on the density of charge carriers n according to the relation [4]

$$n = \frac{IB}{qdV_H} \tag{3.5}$$

where I is the injected current, B the intensity of the applied magnetic field and q the charge of each carrier (in this case equal to the electron charge). In a measurement scheme like the one depicted in figure 3.4, the Hall voltage drop can be extracted by injecting the current along one diagonal of the sample and measuring the potential difference along the other diagonal. This measurement must also be repeated and averaged over the possible configurations of voltage and current, and it is usually also performed with a reversed magnetic field in order to compensate for possible offsets. It is important to notice that V_H values are generally orders of magnitude lower than the voltages measured for Van der Pauw resistivity measurements, and therefore need special care to compensate for measurement errors and noise. By recalling the definition of electrical resistivity (eq.1.5), carrier mobility can be calculated after the value extracted from eq. 3.5.

$$\mu = \frac{1}{qn\rho} \tag{3.6}$$

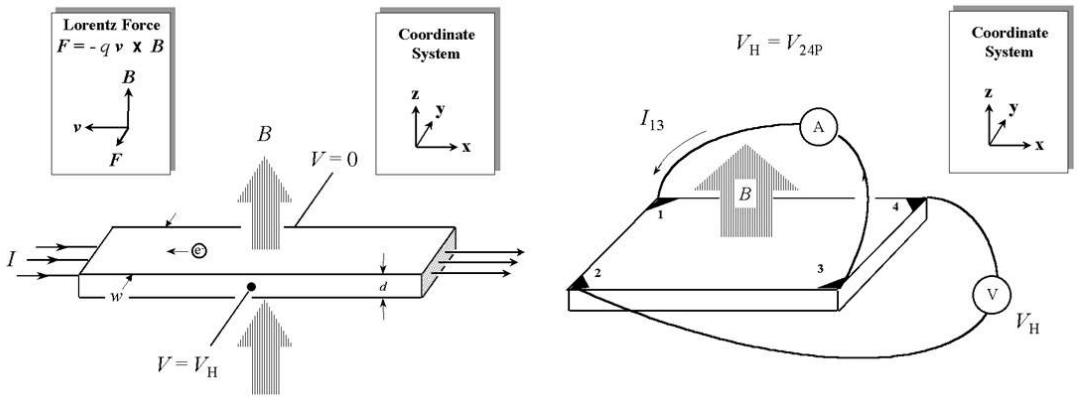

Figure 3.4: *Schematic of the Hall effect in a conductor (left) and relative 4-point measurement setup (right). The Hall voltage drop V_H is measured along the y axis.*

It is useful to remark that the description of the Hall effect through eqs. 3.5 - 3.6 was derived within the framework of the Drude model for ideal metals [4]: in the case of nanostructured materials with nonuniform connectivity, such results must be handled with care, considering μ as an effective mobility value, rather than a Drude-like mobility.

3.3 Optical measurements

The optical characterization of new TCOs, as introduced in part I, requires to measure transparency and light scattering properties. Optical transmittance can be measured with a conventional spectrophotometer, by detecting the total transmitted light intensity T over the whole solid angle (making use of an integrating sphere) at each wavelength. In this case the substrate contribution must be corrected for: the transmittance spectrum is normalized by setting at 100% the intensity at the substrate/film interface. This is done by measuring the transmittance of the bare substrate and then using it as a reference when measuring T of the samples (in this case, proper normalization is ensured by mounting the sample with the substrate facing the light source).

Light scattering properties are measured by calculating the haze factor, i.e. the ratio of diffuse transmittance to total transmittance, according to the scheme depicted in figure 3.5. The fraction of scattered transmitted light S is measured by opening the integrating sphere in order to let the specular light out, undetected. S is then divided by the total transmittance T in order to obtain the haze factor H.

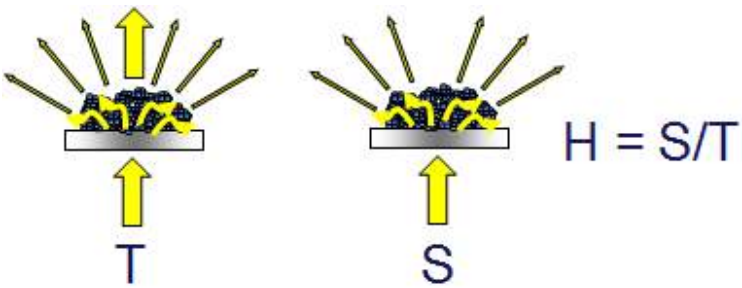

Figure 3.5: *Scheme of the haze factor measurements. S is the diffuse transmittance, T the total transmittance, H the haze.*

From transmittance measurements it is also possible to extract information about the optical gap with the Tauc method [141]. This method is widely used to investigate the optical absorption edge for interband transitions in doped semiconductors. The theoretical value of the absorption coefficient α for photon energies $h\nu$ just above the optical gap E_g is given by [21]

$$\alpha = C(h\nu - E_g)^{\frac{1}{r}} \tag{3.7}$$

where the constant C depends on the optical transition matrix element and the parameter r indicates the type of transition ($r = 2$ for direct bandgap transitions, which is the case of ZnO). Inspection of eq. 3.7 shows that the function α^r must

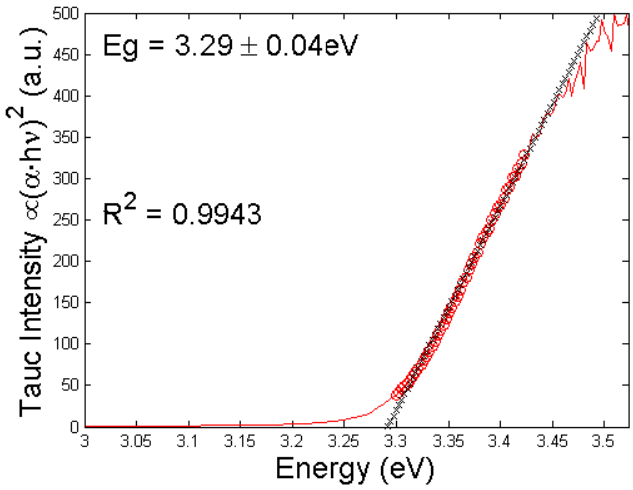

Figure 3.6: *Tauc plot of an AZO sample. Red dots are the experimental points in the linear fit range, black crosses constitute the linear fit.*

have a linear behaviour as a function of $h\nu$, and the intercept with the $\alpha = 0$ axis is found for $h\nu = E_g$, i.e. in correspondence of the optical gap. This is the basic

principle of Tauc plots, where α^r is plotted as a function of $h\nu$, and a linear fit close to the absorption edge is used to determine E_g. In some cases, $(\alpha h\nu)^r$ is plotted rather than α^r: this is due to the properties of the constant prefactor C in eq. 3.7 which in the case of a heavily filled and energy dispersed conduction band needs to be multiplied by $h\nu$ for a more accurate realization of the Tauc plot [142]. In the hypothesis (experimentally verified) that reflectance is negligible near the optical gap, α is experimentally determined from transmittance spectra making use of Lambert-Beer's law:

$$\alpha = -\frac{1}{d} \ln \frac{T}{1-R} \approx -\frac{\ln T}{d} \tag{3.8}$$

An example of Tauc plot realized in MATLAB is reported in figure 3.6. The figure shows the experimental $(\alpha h\nu)^2$ vs. $h\nu$ curve in red, with red dots in correspondence of the linear region. The linear fit is depicted as a line made by black crosses, and the intercept value is reported as Eg, with uncertainty estimated from the fit's residual sum of squares.

4

Control of structure and properties by Pulsed Laser Deposition

In this chapter the main results concerning room temperature synthesis of AZO layers by PLD are presented. Exploiting the properties of PLD introduced in section 3.1, the relation between structure and properties is investigated by synthesizing AZO layers with different morphology via variations of the background (O_2) gas pressure during deposition. Section 4.1 describes the effects of deposition pressure and gas flow rate on the properties of AZO layers, section 4.2 analyzes the structure/property relation by studying the effects of thermal treatments, then in section 4.2.3 a comparison with undoped ZnO is presented in order to investigate the role of extrinsic doping.

4.1 Structure-dependent electrical and optical properties

4.1.1 Morphology and structural properties

AZO thin films were synthesized by room temperature PLD performed in the presence of O_2 as a background gas. A solid syntered target containing Al_2O_3 and ZnO was ablated by a UV laser at different O_2 pressures. The main deposition parameters which were explored in the synthesis phase are listed in Table 4.1.

As introduced in section 3.1, the gas pressure in the deposition chamber is a fundamental PLD parameter which determines the properties of the ablation plume and, therefore, of film growth. In particular, higher deposition pressures induce collisions between the background gas and the ablated species, causing cluster nucleation and spatial confinement of the plume. Examples of ablation plumes of the Al_2O_3:ZnO target in different oxygen deposition pressures are shown in figure 4.1. On the left, the O_2 pressure in the chamber is low (10^{-2} Pa) and the

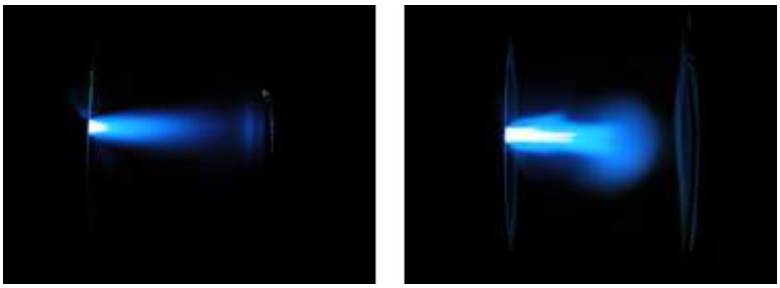

Figure 4.1: *Photographs of ablation plumes of the Al_2O_3:ZnO target with deposition pressures of 10^{-2} Pa O_2 (left) and 200 Pa O_2 (right) [143]*

plume is constituted by high energy species which experience few collisions with the background gas: the plume is highly directional and unquenched, the substrate is *in plume* ($L < 1$). On the right, with an oxygen pressure of 200 Pa, the plume is confined due to collisions, a shock wave front is visible and turbulence effects

Parameter	
Deposition pressure (O_2)	0.01 Pa - 200 Pa
Deposition time	7 min - 72 min
d_{TS}	40 mm 70 mm
O_2 flow rate	0 - 450 sccm
Al_2O_3 in deposition target	0 - 2% wt.

Table 4.1: *Overview of the main deposition parameters whose effects were investigated. One parameter was varied at a time.*

(plume bifurcations) appear. The substrate-to-target distance is the same in the two pictures (5 cm), and the visible plume length is sensibly shorter at higher pressure ($L > 1$). Collisions between oxygen molecules from the background gas and species ablated from the target favor cluster nucleation: this has extremely strong effects on film morphology. To understand these effects it is possible to look at the variety of morphologies which were obtained by varying the O_2 pressure while leaving all other deposition parameters (laser fluence, d_{TS}, deposition time) unchanged. The laser fluence was fixed at 1 J cm^{-2}, chosen as a compromise value to avoid an excess of droplets and delamination-inducing stress present at higher fluences, without excessively decreasing the deposition rate. An overview of AZO layers grown at pressures between 0.01 Pa O_2 and 200 Pa O_2 can be seen in figure 4.2, where examples of cross-sectional Scanning Electron Microscope (SEM) images of AZO films are reported. At low deposition pressures (0.01 Pa -

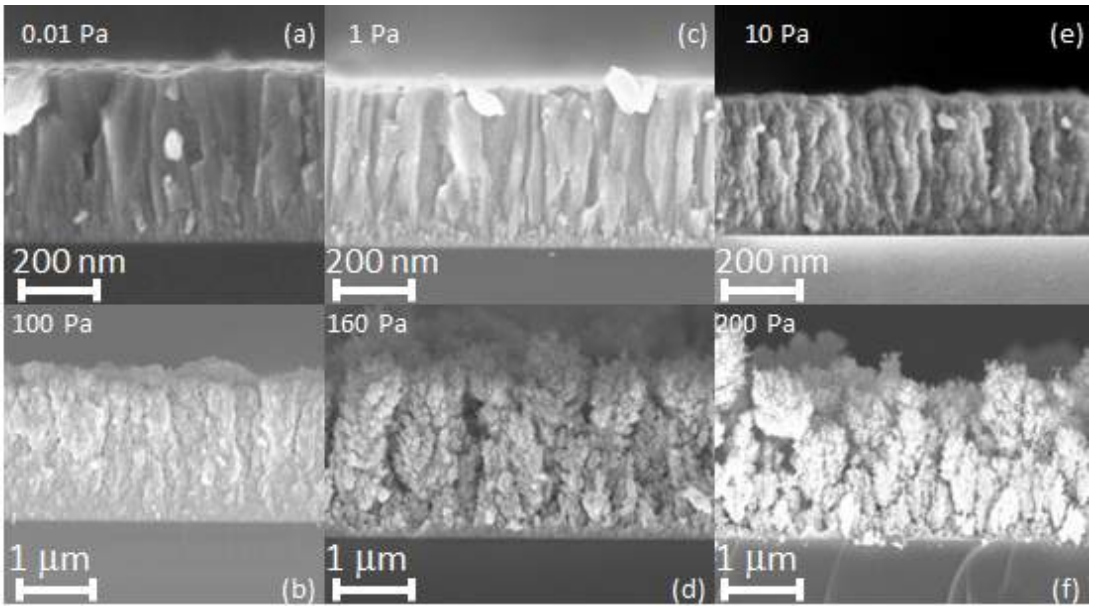

Figure 4.2: *Cross-sectional SEM images of AZO layers grown with different O_2 pressures [144].*

10 Pa), films are characterized by oriented columnar domains of variable size, with a compact structure. As the pressure is increased (10 Pa - 100 Pa) the morphology becomes granular, and hints of a nanoscale porosity are present: the films become rougher and the columns featured at low pressures start to become less connected, evolving into partially separated oriented nanostructures. At higher pressures (100 Pa - 200 Pa), AZO layers exhibit a significant fraction of voids, with mesoscale porosity and a morphology featuring hierarchically assembled forest-like structures. To clarify the concept of hierarchically assembled structures, a

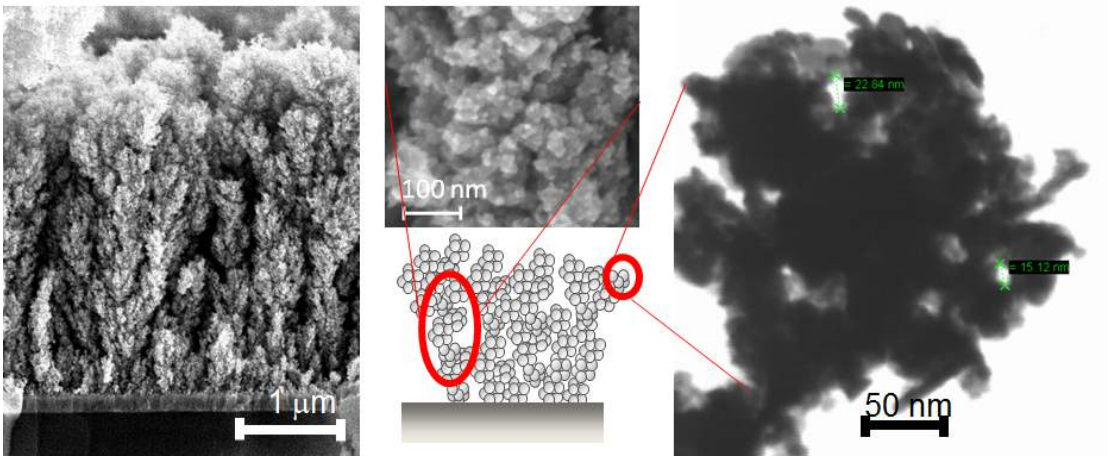

Figure 4.3: *Characteristic length scales of a hierarchical AZO nano-forest grown at 160 Pa O_2: microscale for the forest, mesoscale for the trees, nanoscale for the leaves (image obtained in transmission mode).*

multi-scale image of a film grown at 160 Pa is reported in figure 4.3. As shown in the figure, hierarchical AZO nano-forests are constituted by features which can be engineered at different length scales: the whole forest, corresponding to the whole film, has a height (film thickness) in the µm range, the individual trees have diameters of hundreds of nanometers (mesoscale), and the size of each leaf, i.e. the cluster building block whose nucleation is controlled by PLD properties, is in the nm range. Figure 4.2 also shows that porous films (bottom row) are significantly thicker than compact films (top row) even though the deposition times were the same (and therefore the deposited mass is comparable): this indicates a decrease in mass density due to the greater fraction of voids resulting from cluster assembly in porous films. Quantitative estimates of mass density were acquired by measuring the deposition rate with a quartz microbalance: the density of compact films is comparable to bulk ZnO (4-5.5 g/cm^3), whereas porous films have densities of 1-2 g/cm^3 or lower. The average estimated deposition rate of compact films was about 14 nm/min, the one of porous films was of the order of 80 nm/min.

A finer control over morphology and density of porous films was achieved by investigating the role of gas flow rate and d_{TS} at a fixed pressure of 100 Pa. An overview of the results of these variations can be seen in figure 4.4. Figures 4.4.a-c show that if the gas flow rate is increased from zero to high values (up to 450 standard cubic centimeters per minute, sccm) the assembly of hierarchical structures becomes more significant. Scarce thickness uniformity and lack of a preferential growth direction are visible in low or zero flow (and accordingly low

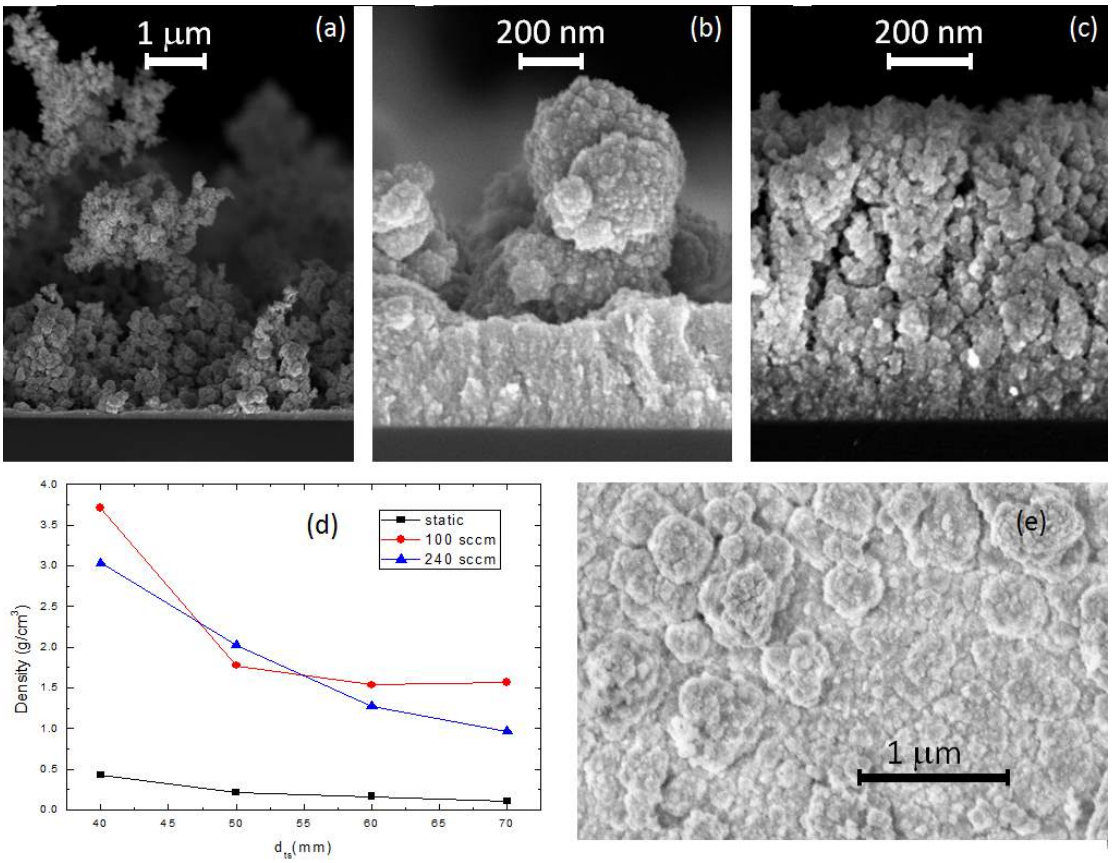

Figure 4.4: *Cross-sectional SEM images of AZO layers grown at 100 Pa O_2 in static conditions (a), with a 100 sccm flow (b) and with a 450 sccm flow (c). Mass density values as a function of target-to-substrate distance and gas flow rate (d). Top view SEM image of an AZO layer grown on ETFE polymer [145].*

or zero pumping speed, since the pressure is held constant at 100 Pa) conditions. In these conditions, the aggregates formed in the plume can reach the substrate even if their kinetic energy is extremely low (larger cauliflower-like aggregates) because the absence or reduced speed of the pumping system is not able to filter the clusters according to their energy. At high gas flow rates, anisotropic growth is enhanced, and hierarchical structures emerge. Fig. 4.4.b reports the trends in mass density of AZO grown at 100 Pa O_2 in different flow conditions and with different d_{TS} values. Significant variations can be obtained by varying the gas flow rate (the density of films grown in static atmosphere is smaller than 0.5 g/cm^3) or by varying d_{TS}, which is another way to vary the L parameter previously introduced. The higher density values obtained at lower d_{TS} are caused by the shorter distance traveled by the ablated species, which leads to a smaller number of collisions, which means that the substrate is reached with higher kinetic energy

and less disordered, porous aggregates are present. The compatibility of all AZO layers with polymer substrates was tested by performing the depositions also on Ethylene-TetraFluoroEthylene (ETFE) flexible substrates: an example of a porous film grown at 100 Pa O_2 on ETFE is presented in figure 4.4.e. Adhesion on ETFE was easily achieved for all porous films, whereas it required particular care and the development of a different procedure in the case of compact films, which was employed also on glass substrates. This is due to the higher energy with which the ablated species reach the substrates at low pressure, which results in the build-up of an internal stress which leads to film buckling and delamination. A solution to this problem was found in cleaning and sputtering the substrate surface with a beam of accelerated Ar^+ ions, causing an increase in roughness which allowed to accommodate residual strains in the first growth stages, allowing for successful deposition of AZO on flexible substrates.

Local structure of AZO films was characterized by means of X-Ray Diffraction (XRD) in $\theta - 2\theta$ configuration and Raman spectroscopy. The most important results of XRD characterization can be summarized as follows: first, all AZO films have a polycrystalline ZnO wurtzitic structure, despite room temperature growth. The XRD patterns of compact films are dominated by the (002) reflection (examples of peaks are presented in figure 4.5.a), indicating a preferential growth direction along the c axis. Such preferential orientation is partially lost at 10 Pa, where randomly oriented domains begin to appear (see fig. 4.5.c). At deposition pressures of 100 Pa O_2 and higher, crystal domains are randomly oriented and all XRD reflections of ZnO powders are present in the diffractograms. In the 0.01 Pa - 1 Pa pressure range, significant local disorder is suggested by diffraction peak broadening and shift: it was possible to estimate the trend in mean domain size from peak broadening by using Scherrer's formula on the (002) peak and the trend in the c lattice parameter from peak position using Bragg's law. These trends are reported in figure 4.5.c. A significant shift in the c lattice parameter was found at low oxygen deposition pressure: this can indicate lattice deformations due to defects such as O vacancies and Al interstitials. The decrease of this shift with increasing O_2 pressure suggests that O vacancies may be the dominant defect at low pressures. Furthermore, a smaller c value may indicate the presence of Al^{3+} in the Zn^{2+} lattice sites (substitutional), as Al has a smaller atomic radius than Zn [146]. The trend in domain size presents a maximum of ≈30 nm at 2 Pa O_2. Defects present at lower pressures and the onset of nanoscale porosity at higher pressures are most probably the reasons behind this optimal value.

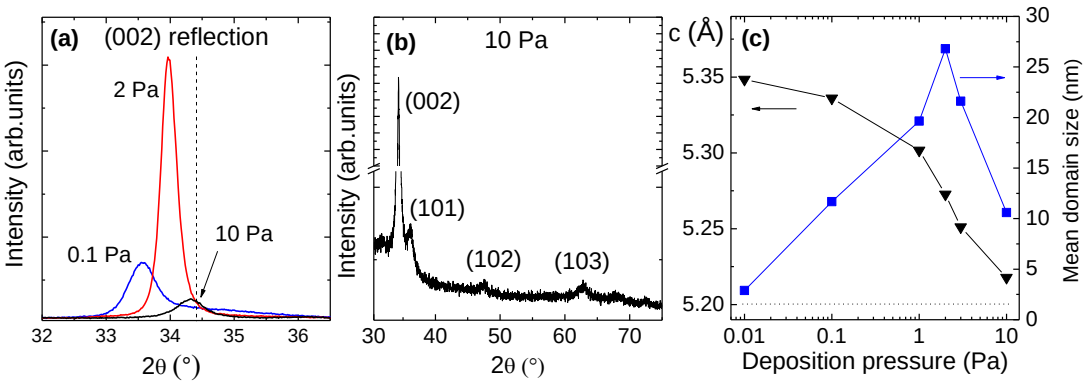

Figure 4.5: *(a) XRD patterns showing (002) reflection for films deposited at 0.1 Pa, 2 Pa and 10 Pa O_2; (b) XRD pattern of the film deposited at 10 Pa O_2; (c) mean domain size (blue squares) and c lattice parameter (black triangles) for as-deposited films as a function of deposition pressure. The dashed line shows the c reference value for unstrained ZnO.*

Results of Raman spectroscopy measurements also allowed to discuss structural order properties [147], even though their interpretation is by far less straightforward and requires a deep understanding of the phonon modes of ZnO which is beyond the scope of this work: for this reason only the main results will be listed here. Examples of Raman spectra for AZO layers grown with different O_2 pressures are presented in figure 4.6. The spectra are characterized by a low-frequency peak ($\approx$ 100 cm^{-1}) attributed to the Zn sub-lattice vibrations, and two peaks/bands at higher wavenumbers (visible in the figure at $\approx$ 400 and $\approx$ 600 cm^{-1}, respectively) associated with the O sub-lattice. The Zn sub-lattice peak emerges and becomes narrower with increasing deposition pressure as shown in figure 4.6, whereas the oxygen-related modes exhibit a change in relative intensity. The intensity ratio between these peaks/bands evolves from low deposition pressure (where the modes at $\approx$ 574-591 cm^{-1} are dominant) to high pressure (where the spectra are dominated by the feature at $\approx$ 409-438 cm^{-1}). Investigating the vibrational modes of the Zn and O sub-lattices by quantitative fits permitted to state that local order of the Zn sub-lattice is achieved almost regardless of the deposition pressure, whereas the O sub-lattice is characterized by strong local disorder especially at low deposition pressures. This fact can be used as a confirmation of the presence of O vacancies, whose presence is favored by a complex interplay with Al atoms (the effects of extrinsic doping on local structural order will be discussed in more detail in section 4.2.3 by taking advantage of comparisons with the Raman spectra of undoped ZnO films). An analysis of the

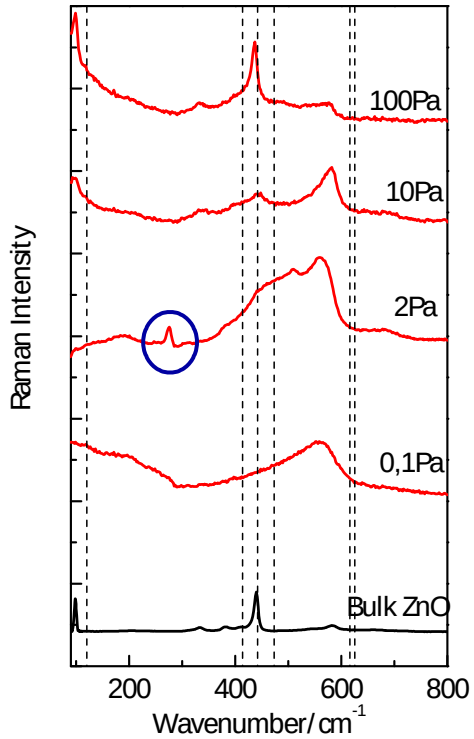

Figure 4.6: *Raman spectra of AZO layers grown at different O_2 pressures (red) and of the bulk ZnO target (black). The blue circle indicates an anomalous mode at 257 cm^{-1} empirically correlated with electrical conductivity [147].*

relative intensities of Raman peaks related to the Zn and O sub-lattices allowed to state that compact AZO films are heavily sub-stoichiometric in terms of oxygen content, moderately sub-stoichiometric at pressures of the order of 10 Pa and that stoichiometry is not fully reached until relatively high pressures ($\approx$ 80 Pa). Finally, an anomalous Raman peak of controversial interpretation was detected at 257 cm^{-1} with prominent intensity at 2 Pa. This peak, marked by a blue circle in figure 4.6, has been empirically correlated with electrical conductivity, which reaches its optimal value at 2 Pa O_2 as will be discussed in the upcoming section.

4.1.2 Electrical properties

Electrical measurements, performed in the Van der Pauw configuration (see section 3.2 for details) allowed to determine the electrical resistivity values of

compact AZO films (500 nm thickness), which were found to be in the $10^{-3} - 10^{-4}$ $\Omega\,\mathrm{cm}$ range for deposition pressures below 3 Pa O_2, increasing up to 0.1 $\Omega\,\mathrm{cm}$ at 10 Pa. The trend in electrical resistivity is reported in figure 4.7, where sheet resistance values can also be read on the right axis. The electrical properties of porous films were not measured in the conventional 4-point probe approach due to the difficulty of applying electrical contact on the top: depositions on evaporated metal contacts allowed to perform the measurement on the bottom part of the film. The measured resistivity of porous samples was extremely

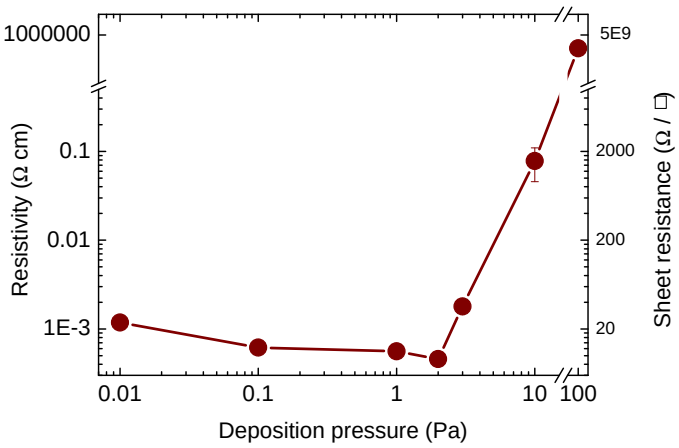

Figure 4.7: *Electrical resistivity and sheet resistance as a function of deposition pressure [144].*

high (of the order of the $\mathrm{M}\Omega\,\mathrm{cm}$) due to the open morphology which results in a distributed in-plane connectivity (lack of a continuous path for conduction electrons). The minimum resistivity value of compact AZO layers was obtained at 2 Pa O_2, where the measured resistivity was $4.5 \cdot 10^{-4}\ \Omega\,\mathrm{cm}$. This optimal value is the result of a compromise between defect concentration (oxygen vacancies and Al dopants can contribute significantly to conduction electrons concentration) and morphology effects limiting carrier mobility: it is useful to point out that this resistivity value is comparable to the state of the art of AZO layers grown at high temperature (see chapter 2). The separate contributions of carrier concentration and mobility, measured by Hall effect, allow to understand the physical meaning of this optimal value: figure 4.8 shows the results of Hall effect measurements. Carrier concentration values are extremely high ($10^{20} - 10^{21}\ \mathrm{cm}^{-3}$) at low deposition pressures, indicating that the filling of the conduction band is easier in oxygen-deficient films, which have a high concentration of defects as already suggested by XRD and Raman measurements. A brisk drop in carrier

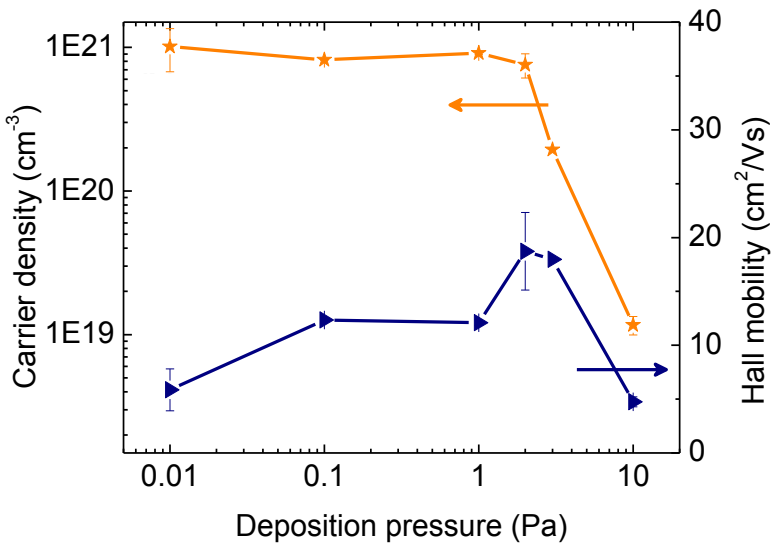

Figure 4.8: *Carrier concentration (orange stars) and mobility (blue triangles) as a function of deposition pressure for compact AZO layers [146].*

concentration (by 2 orders of magnitude) occurs in the pressure region from 3 to 10 Pa, pointing out an ineffective doping level possibly due to saturation of O vacancies. The trend in carrier mobility, with values ranging from about 5 to about 20 cm^2/Vs, noticeably recalls the one of mean domain size (see fig. 4.5) suggesting that grain boundary scattering is likely to be the dominant mobility-limiting mechanism. The maximum value is found at 2 Pa, where crystal domain size is also maximum, allowing to state that the large concentration of defects at lower pressures and trap states due to O segregation at grain boundaries at higher pressures give significant contributions, in agreement with theoretical and experimental considerations reported in section 2.1.

AZO layers of different thickness were grown at this optimal deposition pressure to investigate the influence of thickness on electrical properties: the results of resistivity measurements are shown in figure 4.9.a. Resistivity values are of the order of $10^{-4}\ \Omega\,cm$ for all thickness values (100 nm - 1 µm) and exhibit a decreasing trend with increasing thickness, the 1µm thick layers being twice as conductive than the 100 nm thick ones. The decreasing trend is maintained in sheet resistance (shown in the inset). The resistivity of a 1 µm thick film grown on ETFE substrate was about $3\ \cdot 10^{-3}\ \Omega\,cm$, i.e. compatible with state of the art values for flexible substrates [57]. A similar dependence of electrical resistivity on thickness can be justified by considering the beneficial effects on structural order resulting from

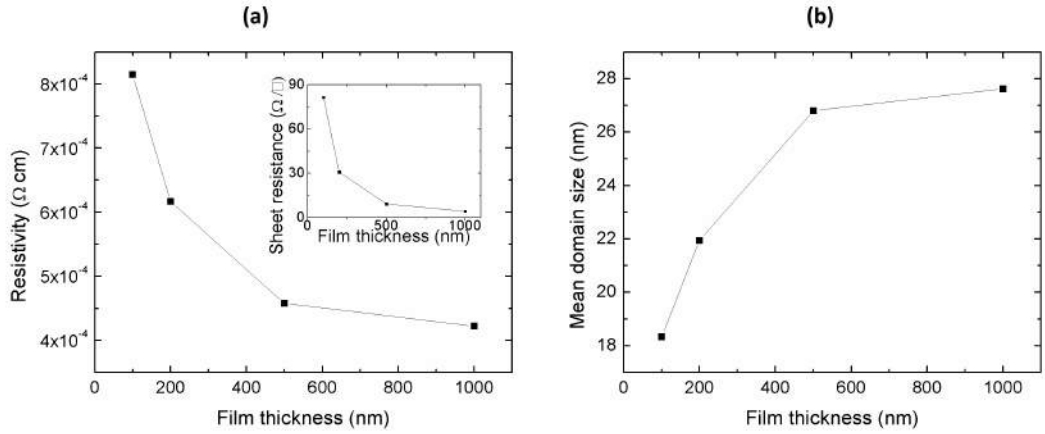

Figure 4.9: *(a) Electrical resistivity as a function of film thickness for films grown at a deposition pressure of 2 Pa. The inset shows the corresponding sheet resistance values. (b) Mean domain size, evaluated from Scherrer's formula on the (002) XRD peak. [148].*

a greater film thickness. In fact, results from XRD measurements performed on AZO layers grown at 2 Pa indicated that there is an increase in structural order with film thickness (fig. 4.9.b), as the mean domain size calculated from Scherrer's formula on the (002) XRD peak for layers of different thickness increased from 18 nm to 28 nm in the investigated thickness range.

4.1.3 Optical properties

Optical transmittance spectra and their average values (400 nm - 700 nm range) for AZO layers deposited with different O_2 pressure are presented in figure 4.10. The spectra have been acquired for films grown on glass substrates, and the substrate contribution has been corrected for by setting to 1 the intensity at the glass/film interface. The thickness of compact samples (up to 10 Pa) was 500 nm, whereas it was of 2 μm for porous samples (100-200 Pa). The spectra show an increase in transparency with increasing deposition pressure, as observed in figure 4.10.a. In the region below 300 nm, where photons excite interband electronic transitions, films grown at higher pressures exhibit a sharper onset of absorption (fig.4.10.b shows a close-up of the corresponding spectral region). The absorption due to interband transitions close to the optical gap is characterized by two different regimes: compact, oxygen-deficient films are more transparent in the higher-energy region (up to 380 nm) and porous, oxygen-rich samples are more transparent in the blue. This behaviour is in excellent agreement with results from *ab initio* calculations recalled in section 2.1 (and in particular fig.

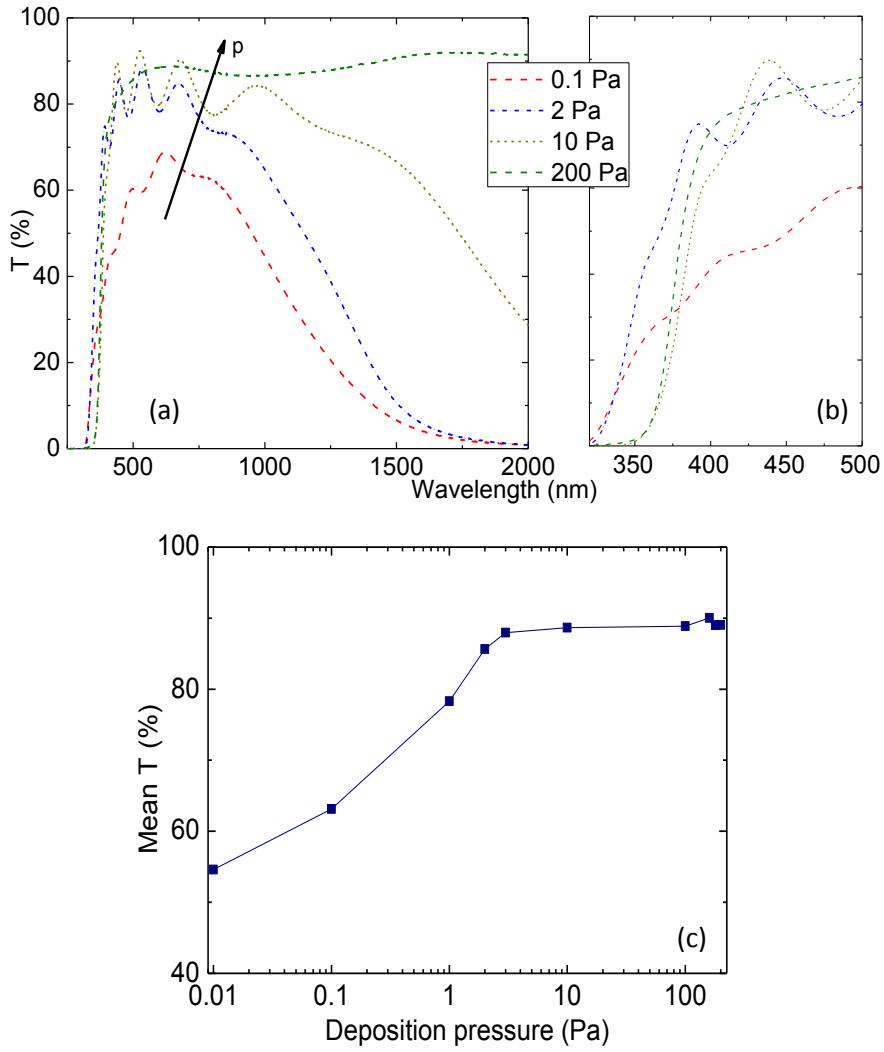

Figure 4.10: *(a) Total transmittance spectra of AZO films grown at different O_2 pressures. (b) A close-up of the onset of absorption in the near UV - visible range. (c) Mean transmittance values in the 400 nm - 700 nm range as a function of O_2 deposition pressure [144].*

2.2 [38]): grain boundaries create O 2*p* dangling bonds, i.e. available states above the valence band maximum which decrease the optical gap. O vacancies limit the presence of these dangling bonds, causing the optical gap to reopen and increasing UV transmittance of films grown at low O_2 pressures. In the visible, O vacancies increase light absorption through the introduction of intragap defect states, which add up to other Al- and Zn- related defects. In the IR region, absorption due to plasma oscillations of free electrons in the conduction band is extremely strong for samples grown at low pressure which have higher concentrations of electrons in the conduction band. The fringes in the visible range are due to interference phenomena, and their position depends on film thickness and on the refractive indices of both film and substrate. The spectra of porous samples do not present interference fringes, due to mesoscale disorder and increased surface roughness. The near-infrared region is characterized by a decrease in optical transmittance due to carrier absorption in the conduction band for samples grown at low O_2 pressures (up to 10 Pa) while porous films show high transmittance up to 2000 nm due to a less defective structure and a greater fraction of voids. A comparison of the mean values of optical transmittance in the visible range, taken between 400 nm and 700 nm, is reported in figure 4.10.c. The values increase monotonically with pressure, from 55% at 0.01 Pa up to nearly 90% for all pressures above 10 Pa. Porous films are characterized by an overall higher transparency, since their total transmittance is comparable but the thickness is 4 times as much.

Optical properties of films grown on ETFE polymer flexible substrates were characterized by comparable transmittance values: total transmittance spectra of 1 μm thick compact films grown at 2 Pa O_2 on glass and ETFE are reported in figure 4.11 as an example. The average transmittance values in the visible range were of 77% on ETFE and 80% on glass.

The light scattering capability of AZO layers was evaluated by measuring the haze factor. The measured haze values are presented in figure 4.12, which shows the average values in the 400-700 nm range as a function of O_2 pressure during deposition. The values are of the order of 10% for all compact films, indicating that their scattering ability is inefficient. At pressures of 100 Pa and higher, where morphology evolves from granular to mesoporous, the light scattering capability is enhanced, with a boost in haze from 30% to over 80%. This means that in AZO nano-forests, over 80% of the transmitted photons (which are over 85% of the incoming photons as seen from transmittance measurements) are scattered by the hierarchical structures. The reasons behind such high haze values are to be

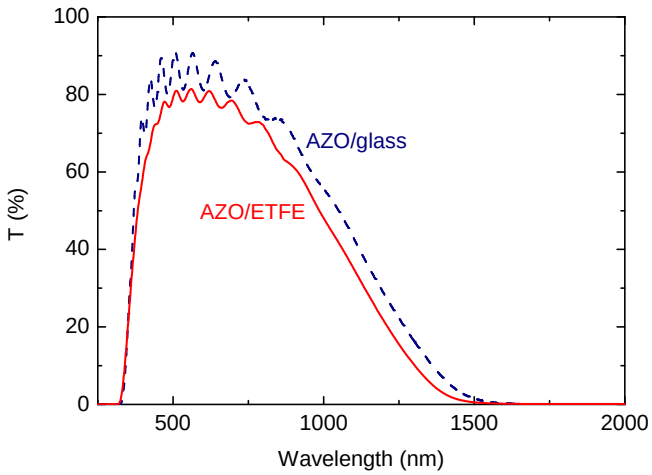

Figure 4.11: *Optical transmittance spectra of a 1 µm thick compact AZO layer grown at 2 Pa O_2 on glass and ETFE substrates [148].*

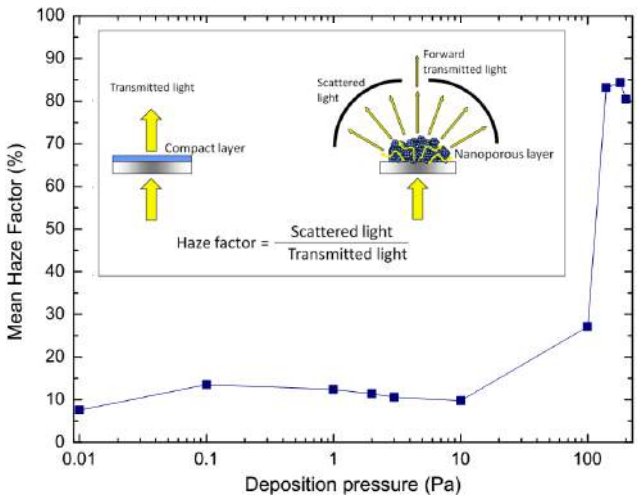

Figure 4.12: *Mean haze in the visible range as a function of deposition pressure. The inset shows a scheme of the scattering direction and of the measurement process [144].*

found in the characteristic size of the nanotrees (hundreds of nanometers) which is of the same order of magnitude as the visible light, thus maximizing scattering probability [149].

The method of envelope analysis [31, 150] was employed to estimate the refractive index of compact films by numerically solving the envelope equations for the position of the interference fringes in transmittance spectra, knowing film thickness from cross-sectional SEM measurements. Details on the envelope equations and on the iterative method employed for their solution can be found in Appendix B. Such analysis was not carried out on porous films due to the lack of interference fringes. The calculated trends of the real and imaginary part of the refractive index (n and k respectively) for a compact sample grown at 1 Pa are reported in figure 4.13, which also show the mean values in the visible range as a function of deposition pressure. The results of numerical calculations indicate

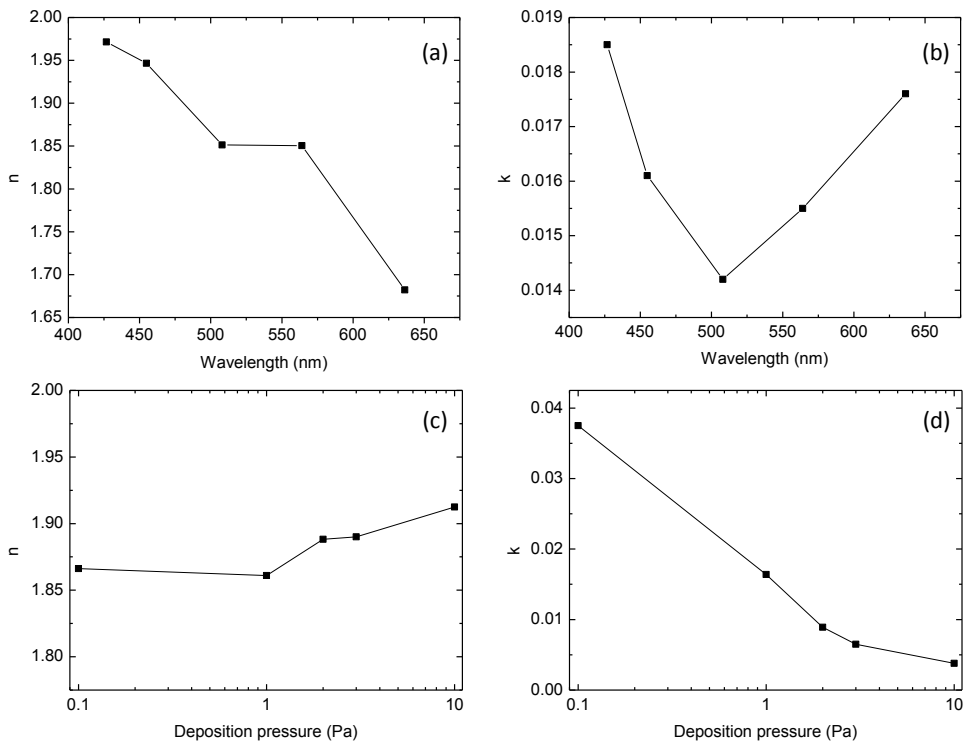

Figure 4.13: *(a-b) Calculated dispersion relations for the real and imaginary part of the refractive index of a compact AZO sample grown at 1 Pa O_2. (c-d) 400 nm - 700 nm Average values of the real and imaginary part of the refractive index as a function of deposition pressure [144].*

normal dispersion relations for n (i.e. monotonically decreasing with λ), and the mean values of the real part of the index in the visible range were found to be

about 1.90 for all compact films (pressures up to 10 Pa), which is in agreement with the typical values for ZnO (1.8-2.4) [91]. The variation of the extinction coefficient was also estimated over the visible spectrum with the same method. The calculated dispersion relations of the imaginary part k show a minimum in the visible (see fig. 4.13.b), and the average values are in agreement with the trends found in transmittance: films grown at higher oxygen pressures are characterized by a higher degree of structural order resulting in less significant light absorption. It is also worthwhile to notice that there is qualitative agreement between the estimated values of k and of the absorption coefficient α taken from Lambert-Beer's law, as the relation $\alpha = 4\pi k/\lambda$ holds (substituting the average values yields $\alpha \approx 10^4$ cm^{-1} for compact films and 10^3 cm^{-1} for porous films, for which only the Lambert-Beer estimate is available).

The infrared absorption profiles of compact AZO layers, as discussed in section 1.1, can be studied to obtain information on collective oscillations of free carriers in the conduction band. Absorptance spectra were calculated as $A = 1 - T - R$ from transmittance and reflectance measurements and are reported in figure 4.14. The

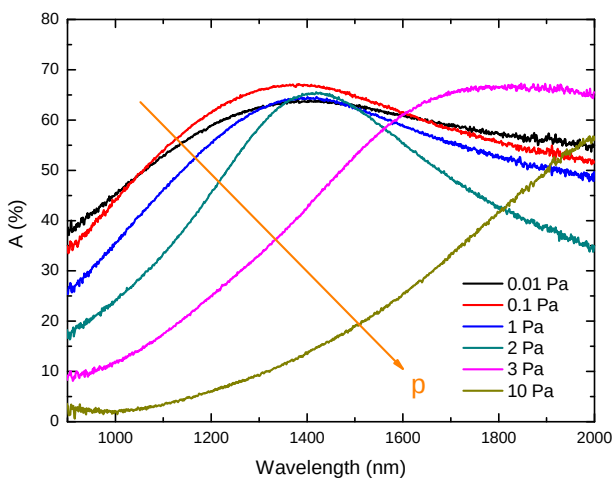

Figure 4.14: *Absorptance profiles in the near IR for compact AZO layers [144].*

absorptance peak is centered at the plasma wavelength, which (upon rearranging eq.1.3) can be written as follows:

$$\lambda_p = \frac{2\pi c}{q}\sqrt{\frac{m_c^* \varepsilon_0 \varepsilon_\infty}{n}} \tag{4.1}$$

The peaks reported in figure 4.14 shift towards higher wavelengths at higher deposition pressures: this is a consequence of the decrease in carrier concentration

(see section 4.1.2) in agreement with eq. 4.1. By evaluating carrier density n from Hall measurements and using the squared refractive index calculated above as ε_∞, it was possible to provide an estimate of the electrons conduction band effective mass which is the only unknown in equation 4.1. The obtained result was $m^* \approx 0.4m_0$, where m_0 is the electron rest mass. This value is in comparable with other estimates of other estimates of m^* in AZO calculated from plasma absorption [151, 152].

4.2 Effects of thermal treatments and Al doping

With the aim of a deeper understanding of the structure/property relation of AZO, thermal treatments in different atmospheres were performed on the materials described in the previous sections. Besides the general aim of improving the crystal structure of the layers, annealing treatments in an oxygen-rich environment (air) were devised to induce saturation of O vacancies, whereas vacuum or inert (Ar) atmospheres were employed to induce oxygen desorption.

4.2.1 Annealing in air

Annealing treatments in air (500°C, 3 h) were performed on samples to induce recovery of ZnO stoichiometry by saturation of oxygen vacancies. As a general remark, this kind of treatment is bound to have other effects besides O-related defect healing, e.g. humidity desorption: in the recently accepted picture which considers H atoms as unintentional electron donors in AZO (see section 2.1), many effects traditionally attributed to oxygen deficiency can be interpreted as hydrogen-induced. Recalling that a widely credited hypothesis concerning hydrogen as a donor states that H can occupy empty O lattice sites, many effects associated with oxygen can be also attributed to or correlated with hydrogen. For the sake of simplicity, in the following discussion annealing in air will be considered mainly as an oxygen vacancy healing treatment, but the results which will be presented are compatible with hydrogen doping, or even more probably with an interplay between H atoms and oxygen vacancies (especially in terms of electrical properties). Figure 4.15 shows the electrical resistivity of air-annealed compact AZO films as a function of deposition pressure. The two main effects of the thermal treatments are an increase in electrical resistivity (which reaches 0.1 $\Omega\,\mathrm{cm}$) and the flat behaviour of the trend vs. deposition pressure: the dependence on deposition conditions becomes almost negligible after annealing. The increase in resistivity is extremely significant (over two orders of magnitude) for films which showed better electrical properties prior to the treatment, and moderate for AZO grown at 10 Pa O_2, which was probably less influenced by the saturation of O vacancies due to a smaller initial concentration. These results allow to state that electrical conductivity in AZO is heavily influenced by defects formed during deposition, and their healing cancels its dependence on such defects.

Results of Hall effect measurements on annealed AZO are reported in figure 4.16. Carrier concentration values are characterized by a dramatic decrease upon

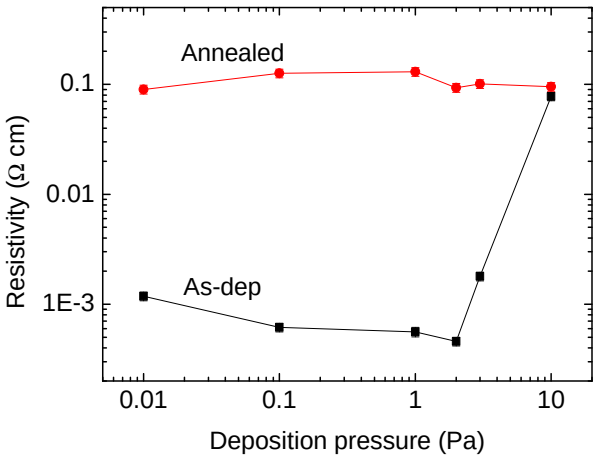

Figure 4.15: *Electrical resistivity as a function of deposition pressure, for as-deposited (black squares) and air-annealed (red dots) AZO layers [146].*

annealing, reaching values of the order of $10^{18} - 10^{19}\text{cm}^{-3}$ for all deposition pressures and becoming less dependent on deposition conditions. Carrier mobility is uniformly increased, probably due to an increase in structural order upon annealing which decreases electron scattering, reaching its highest values of 30-40 cm^2/Vs at 2-3 Pa. This increase in mobility is by far less significant than the drop in carrier concentration (over 2 orders of magnitude) indicating that the variations in electrical resistivity reported in figure 4.15 are mainly ascribable to a depletion of the conduction band.

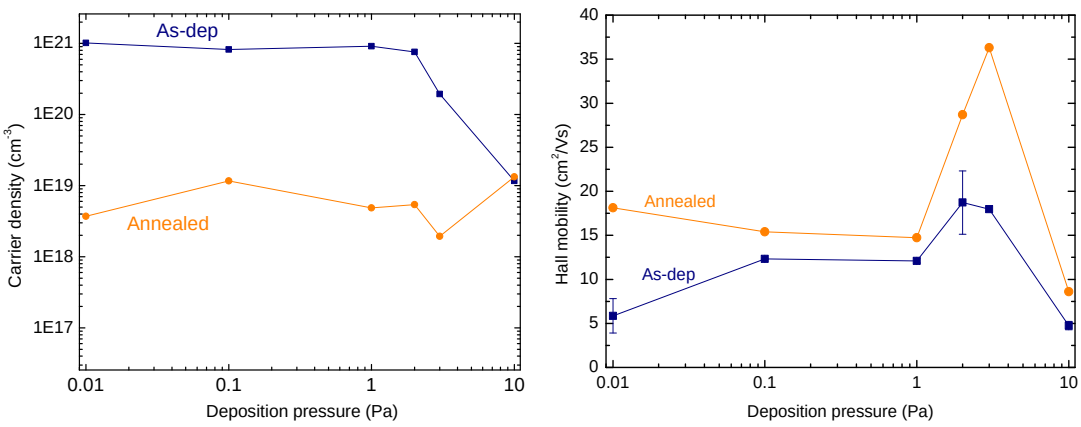

Figure 4.16: *Carrier concentration (left) and mobility (right) as a function of deposition pressure for as-deposited (blue squares) and air-annealed (orange dots) compact AZO layers [144].*

The influence of annealing in air on optical transmittance can be seen in figure 4.17. On the left, the spectrum of a compact highly oxygen deficient AZO

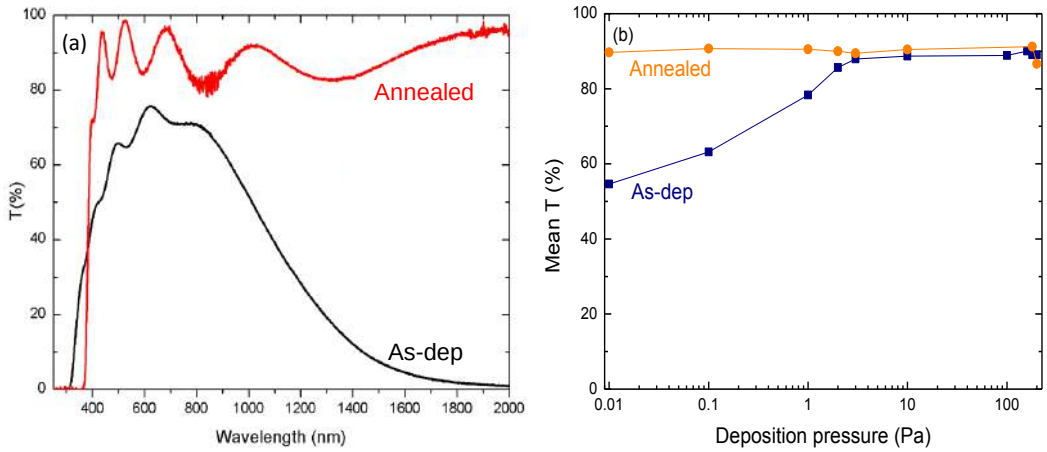

Figure 4.17: *(a) Example of a transmittance spectrum of an AZO compact layer grown at 0.1 Pa O_2 before (black) and after annealing (red) [146]. (b) Mean optical transmittance as a function of deposition pressure for as-deposited (blue squares) and air-annealed (orange dots) AZO layers. [144].*

layer (grown at 0.1 Pa O_2) is reported as an example to examine the effects of defect healing in different wavelength ranges: in proximity of the optical gap, the absorption edge becomes sharper after annealing, losing defect-induced absorption tails and re-establishing absorption by O dangling bonds at grain boundaries which was suppressed by oxygen vacancies. In the visible range, the mid-gap states associated to O vacancies disappear leading to an increase in transparency. In the IR, free carrier absorption is no longer present after annealing, due to the decrease in carrier concentration also noticed by Hall effect measurements. Figure 4.17.b shows the average transmittance values in the 400-700 nm range, highlighting the boost in transmittance of compact films (which reaches 85% regardless of the initial value, similarly to what emerged from electrical measurements) and showing how porous films, which already featured local structural order, are almost unaffected in terms of transparency. Haze values were not affected by the thermal treatment either (the data are not shown), since the characteristic size of the hierarchical structures, responsible for light scattering, does not vary upon annealing. The effects of annealing on the morphology of porous films, in fact, are limited to the nanoscale as shown in figure 4.18 (coalescence of

small hexagonal ZnO structures) and mesoscale morphology is not altered by the thermal treatment.

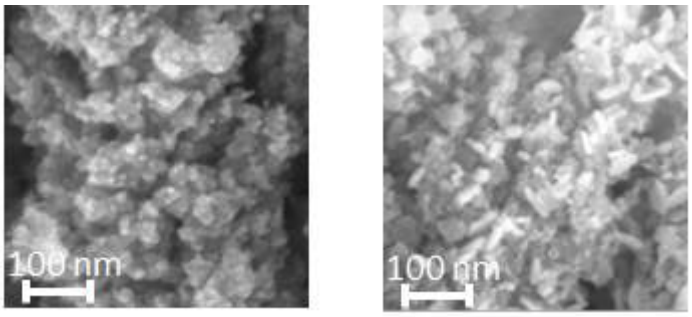

Figure 4.18: *SEM image of a portion of AZO nano-tree grown at 160 Pa O_2 before (left) and after (right) annealing in air [144].*

Another investigation regarding the filling of the conduction band in as-deposited and annealed samples was performed by analyzing the variations in the optical gap as measured by Tauc plots. As introduced in section 3.3, the intercept of a linear fit of the $(\alpha h\nu)^2$ vs. $h\nu$ curve with the $h\nu$ axis gives the minimum energy for an optical transition, i.e. the optical gap. In the presence of a heavy doping leading to a filling of the bottom of the conduction band with an electron density n, the optical gap is increased proportionally to $n^{\frac{2}{3}}$ according to the Moss-Burstein relation as discussed in section 1.1.1:

$$\Delta E_g^{MB} = \frac{\hbar^2}{2m^*}\left(3\pi^2 n\right)^{\frac{2}{3}} \tag{4.2}$$

As shown in figure 4.16.a, n is high for as-deposited films, with decreasing values for increasing deposition pressures, and low for films annealed in air. The results of Tauc analyses are presented in figure 4.19. As-deposited films show an enlargement of the optical gap by up to 400 meV with respect to undoped ZnO (green dashed line) at low deposition pressures. This shift is reduced as deposition pressure is increased, and becomes negligible (i.e. within experimental uncertainty) for porous films and air annealed compact films. This is in full agreement with the trends in n obtained from electrical measurements, confirming that the blueshift of the optical gap is due to the MB effect and that the annealing treatment in air does empty the conduction band as stated above. A linear regression on the optical gap values vs. $n^{\frac{2}{3}}$ allowed to obtain another estimate of the electron effective mass m^* from equation 4.2[1]. From the slope of the linear

[1]The term m^* in the equation actually corresponds to the reduced effective mass of the transition, which can be approximated to the electron conduction band effective mass since its value is expected to be much smaller than the hole valence band effective mass [153].

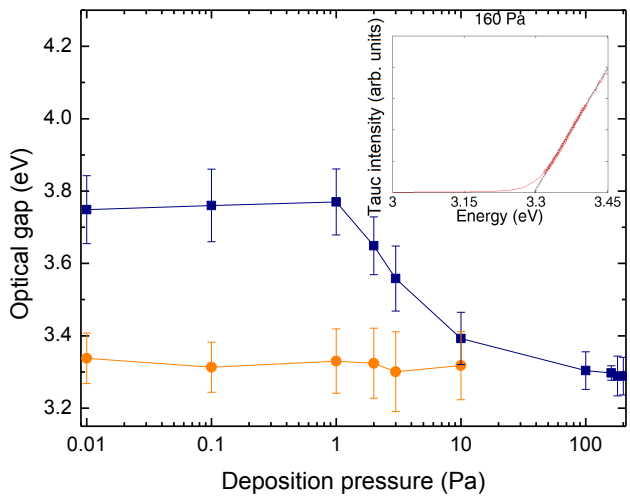

Figure 4.19: *Optical gap as a function of deposition pressure for as-deposited (blue squares) and air-annealed (orange dots) AZO layers. The green dashed line indicates bulk undoped ZnO bandgap. The inset shows an example of Tauc plot and linear fit [144].*

regression it was possible to estimate an electron effective mass of $m^* = 0.81\,m_0$, where m_0 is the electron rest mass. This value is likely to overestimate the actual effective mass because of many-body effects which tend to narrow the bandgap in opposition to the MB effect [25,26]. Other estimates of m^* in AZO calculated from MB shift are even higher ($m^* \approx 0.98 m_0$) [154] which points out other fine structure effects possibly due to nonparabolicity of the bands [27]. As a final remark, this estimate was performed under the hypothesis that variations in optical gap are mainly due to changes in conduction band carrier concentration and assuming that the band structure of the material is not strongly affected by structural variations, even though changes in the effective mass due to variation of the material structure may be expected when moving from compact sub-stoichiometric to nanoporous films.

4.2.2 Annealing in other atmospheres

The evidence that oxygen-related defects play a key role in determining the electrical and optical properties, which emerged unquestionably from the previous sections, led to the investigation of the effects of thermal treatments performed in oxygen-free atmosphere. Both vacuum and inert (Ar) annealing environments were used, with the aim of inducing oxygen desorption and changing defect

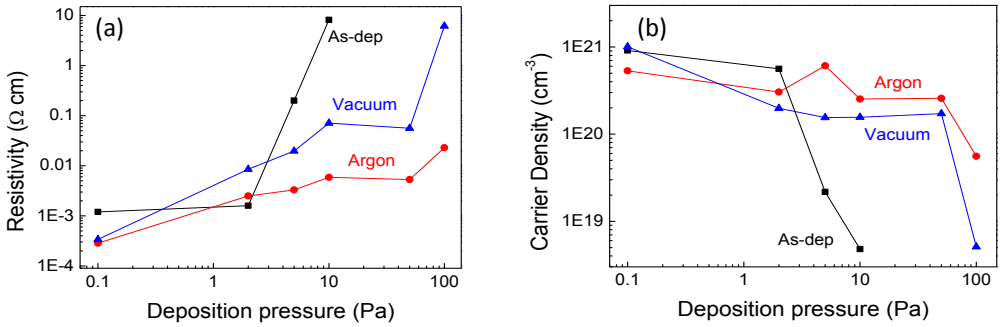

Figure 4.20: *Electrical conductivity (a) and carrier concentration (b) as a function of deposition pressure for as-deposited (black squares), vacuum-annealed (blue triangles) and Ar-annealed (red dots) AZO layers.*

concentration, improving the crystal structure and understanding the doping mechanisms. The annealing temperature was 500°C, the same employed for the thermal treatments in air described in the previous section[2]. The effects of treatments on electrical properties can be seen in figure 4.20, where the variations in electrical resistivity (fig. 4.20.a) and carrier concentration (fig. 4.20.b) upon annealing in vacuum and inert atmosphere are reported. For most deposition conditions, both thermal treatments in inert atmosphere and in vacuum sorted beneficial effects on electrical resistivity (which decreased at every deposition pressure but 2 Pa O_2). At high deposition pressures (5-10 Pa) resistivity decreases by 1-2 orders of magnitude upon vacuum annealing, and by 2-3 orders of magnitude for treatments in argon. Most noticeably, porous samples (100 Pa) which prior to the treatment were too resistive to be measured in the Van der Pauw conditions (see section 4.1.2) gained electrical conductivity upon annealing, with a resistivity value of 0.01 Ω cm for a 100 Pa sample annealed in Ar. Interestingly, porous samples annealed in Ar, which underwent this transition from insulating to conducting, reported an appearance of the anomalous Raman peak at 257 cm^{-1} mentioned in section 4.1 which has been empirically correlated with conductivity.

Examining figure 4.20.b allows to view the contribution of carrier density to this increase in conductivity. Treatments in vacuum or inert atmosphere provide

[2]Due to experimental reasons, the as-deposited samples which underwent the treatments in Ar and vacuum were not fully optimized and therefore their initial properties are slightly different from the ones described in sections 4.1 and 4.2.1. For a more coherent description of the effects of annealing, the data sets belonging to the actual annealed samples will be shown in this section: for this reason there will be some discrepancies between the functional properties of as-deposited samples in this section and in the rest of this work.

an increase in the carrier concentration of layers grown at 5-100 Pa, which is sufficient to account for the conductivity boost. The effects of annealing in Ar are in general more beneficial for carrier concentration, except for films grown at very low pressure (< 2 Pa) where a small decrease in n was measured.

Carrier mobility values are shown in figure 4.21.a. A significant increase

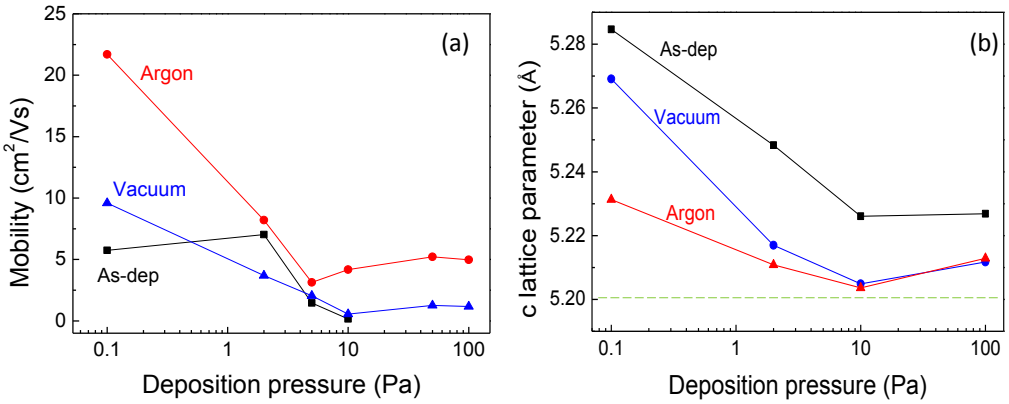

Figure 4.21: *Carrier mobility (a) and c lattice parameter (b) as a function of deposition pressure for as-deposited (black squares), vacuum-annealed (blue triangles) and Ar-annealed (red dots) AZO layers. The green dashed line indicates the reference bulk undoped ZnO c parameter [91].*

in μ is found for compact AZO samples grown at low (0.1 Pa) pressure and annealed in Ar (by a factor 4) or vacuum (by a factor 2). This can explain the increase in electrical conductivity mentioned above, despite the decrease in carrier concentration. In general, for any deposition pressure, thermal treatments in Ar increase the measured mobility values with respect to as-deposited samples. The benefits of annealing in vacuum are visible only at very low (< 2 Pa) or very high (> 10 Pa) deposition pressure.

From the structural point of view, c axis parameters (fig. 4.21.b) show a significant decrease upon annealing, indicating a relaxation towards the bulk ZnO value (green dashed line). This relaxation is stronger for annealing treatments performed in inert atmosphere, in agreement with results from electrical measurements. A straightforward explanation of this behavior is not easy to present, if both structural and electrical properties are taken into account: one plausible possibility is constituted by the migration of Al^{3+} cations from interstitial to Zn-substitutional position: since Al has a smaller atomic radius than Zn, the entrance of Al^{3+} in substitutional position can lead to a smaller lattice parameter [146] (similarly to what described in section 4.1) and simultaneously to an increase in

electrical conductivity due to effective activation of doping.

Results of optical characterization are reported in figure 4.22. The full

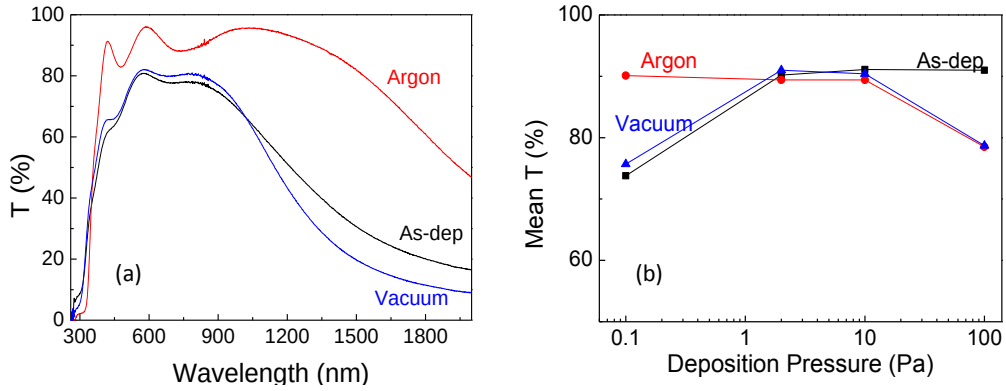

Figure 4.22: *Optical transmittance spectra of a compact AZO layer grown at 0.1 Pa before annealing (black), after annealing in vacuum (blue) and in Ar (red). (b) Average optical transmittance values as a function of deposition pressure for as-deposited (black), vacuum annealed (blue) and Argon annealed (red) AZO layers*

transmittance spectrum of an AZO layer grown at 0.1 Pa is shown in fig. 4.22.a, where a significant transmittance enhancement can be seen for the thermal treatment in Ar. Transparency is increased throughout the spectrum, and most noticeably in the IR range, in agreement with the decrease in carrier concentration shown in figure 4.20. The spectrum of the sample annealed in vacuum does not exhibit major changes with respect to the as-deposited one. Figure 4.22.b allows to compare the average values (in the 400 nm-700 nm) of optical transmittance for different AZO layers which underwent the thermal treatments. No significant alterations are present in the mid-pressure range (1-10 Pa). In the case of porous samples, on the contrary, optical transmittance is decreased from 90% to 80% for both annealing conditions: this is an evidence of the fact that the dramatic increase in electrical conductivity (and especially carrier density) is accompanied by the formation of structural defects. Once again, haze values were not affected by the thermal treatments, confirming that light scattering in AZO nanoforests is mainly a morphology-driven feature.

4.2.3 Effects of Al doping

To investigate the effects of the presence of Al as an extrinsic dopant in AZO, undoped ZnO films were synthesized in identical conditions and compared in terms of morphology, structure and functional properties. Examples of the obtained morphologies can be seen in figure 4.23. The effects of deposition

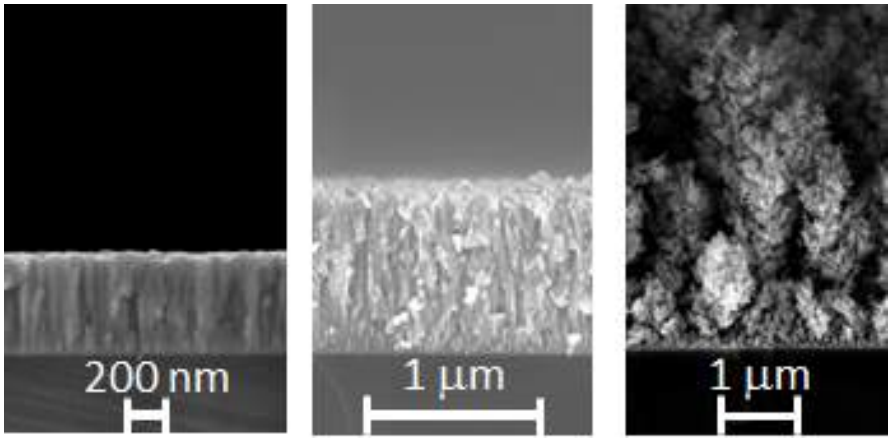

Figure 4.23: *Cross-sectional SEM images of undoped ZnO layers grown at 2 Pa (left), 100 Pa (center), 500 Pa (center) O_2 deposition pressures.*

pressure on film morphology were comparable to what observed for AZO layers, but ZnO films appeared generally more compact than AZO grown at the same deposition pressure: columnar compact films are synthesized for pressures up to 10 Pa, nanostructuring emerges around 100 Pa without visible porosity, and the development of porous hierarchical nanoforests emerged at higher pressures (200 Pa - 500 Pa).

In terms of structural properties, a comparison between results from XRD measurements on AZO and ZnO films is presented in figure 4.24. The c parameter values reported in figure 4.24.a indicate a shift towards higher values at low pressures, both for ZnO and AZO: the deformation in the undoped ZnO lattice is significantly less marked than in the case of AZO, even though in both cases the structure tends towards relaxation at higher pressures. This discrepancy can be explained by considering that Al^{+3} cations in the interstitial can introduce additional disorder or stress with respect to intrinsic defects (Zn interstitials and O vacancies) present also in undoped ZnO. Similarly, the mean domain size calculated from Scherrer's formula on the (002) peak (fig. 4.24.b) is generally larger in ZnO than in AZO, with the exception of AZO grown at 2 Pa which showed peculiar properties as discussed in the previous sections. The analysis of

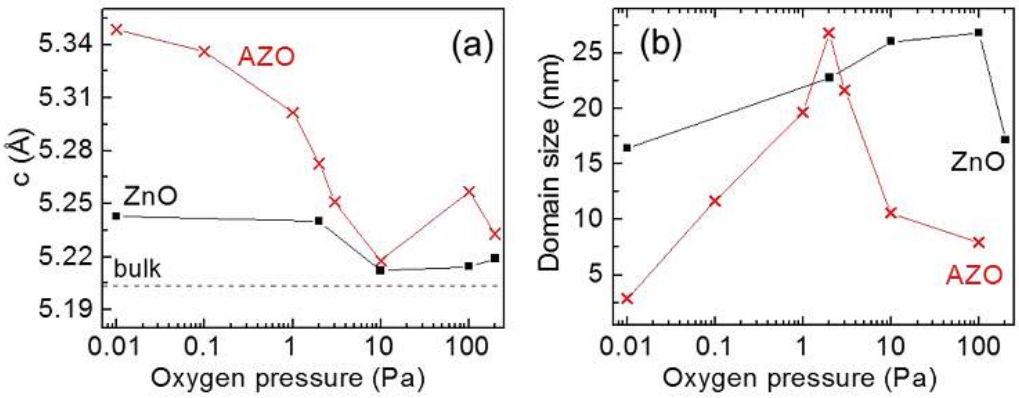

Figure 4.24: *Variation of the lattice parameter c (a) and the mean domain size (b) with oxygen deposition pressure for ZnO (black) and AZO (red) films [147].*

local order by Raman spectroscopy pointed out a structural interplay between Al dopants and O vacancies, since oxygen stoichiometry (evaluated from the relative intensity of the Zn- and O-sublattices Raman peaks) is reached at lower deposition pressures in undoped ZnO than in AZO (approximately 2 Pa for ZnO and 80 Pa for AZO).

The average visible optical transmittance of ZnO and AZO layers is shown in figure 4.25. The reported mean values exhibit similarities both in terms of

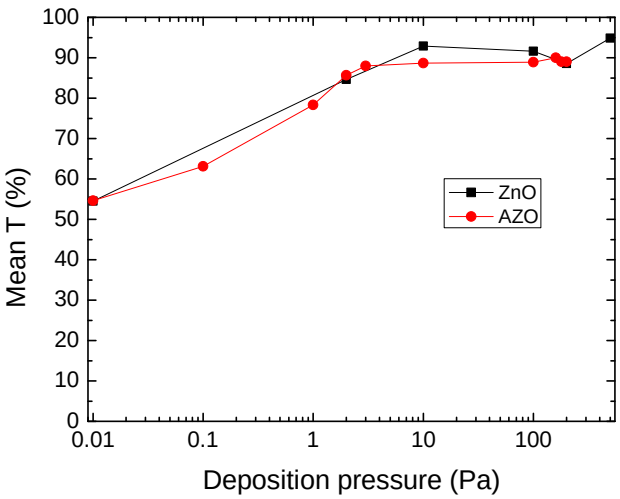

Figure 4.25: *Mean optical transmittance (400 - 700 nm) of AZO (red dots) and ZnO (black squares) as a function of deposition pressure.*

dependence on pressure and of absolute values. This is an interesting fact, showing that the greater structural disorder detected in AZO is somewhat compensated

by a greater fraction of voids due to porosity, making the total transmittance not significantly affected by doping. The similar values at very low pressure indicate that defects such as Zn interstitials and O vacancies, whose presence is suggested by XRD and Raman measurements in both film categories, play an important role in the creation of mid-gap states leading to a decrease in visible optical transparency.

Unfortunately, a systematic characterization of electrical properties of undoped ZnO was not possible due to stability problems which were met after depositions: on one side, ZnO films grown on glass at low pressure presented adhesion problems which led to a quick delamination making the electrical measurements impossible. On the other, films deposited at pressures of 2 Pa exhibited scarce stability of electrical properties: a relatively low resistivity of (10^{-2} $\Omega\,\mathrm{cm}$) was detected shortly after deposition, but the electrical properties were compromised within few days. This fact, possibly connected with a metastable nature of electrical conductivity in some TCOs (a very recent hypothesis emerging in the TCO research community [42]) is interestingly in contrast with what reported for AZO compact films (0.1 - 2 Pa range), which only exhibited conductivity variations within 5% over a timescale of several years. All undoped ZnO films deposited at pressures of 10 Pa and higher were too resistive to measure at any time.

4.3 Summary

AZO thin films were grown by room temperature PLD in different O_2 background pressures. All depositions were also performed on flexible ETFE substrates to test compatibility with polymer-based devices. Compact films were obtained at low (<10 Pa) deposition pressures, with state of the art properties at 2 Pa ($\rho \approx 4 \cdot 10^{-4}\ \Omega\,\mathrm{cm}$, $T \approx 85\%$ in the visible range) depending on a compromise between competing effects of oxygen-related defects: at lower pressures, high defect concentrations were detrimental for optical properties, and at higher pressures grain boundaries and oxygen stoichiometry led to a decrease in electrical conductivity. Local structural order is strongly affected by oxygen content, as demonstrated by XRD and Raman spectroscopy, and by investigating the effects of thermal treatments in oxidizing atmosphere. In particular, oxygen vacancies are detrimental for structural and optical properties, but contribute to improving electrical conductivity.

Mesoporous forest-like hierarchical structures were obtained at high (> 10 Pa) deposition pressures, with optimal transparency and light scattering properties ($T > 85\%$, $H > 80\%$) due to a locally ordered structure with ZnO stoichiometry, and to the effects of morphology at the mesoscale. The open morphology of porous AZO layers leads to the lack of uniformly connected in-plane conduction paths, resulting in an electrical resistivity of the order of 1 MΩ cm.

These results were used as a basis for an in-depth analysis of the structure/property relation in AZO, which allowed to investigate the mechanisms leading to the filling of the conduction band: an analysis of the Moss-Burstein effect and of the refractive index/absorption coefficient led to two independent estimates of the electron conduction band effective mass. The effects of thermal treatments in different atmospheres and a comparison with undoped ZnO films synthesized in analogous conditions gave further insight on the relationship between defects and functional properties.

The discussion reported in this chapter, which explains how it is possible to understand the interplay between morphology, structure and functional properties of AZO, will be used as a starting point for chapters 5 and 6, where the knowledge of the structure/property relation will be exploited to achieve independent control of electrical and optical properties to develop novel nano- and mesostructured AZO layers with a unique tunability of functional properties.

Part III

Novel AZO nano- and mesoarchitectures

5

Electrically conducting nano-forests

This chapter describes a novel approach to obtain mesoporous, large surface area AZO layers simultaneously characterized by electrical conductivity, optical transparency and light scattering capability. The development of this approach is based on considerations deriving from the most significant results presented in chapter 4 about the control of structure and properties of AZO thin films by PLD. The chapter begins by describing the motivations and development of this approach in section 5.1, then the main results are presented in section 5.2, followed by a description of advanced characterizations pertaining to cross-plane conductivity in section 5.3.

5.1 Depositions in mixed atmospheres

The dependence of optical and electrical properties of AZO layers on structure, morphology and deposition conditions, as discussed in the previous chapter, is characterized by a complex role played by the oxygen pressure in the deposition chamber. On the one hand, a high deposition pressure (100 Pa O_2 or higher) is required for the development of mesoporous hierarchical AZO nanoforests, whose morphology is optimal for light scattering and results in haze values as high as 80%, and whose large surface area is interesting for PV applications. This requirement derives from the properties of the PLD deposition technique, in which clustering and hierarchical assembly occur only at high pressures due to collisions between the ablated species and the background gas. On the other hand, oxygen plays a crucial role in the determination of electrical conductivity and optical transparency: a complex interplay between O vacancies, Al^{3+} dopants and possibly other unintentional electron donors (i.e. H^+) was detected, whose effects, along with properties of grain boundaries and nanoscale porosity, maximizes electrical conductivity at low ($\approx$ 2 Pa) oxygen deposition pressure. Furthermore, in terms of optical transparency, a higher O content is beneficial for the suppression of mid-gap states which increase visible light absorption at oxygen pressures up to 2 Pa. It is therefore clear that the possibility to obtain separate control of electrical conductivity, optical transparency and light scattering would be appealing in order to be able to combine these properties into the same material.

A first approach which was developed to reach this goal consists in performing PLD in mixed atmospheres constituted by oxygen and an inert gas. If the total pressure ($p_{TOT} = p_{O_2} + p_{inert}$) in the chamber is maintained at a sufficiently high value, hierarchical porous layers can be obtained. If, for this high value of p_{TOT}, p_{O_2} is varied, the oxygen content in the film can be controlled to some extent, and the functional properties of interest (in particular, electrical conductivity) can be obtained in the nano-forests. In other words, it is possible to uncouple morphology from stoichiometry (which in the case of depositions in pure O_2 are intrinsically coupled) using the inert gas partial pressure to control morphology and the O_2 partial pressure to control stoichiometry.

The inert gas was chosen by investigating the possibility to obtain forest-like structures: both He and Ar were tested. Due to the atomic mass of Ar being 10 times heavier than the one of He, the effects of collisions between the ablated

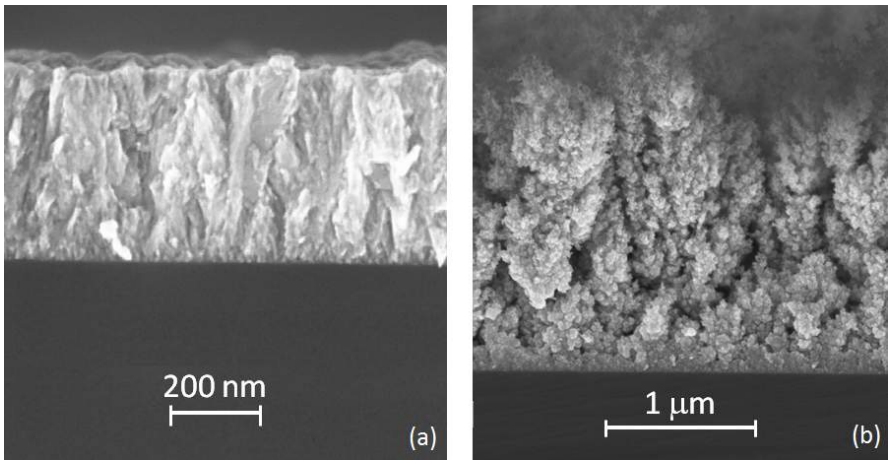

Figure 5.1: *Cross-sectional SEM images of (a) an AZO layer grown in a He:O_2 atmosphere, at a total pressure of 400 Pa, with d_{TS} = 6 cm (b) an AZO layer grow in an Ar:O_2 atmosphere at a total pressure of 200 Pa, with d_{TS}=5 cm.*

species and the inert fraction of the background gas are very different in the two cases. In particular, the ablation plume in the presence of helium is less confined and the kinetic energy with which the substrate is reached is higher due to the smaller mass of He atoms leading to less significant energy decrease in inelastic collisions. In order to perform *out of plume* depositions ($L > 1$) in He atmospheres, both the total pressure and the target-to-substrate distance were increased. Figure 5.1.a shows a SEM image of an AZO layer grown in a He:O_2 atmosphere at a total pressure of 400 Pa (2% O_2) with d_{TS}=6 cm. In spite of the high pressure, the obtained morphology is too compact to obtain effective light management properties even attempting to increase d_{TS}. Figure 5.1.b shows an AZO layer deposited in a mixed Ar:O_2 atmosphere at a total pressure of 200 Pa: the morphology is characterized by hierarchical tree-like structures similar to the ones obtained in pure oxygen (see for example fig. 4.2 and related discussion). This similarity is probably due to the relatively close values of the atomic mass of Ar and the molecular mass of O_2 (their ratio is ≈ 1.25), resulting in comparable energy loss upon inelastic collisions with the ablated species. As a consequence, analogous morphologies are obtained without the need of increasing the target-to-substrate distance, which can negatively affect deposition rate.

The total deposition pressure for the development of electrically conducting nano-forests was chosen in the 100-110 Pa range, with the aim of having mesoscale light scattering features without exceeding in porosity and spatial separation, thus avoiding to increase electrical resistivity by reducing the connectivity

between nano-trees. The oxygen fraction was varied to investigate whether it is actually possible to achieve control of electrical and optical properties through stoichiometry without altering the morphology of the AZO layers.

5.2 Results and discussion

5.2.1 Morphology, structure and chemical composition

Hierarchical AZO layers were grown at a total deposition pressure of 100-110 Pa, with different Ar:O_2 partial pressure ratios. Examples of the obtained morphologies are presented in the cross-sectional SEM images of figure 5.2. In

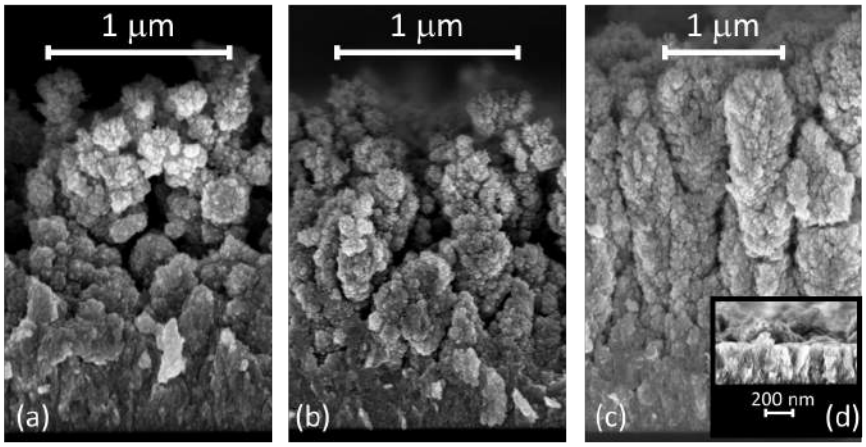

Figure 5.2: *Cross sectional SEM images of hierarchical AZO layers grown at a total deposition pressure of 110 Pa, with 2.5% O_2 (a), 10% O_2 (b) and 100% O_2 (c). The inset (d) shows a 300 nm layer grown at 100 Pa (2% O_2).*

particular, the O_2 partial pressure was 2.5% for fig. 5.2.a, 10% for fig. 5.2.b and 100% (pure oxygen) for fig. 5.2.c. respectively. The images show the gradual arise of a preferential growth direction orthogonal to the substrate surface, enhancing the hierarchical nature of the material which resembles a nanotree forest in the case of pure oxygen (fig. 5.2.c). This evolution is similar to what observed as an effect of an increase in gas flow rate, for the case of depositions in pure oxygen, as discussed in section 4.1. Regardless of the deposition parameters, the bottom layer of the film is more compact and uniformly connected, then the structure of the material becomes more open and porous, moving away from the substrate. In this porous region the influence of the background deposition atmosphere is more significant, and the forest-like morphology appears only at high oxygen content. A 300 nm film grown at 100 Pa with an O_2 partial pressure of 2% is also shown in the inset 5.2.d as a reference to examine the more compact morphology corresponding to the earlier growth stages, also visible in the thicker films of figs.5.2.a-c. As a general result, partly anticipated in section 5.1, the possibility to grow AZO nano-forests in mixed Ar:O_2 atmospheres, with features at the mesoscale for different

partial pressure ratios, was thus demonstrated.

The structure of these layers was probed by XRD measurements, whose main results are presented in figure 5.3. The most intense reflections of ZnO powders

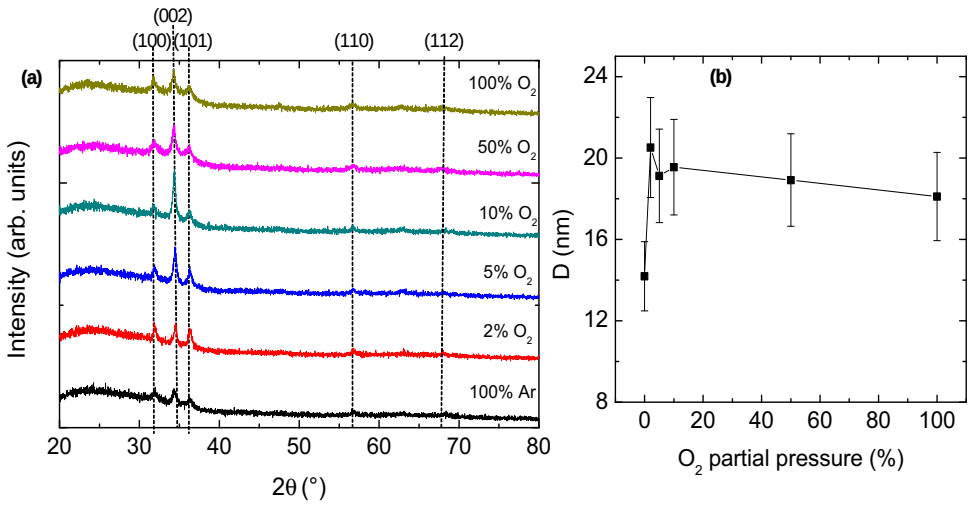

Figure 5.3: *(a) XRD patterns of porous AZO layers (300 nm thick) grown at 100 Pa with different oxygen partial pressures. The most intense reflections of ZnO powders are present, with hints of a preferential orientation in the (002) direction. (b) Mean domain size D, calculated from Scherrer's formula on the (002) peak, as a function of oxygen partial pressure.*

appear in the diffractograms; however, the peak intensity ratio suggests a slightly preferential orientation along the (002) direction. The mean size of the crystal domains was calculated from Scherrer's formula on the (002) peak and the values are reported in fig.4.5.b. The calculated domain size is of the order of 20 nm for all oxygen partial pressures, except for the case of pure argon (oxygen-free atmosphere), with a mean domain size of about 14 nm. This can be interpreted as an indication of the presence of O vacancies in the lattice, similarly to what discussed in section 4.1, suggesting that it is actually possible to obtain sub-stoichiometric AZO layers with mesoscale porosity. Calculations of the c lattice parameter from Bragg's formula (not shown) were also performed, indicating only small variations from the ZnO reference value, corresponding to the very small shifts visible in fig. 5.3. However, neither the degree of preferential orientation nor the c parameter shift are comparable to the compact AZO films grown in oxygen described in section 4.1, where the intensity of the (002) peak was higher than all other reflections by up to 4 orders of magnitude, and where relative shifts in c as high as 5% were found.

In order to provide a confirmation of the correlation between oxygen partial

pressure during deposition and oxygen stoichiometry in the films, selected AZO layers were probed by X-ray Photoemission Spectroscopy (XPS) and Scanning Photo Emission Microscopy (SPEM), with synchrotron X-ray radiation at 650 eV as an excitation source. In particular, variations in the Zn/O stoichiometry ratio were estimated by acquiring point XPS spectra in different regions of the cross-section of the nano-forest layers, with a focused X-ray beam with a minimum spot size of 200 nm. Measurements were performed on layers grown at a total pressure of 110 Pa, both in pure O_2 and in 6% O_2 atmosphere. Samples with a thickness over 10 µm were used in order to estimate the composition in different points by cross-sectional measurements with focused beam. According to the approach by Islam et al. [155] for Al-doped ZnO, the Zn 3d and O 1s photoemission lines were used to estimate stoichiometry from the following relation:

$$\frac{n_O}{n_{Zn}} = \frac{I_O}{I_{Zn}} \frac{\sigma_{Zn}}{\sigma_O} \frac{\lambda(E_{Zn3d})}{\lambda(E_{O1s})} \tag{5.1}$$

where I is the integral intensity of the peak, σ the photoionization cross-section at the incoming X-ray wavelength (approximately 0.34 and 0.18 Mbarn for O and Zn, taken from refs. [156, 157]), λ the electron escape depth at the corresponding kinetic energy (approximately 7 Åat E_O and 24.5 Åat E_{Zn}, respectively [158]). The obtained average values of the n_O/n_{Zn} ratio were employed to estimate the variations in stoichiometry due to differences in the deposition atmosphere: the O/Zn ratio for AZO grown at low (6%) oxygen partial pressure was 70% of the O/Zn ratio of stoichiometric (100% O_2) AZO. This significant variation allows to safely state that the oxygen partial pressure during deposition directly influences the stoichiometry of the material even though a precise quantitative determination is not possible.

The possibility to perform SPEM measurements with a lateral resolution of hundreds of nanometers was also employed to acquire spatial maps of the distribution of Al, Zn and O elements in different regions of the nano-forests by comparing the relative intensities of the corresponding photoemission peaks. Figure 5.4.a presents a map of the distribution of Al atoms (evaluated from the Al 2p photoemission peak) over the cross-section of an AZO layer grown at 110 Pa O_2, with the corresponding SEM image in fig. 5.4.b. In the map, darker colors correspond to higher aluminum concentrations: it is possible to see how there is a tendency for Al to accumulate in the top part of the layer. Interestingly, this result was found regardless of the partial pressure ratio during deposition,

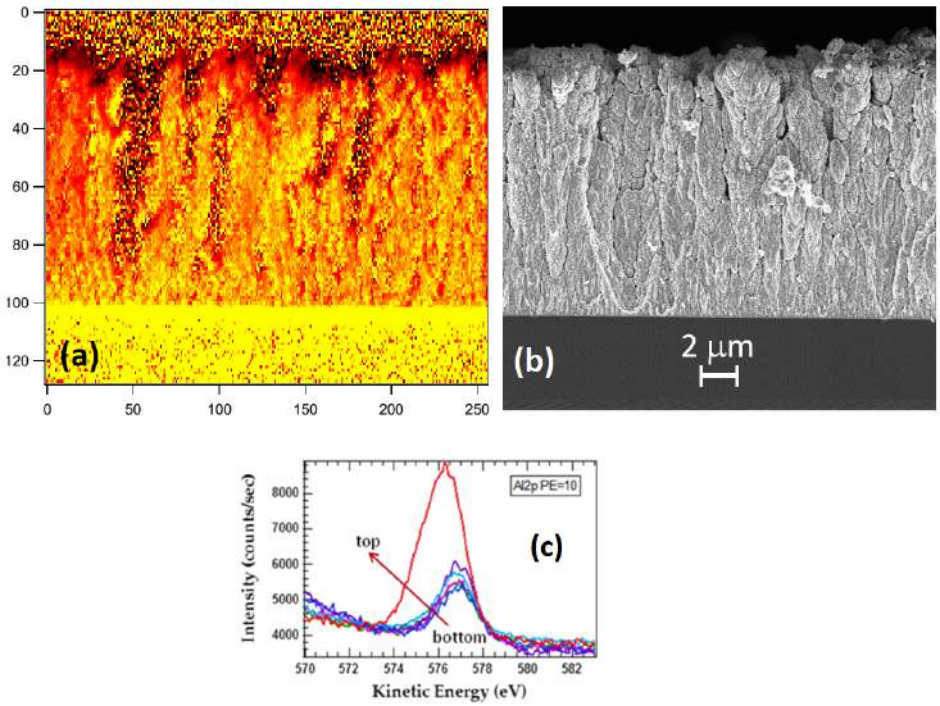

Figure 5.4: *(a) Map of the distribution of Al, evaluated from the Al 2p photoemission peak, over a nano-forest of AZO grown at 110 Pa O_2. (b) Cross-sectional SEM image of the same region. (c) Evolution of the Al 2p photoemission peak from single point spectra.*

suggesting possible segregation effects. This behaviour was also confirmed by point spectra acquired in different regions, as shown in figure 5.4.c. A simple explanation to this phenomenon is difficult to formulate, especially considering that all depositions were performed at room temperature from a uniform target, and the samples did not undergo any thermal treatment which could drive Al migration. This result confirms that a complex interplay between the Al dopant and the ZnO structure is present, as already suggested by results presented in chapter 4, which needs further investigation.

5.2.2 Optical properties

The investigation of optical transparency and light scattering was carried out by measuring the total transmittance and haze for AZO grown in different Ar:O_2 mixtures and with different thickness values. By comparing the optical properties for films of different thickness it was possible to estimate the attenuation coefficient α, whose average values for different thickess are shown in figure 5.5.a.

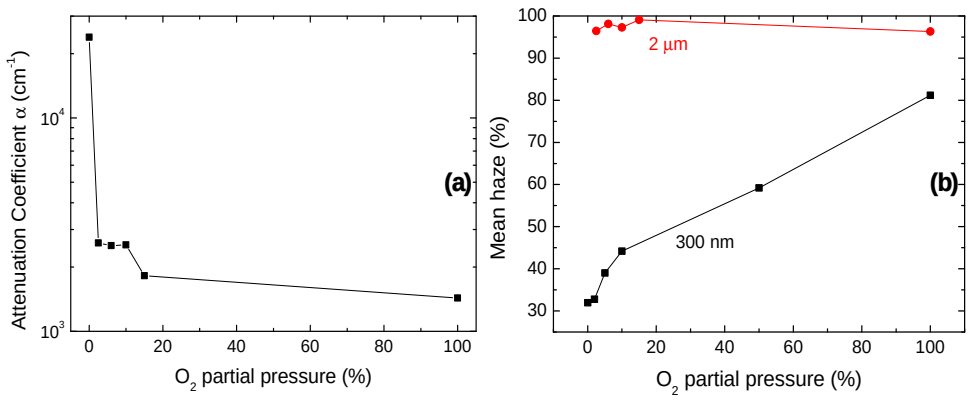

Figure 5.5: *(a) Attenuation coefficient as a function of O_2 partial pressure. (b) Haze factor as a function of O_2 partial pressure for AZO layers of different thickness*

The values of the attenuation coefficient show a significant decrease as the oxygen partial pressure is increased: AZO grown in pure Ar is strongly absorbing in the visible range ($\alpha \approx 2.8 \cdot 10^4\,\mathrm{cm}^{-1}$) and then the attenuation coefficient decreases by over one order of magnitude as the oxygen content in the deposition chamber (hence in the film) increases, down to 1400 cm^{-1} for a pure O_2 deposition atmosphere. The calculated values of α (Lambert-Beer's law was employed since reflectance is negligible in the visible) were consistent for layers of different thickness, and in agreement with the estimates reported in section 4.1.3 for

depositions performed in pure oxygen. The mean transmittance of 300 nm thick films is of the order of 90% (except for the case of pure Ar, with $T \approx 55\%$). For 2 μm thick layers T is of the order of 60% (in this case, 2 μm thick AZO layers grown in an oxygen free atmosphere were completely opaque to visible light, even at eyesight). This trend in optical transparency can be interpreted as a successful control of optical properties through variations of ZnO stoichiometry. In fact, the influence of oxygen vacancies on optical transparency which was identified in section 4.1.3 allows to state that these measured trends in transmittance correspond to the achievement of control over mid-gap defect states associated with oxygen content, by a variation of the Ar:O_2 partial pressure ratio.
Figure 5.5.b shows the average (400 nm - 700 nm) haze values for AZO films of different thickness, as a function of O_2 partial pressure. Two different thickness values are shown as an example, since in the case of haze there is not a simple relation analogous to Lambert-Beer's law to estimate the effects of thickness. The values reported in figure 5.5.b show that at low thickness there is an increase of haze with the oxygen content (i.e. with a more open morphology), whereas in the case of thick films haze is almost constant and close to unity, meaning that virtually all the transmitted photons are scattered by the hierarchical structures. This means that it is possible to achieve control of light scattering in mesoporous AZO by varying either the oxygen partial pressure or the film thickness, and it is possible to know how both parameters influence total transmittance by using Lambert-Beer's law on the values in fig. 5.5.a.

5.2.3 Electrical properties

The in-plane electrical resistivity of hierarchical AZO layers is reported in figure 5.6, as a function of O_2 partial pressure during deposition and for different thickness values. The measurements were performed in the 4-point probe configuration for resistivities up to 100 $\Omega\,\mathrm{cm}$, and in 2-wire configuration for higher values. As introduced in section 4.1.2, for porous samples such as the 2 μm thick ones (see fig. 5.2), the measurements needed to be performed by depositing the samples on evaporated contacts due to the impossibility of applying electrical contacts on the top.

There is an extremely significant increase in resistivity with increasing oxygen content, ranging from 0.3-0.4 Ω cm for oxygen-deficient AZO (O_2 partial pressure $\leq 2.5\%$) to the order of $10^6\,\Omega$ cm for the case of depositions in pure O_2. This

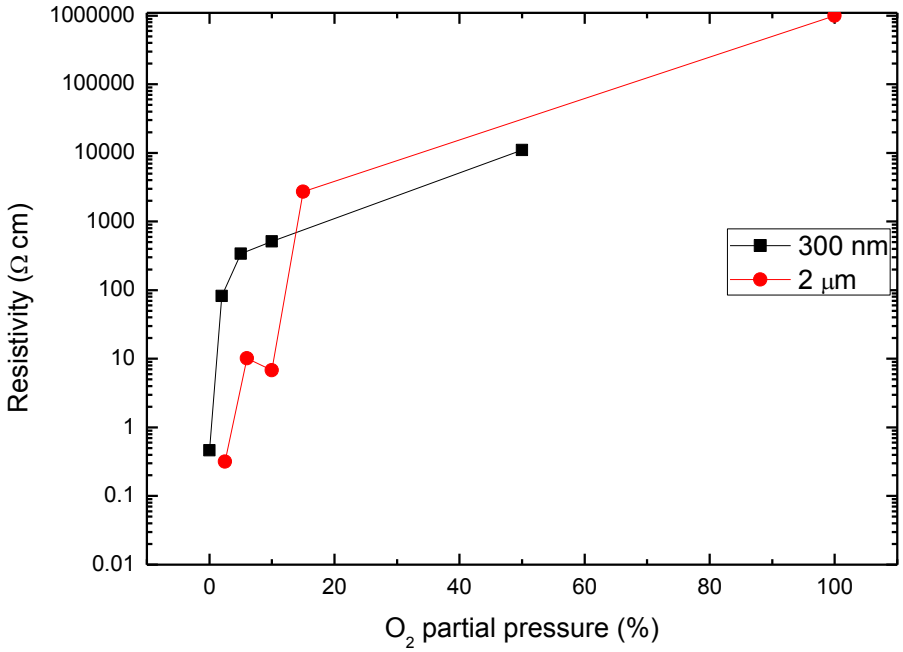

Figure 5.6: *In-plane electrical resistivity of hierarchical AZO layers of different thickness, as a function of oxygen partial pressure during deposition.*

increase by many orders of magnitude is observed both for 300 nm and 2 μm thick films; in the case of 300 nm layers the resistance of the samples grown in pure oxygen was out of the instrumental range. In the region of O_2 partial pressures between 2% and 10% the resistivity of thinner films is higher: a similar effect of thickness was observed also for compact AZO films (see section 4.1.2), and in this case it may have been enhanced by the fact that resistivity measurements on thicker films were performed by injecting the current at the substrate/film interface rather than from the top. In any case, the observed trends show the importance of oxygen defects (or in general of oxygen content) in determining the electrical properties of AZO, whose resistivity spans across 7 orders of magnitude as a result of variations in the O_2 partial pressure during deposition. In principle it is not possible to exclude an influence of morphology on these values, considering also the similar trend in haze (see figure 5.5.b). Unfortunately, it was not possible to perform reliable Hall effect measurements on nano-forests due to the very low V_H signal, which is likely to be a consequence of the nonuniform connectivity due to porous morphology, therefore no reliable carrier concentration and mobility data are available.

The time stability and durability of electrical properties was investigated by monitoring the evolution of electrical resistivity in the month following film deposition. The results of this characterization are presented in figure 5.7. Unlike

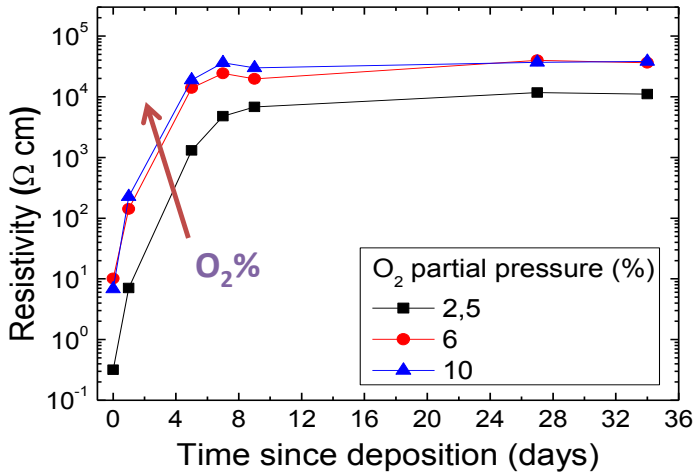

Figure 5.7: *Evolution of electrical resistivity as a function of ageing time for hierarchical AZO layers grown at different Ar:O_2 partial pressure ratios.*

compact AZO, whose many-year durability in terms of electrical properties was already mentioned in section 4.2.3, the electrical resistivity of nano-forests is subject to a rapid increase in the days following film synthesis. In fact, regardless of the initial value, the measurements report an increase in electrical resistivity by a factor $10^3 - 10^4$ within one week. One possible explanation to this degree of instability can be found in interaction with humidity from the environment (ageing took place in ambient conditions), leading to accumulation of OH^- from water vapor at grain boundaries, as recently reported in recent ageing studies conducted on AZO [159]. This phenomenon, which in compact films occurs mainly at the surface, raises the height of the grain boundary potential barrier (see eq. 2.1) decreasing carrier mobility. In mesoporous films with a very high surface-to-volume ratio, this decrease is bound to be more important, leading to a quick degradation of electrical properties. Interestingly, moving the samples to a vacuum environment after degradation allows a partial recovery of electrical resistivity (2-3 orders of magnitude), even without heat treatments: this can give a confirmation of the role played by humidity in degradation of electrical transport properties.

5.3 Cross-plane electrical transport

The electrical transport properties of the nano-trees along the tree axis, which are of primary importance when considering applications of AZO as a photoanode, were investigated by two independent approaches. Due to the difficulty of applying electrical contacts on the surface of porous AZO layers, which was already mentioned in the previous sections, a macroscopic cross-plane measurement involving the whole film was not possible.
For this reason, both approaches are based on local (microscale) measurements. In particular, the first approach (in collaboration with the University of Modena and Reggio Emilia) consisted in measuring the electrical resistance of a bundle of nano-trees by employing a micrometrical W tip to apply a known voltage from the conducting substrate (ITO) to the top of a bundle, as depicted in figure 5.8.a, and measure the corresponding current flow. The measurements were performed in vacuum, inside a SEM chamber, by applying bias voltage cycles of amplitude 200 mV (0 V → +0.2 V → -0.2 V → 0 V). Fig. 5.8.b shows a SEM image of the W

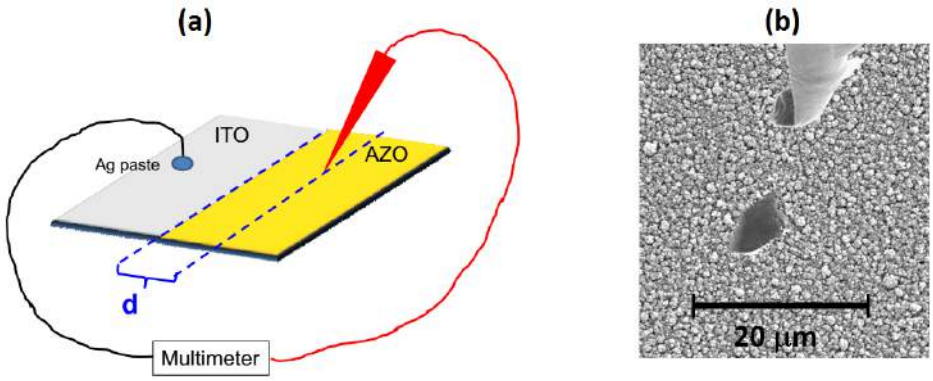

Figure 5.8: *(a) Scheme of cross-plane electrical measurements. (b) SEM image of the trace left by the W tip on a nano-forest.*

tip employed for the measurements, whose trace on the top of a the nano-forest is visible at the center of the image. The calculated area of the print is of the order of 20-30 μm^2. Hierarchical AZO layers grown with variable Ar:O_2 pressure ratios were measured with this setup, acquiring I-V curves with different contact-to-tip distances (the blue d in figure 5.8.a) and varying also the time interval t between measurements and the applied pressure on the nanotree top, which was minimized by trial and error. Examples of I-V curves for AZO layers grown at 6%, 10% and 100% O_2 partial pressures are reported in figure 5.9. The main features of these results can be summarized as follows:

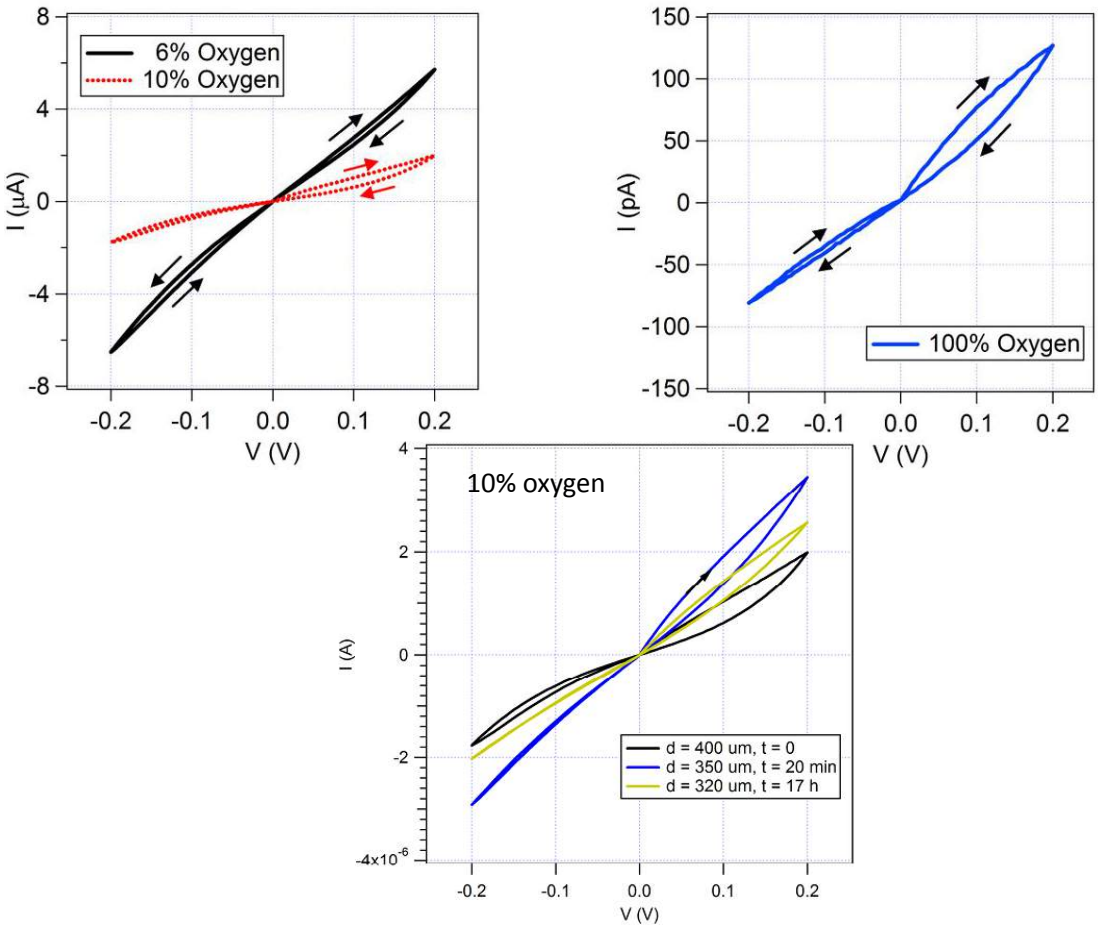

Figure 5.9: *(top) I-V curves of hierarchical AZO layers (2 μm thick) grown in different Ar:O_2 atmospheres. Arrows denote the voltage sweep directions, corresponding to one bias voltage cycle. (bottom) Effects of variations in contact-to-tip distance d and time interval t between measurements, for a sample grown at 10% O_2. (Courtesy of G. C. Gazzadi and V. De Renzi, UniMoRe, Italy)*

- All the I-V curves were characterized by a non-linear shape, emerging more strongly at higher O_2 partial pressures. This behaviour can be due to a Schottky-type barrier between the W tip and the AZO surface [91], and possibly enhanced by non-ohmic conduction mechanisms resulting from discontinuous distributions of the conduction paths.

- A hysteresis effect is present, which is probably caused by charge trapping effects in mesoporous structures. This effect is stronger in less conducting films (higher O_2 partial pressures) as well, recalling a memristor-like behaviour which has recently been reported for compact AZO layers [160, 161].

- For each deposition condition, variations in d and t have a strong influence on the shape of the curves and on the absolute value of the measured current intensities. The measured data are heavily scattered, and appear to depend also on the mechanical pressure exerted by the W tip. These considerations, as well as the very low values of the measured current (especially for films grown in pure oxygen) and the uncertainty about the exact number of nanotrees involved in each bundle, force data interpretation to be considered only as a reliable estimate of the order of magnitude of cross-plane electrical resistance.

- The estimated resistance orders of magnitude were 10 KΩ for layers grown at 6% O_2, 100 KΩ at 10% O_2 and 10 GΩ at 100% O_2. Knowing film thickness (2 μm) and assuming that the current flows in a column whose section equals the diameter of the tip ($\approx 20 - 30$ μm^2) it is possible to have an estimate of the order of magnitude of cross-plane electrical resistivity in hierarchical AZO nano-forests. Interestingly, there is compatibility between the values calculated with this approach (ranging from 10 Ω cm to 1 MΩ cm) and the measured in-plane resistivity values reported in figure 5.6.

- The hypothesis that the current flows preferentially in the vertical (cross-plane) direction has been confirmed by isolating a 5x5 μm trench with a Focused Ion Beam (FIB) down to the ITO substrate and repeating the I-V measurements with the W tip inside and outside the FIB-milled square. The measured current values (without alterations in the I-V curve shape) were reduced by 75% if the tip was placed on top of the isolated area (i.e. when vertical current transport was impeded), indicating that 75% of the current does actually flow in a vertical column from the W tip to the ITO substrate.

- It is not possible to exclude that the cross-plane resistivity values can be higher in as-grown AZO nano-forests, since this analysis was carried out several weeks after deposition, when the degradation of electrical properties discussed in section 5.2.3 had already taken place. If this degradation mechanisms is similar for in-plane and cross-plane electrical transport, the vertical conductivity of the as-grown AZO layers can be expected to be higher.

The investigation of cross-plane electrical transport properties was also performed through an indirect approach, based on Scanning Photo Electron Microscopy (SPEM). The basic principle of this approach (which was recently developed to measure the conductivity of spatially separated nanowires [162]) consists in acquiring photoemission spectra in different points along the growth direction and monitoring the shift due to charging effects: the photoemitted electrons are not effectively compensated by electrons from the (grounded) substrate if the electrical conductance of the measured structure is too low to permit an easy electron flow from the substrate to the top. This results in the build up of a surface potential, leading to a rigid shift in the kinetic energy of the photoemitted electrons, which increases proportionally to the distance from the substrate x, according to the relation [162]

$$\Delta E_k = C\frac{x}{\sigma}A_x \tag{5.2}$$

where C is a parameter depending on the beam properties (photon flux, irradiated area, electron yield), σ is the electrical conductivity and A_x the nanostructure cross-section at a distance x from the substrate, estimated from SEM measurements. Equation 5.2 shows that the peak shift is inversely proportional to σ, meaning that if conductivity is too high the shift may not be detectable (in highly conducting nanostructures, electrons coming from the substrate can easily travel along the nanostructure, managing to screen the positive charges deriving from photoejected electrons). The measurement was performed on thick (10-15 µm) AZO nano-forests grown in different Ar:O_2 atmospheres, in order to estimate the effects of oxygen content on cross-plane conductivity. SPEM maps of the whole forest cross-section were acquired from the Zn 3d, O 1s and Al 2p core levels. Figure 5.10.a shows the map obtained from the Zn 3d level on a sample grown at 100% O_2. A set of points (marked with letters from A to E on the figure) were selected from the map as a possible conduction path for electrons along the nanotree axis. In correspondence to those points, XPS spectra of the

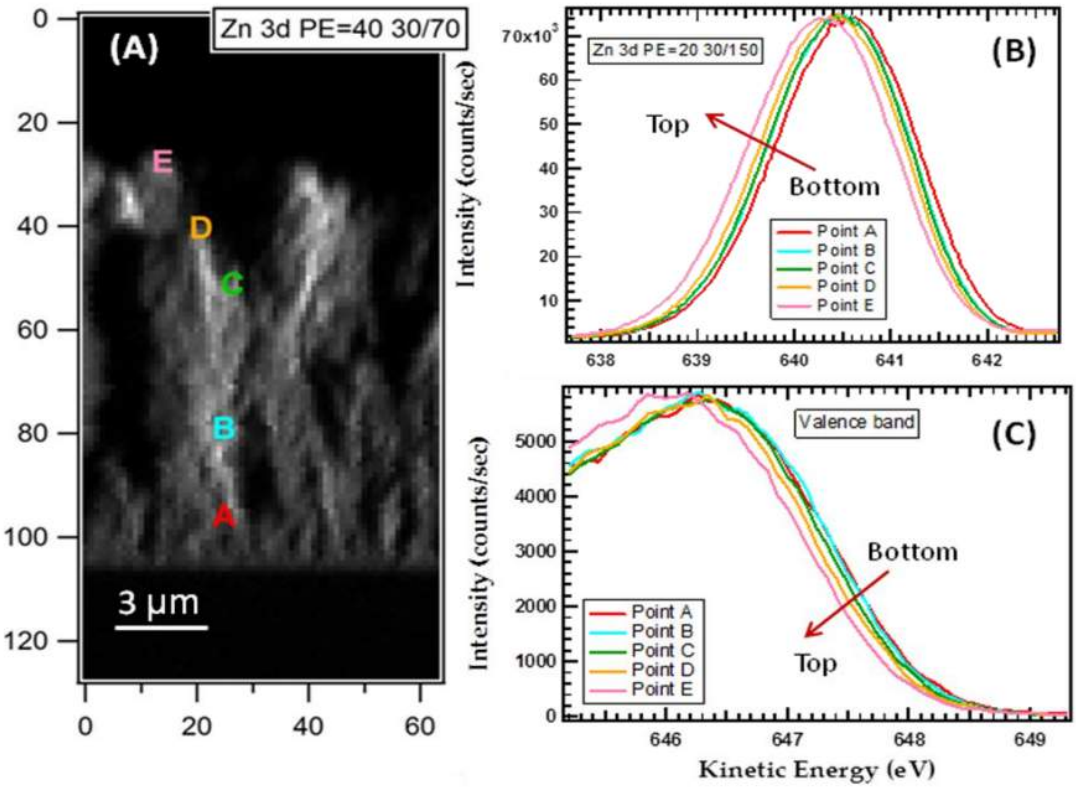

Figure 5.10: *(a) SPEM map (11x23 µm^2) of the cross section of an AZO nano-forest grown at 110 Pa O_2, acquired from the Zn 3d core level. The letters A-E indicate the acquistion points of XPS spectra along a possible electron conduction path. (b) Single point XPS spectra of the Zn 3d core levels taken at the A-E points indicated on the map. (c) Single point XPS spectra of the valence band in the same points.*

Zn 3d, O 1s, Al 2p levels as well as the valence band were acquired to monitor the charging-induced shift. Results of these measurements can be seen in figure 5.10.b-c, where the evolution of the Zn 3d and valence band peaks upon moving from A to E is reported. A rigid shift (up to 250 meV) towards smaller kinetic energies is observed along the growth direction, without significant alterations of the peak shape. This is compatible with the assumptions leading to the formulation of equation 5.2 [162], indicating that the shift is possibly induced by the ineffective screening of photoemitted charges, and it is therefore depending on the conductivity of the nanotrees. Equation 5.2 can be then used to estimate the order of magnitude of σ, obtaining $\sigma \approx$µS/cm, corresponding to cross plane resistance values of the order of $10^{10}\Omega$.

The same measurement, performed on hierarchical AZO layers grown with a smaller (6%) oxygen partial pressure, revealed a negligible shift, indicating a cross-plane resistance below the sensitivity limit of this approach. Instrumental considerations regarding the parameter C of equation 5.2 allow to estimate that this limit is around 1GΩ, suggesting that the resistance of the sample is significantly lower than this value. Both the obtained results are in agreement with the direct estimate of cross-plane electrical resistance, which indicated a resistance of about 10 GΩ at 100% O_2 and 10 KΩ at 6% O_2 as discussed above.

6

Multifunctional graded layers

This chapter presents another approach for the development of transparent conducting AZO layers with effective light management properties. The basic idea behind this approach is to obtain complex AZO architectures constituted by a large surface area porous scattering layer and a compact TCO. The development of this approach - leading to the synthesis of functionally graded structures - and the subsequent optimization of multifunctional architectures are described in section 6.1. An in-depth analysis of the effects of surface morphology on electrical and optical properties of graded AZO layers is presented in section 6.2, followed by an example of application as a light harvesting enhancer in organic PV devices in section 6.3.

6.1 Development of functionally graded structures

The optimized electrical properties of compact AZO layers and the large surface area and optical properties of hierarchical mesoporous AZO layers, as described in chapter 4, are the result of a complex interplay between morphology, structural and local stoichiometry properties. In chapter 5, the possibility to achieve independent control of these properties by means of stoichiometry was discussed: another possible way to obtain a multifunctional material, described in the present chapter, is constituted by a spatial separation of functional properties. The basic idea for the development of this approach is depicted in figure 6.1: a

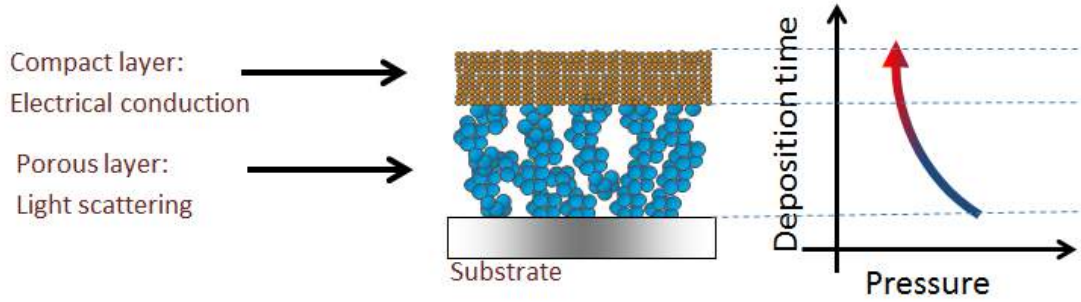

Figure 6.1: *Schematic of the development of functionally graded AZO layers. The bottom porous layer is grown at high deposition pressure, the top compact layer is grown at low deposition pressure.*

multifunctional structure can be obtained by growing a compact conducting AZO layer on top of a porous scattering layer. If both layers are transparent, the resulting structure is a scattering TCO film. The realization of this structure can be devised in a single PLD process, in which the (oxygen) deposition pressure is varied: as depicted in the graph of figure 6.1, if the first part of the deposition is performed at high pressure, the bottom layer of the film is constituted by a hierarchical mesoporous nano-forest. The pressure is then decreased down to values suitable for the growth of a compact AZO layer. However, due to the high kinetic energy of the ablated species in low pressure conditions, an abrupt decrease in the O_2 pressure leads to the damaging of the forest-like structures. As a consequence, the pressure decrease needs to be performed gradually, obtaining a buffer layer between the porous and compact parts of the film: this strategy allows the realization of *graded* AZO structures, rather than plain multi-layers. The optimization of the growth conditions of this buffer layer constituted a first, critical step: an average pressure decrease rate of ≈ 6 Pa/min was identified as an

effective compromise to preserve the forest-like morphology without excessively increasing film thickness. The opposite approach, i.e. the realization of a porous film on top of a compact film, does not require this kind of procedure: however, its degree of interest is lower for two reasons. First, the electrical characterization of such structure is rather complex due to the difficulty of applying contacts on the top where the porous layers are present. Second, this architecture is less applicable to a HOPV device, where the TCO is placed on a glass substrate and below the active layer: the interface between a forest-like layer and the active medium is inevitably more complex to deal with than the same interface with a compact layer.

Taking advantage of the results discussed in chapter 4, the background pressure for the deposition of the bottom porous layer was chosen in the 100-200 Pa range in order to obtain scattering hierarchical structures and the pressure for the top compact layer was fixed at 2 Pa O_2, where electrical properties showed their optimal values. The parameters explored in order to obtain the desired combination of properties were the background gas pressure for the deposition of the porous layer and the equivalent thickness (i.e. deposition time) of the porous and compact layers.

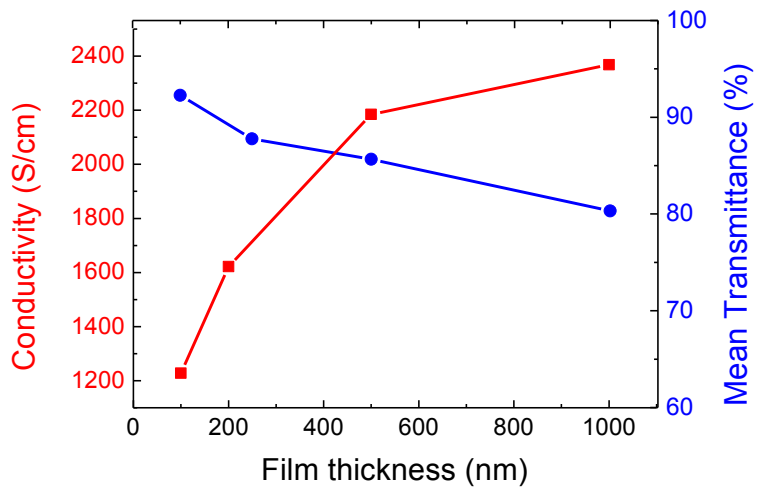

Figure 6.2: *Electrical conductivity and average optical transmittance from AZO layers grown at 2 Pa O_2, as a function ot film thickness.*

The thickness of the compact layer was chosen in order to have a suitable combination of electrical conductivity and optical transparency, whose variations

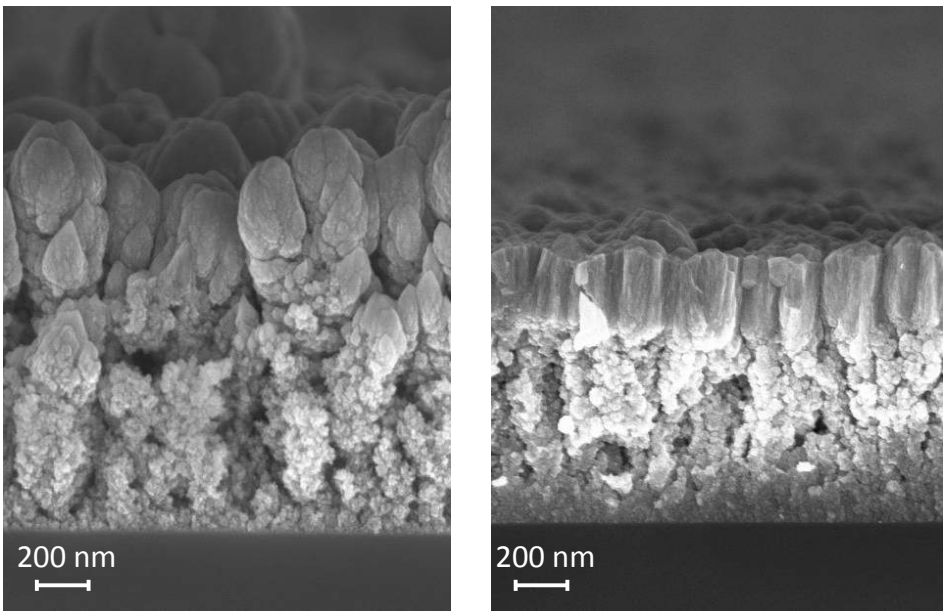

Figure 6.3: *Cross-sectional SEM images of graded AZO films with porous layers grown at 160 Pa O_2 (left) and 100 Pa O_2 (right) [163]*

with film thickness (at a fixed deposition pressure of 2 Pa O_2) can be seen in figure 6.2. In the 250-300 nm range, very high transmittance values are accompanied by high conductivity: this range was chosen in order to keep the transmittance as high as possible in view of the development of an overall thick graded structure.

To understand the effects of the bottom layer deposition pressure on the morphology of the graded structure, figure 6.3 shows cross-sectional SEM images of functionally graded AZO films grown in different conditions. The left part of the figure shows a film whose scattering layer was grown at 160 Pa O_2 with a thickness of 800 nm: the morphology of this layer is (as expected from previously discussed results) characterized by hierarchical forest-like structures, with a significant fraction of voids, corresponding to a partial spatial separation of the hierarchical structures; as a consequence, the compact layer provides a nonuniform coating which traces out the underlying porous layer surface. In the right part of fig. 6.3, a film whose bottom layer was grown at 100 Pa O_2 is presented; the morphology is significantly less porous and more uniformly connected. The less open morphology results in a more uniform surface, on which the growth of the compact layer occurs in a more uniform manner; the top part of the film is constituted by a flatter, uniform coating.

O_2 pressure (Pa)	160/2	100/2
Equivalent thickness (nm)	800+300	750+250
Mean total transmittance	64.7%	90.2%
Mean haze	73.1%	11.6%
Sheet resistance ($\Omega/\square$)	15.1 k	93.1
Sheet carrier density ($\cdot 10^{15}\,\mathrm{cm}^{-2}$)	1.68	8.2
Hall mobility ($\mathrm{cm}^2/\mathrm{Vs}$)	0.25	8.19

Table 6.1: *Overview of properties of the films shown in figure 6.3. Mean transmittance and haze have been calculated in the visible (400 nm - 700 nm) range.*

An overview of functional properties of the films is reported in Table 6.1, which can be used to highlight the main effects of deposition time and pressure.
First, a higher oxygen pressure during the growth of the bottom layer increases its porosity and hence haze; as discussed in the previous chapters, the interaction of the incoming light with the hierarchical structures is maximized when the characteristic dimensions of the nano-trees are comparable with the incoming wavelength. An increase in the deposition time of the bottom layer sorts the same effect, since porosity increases along the direction normal to the substrate. On the other hand, a higher effective thickness implies lower total transmittance (in ordered media the decrease would be exponential according to Lambert-Beer's law, in highly scattering systems such as these the optical path is expected to be even longer, with even lower total transmittance). Furthermore, an increase of deposition time or pressure results in higher surface roughness, and hence in a less regular coverage by the compact layer. This has dramatic effects on electrical properties: the sheet resistance of the 160 Pa sample is over 150 times higher than the 100 Pa sample, as reported in table 6.1. The main reason to this discrepancy is found in the significant decrease in mobility (by a factor 30) due to the lack of a continuous path for charge carriers as a consequence of morphology. It should be pointed out that these mobility values were obtained by approximating the compact film to a uniform coating in order to ensure validity of the Van der Pauw hypotheses, and are hence to be considered as effective Hall mobility values. Increasing the thickness of the compact layer can significantly increase carrier mobility, but it is detrimental for optical transparency: 200 nm of compact AZO (2 Pa) are characterized by the same mean visible transmittance ($\approx$ 90%) (see figure 6.2) as 1 µm of porous AZO (100 Pa), as discussed in chapter 4.
An optimal combination of deposition conditions was identified by increasing the

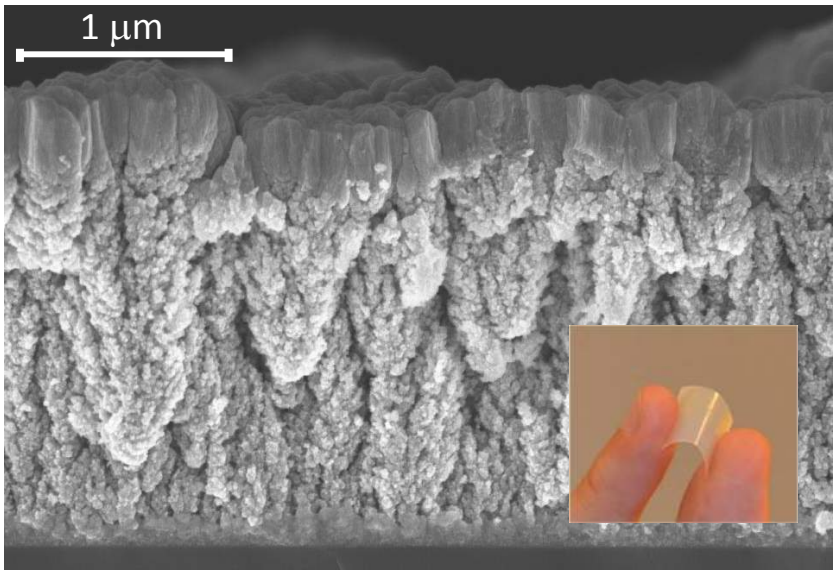

Figure 6.4: *Cross-sectional SEM image of a sample grown with a thicker bottom layer grown at 100 Pa. The inset on the right shows a photograph of the corresponding sample deposited on a flexible ETFE substrate [163].*

O_2 pressure (Pa)	100/2
Equivalent thickness (nm)	1600+250
Mean total transmittance	77.07%
Mean haze	42.39%
Sheet resistance ($\Omega/\square$)	162
Sheet carrier density ($\cdot 10^{15}\,\mathrm{cm}^{-2}$)	15.2
Hall mobility ($\mathrm{cm}^2/\mathrm{Vs}$)	2.52

Table 6.2: *Overview of properties of the film shown in figure 6.4. Mean transmittance and haze have been calculated in the visible (400 nm - 700 nm) range.*

equivalent thickness of a 100 Pa bottom layer to about 1.6 µm, maintaining 250 nm of compact layer on the top. A cross-sectional SEM image of a film grown in these conditions is presented in figure 6.4, and a summary of its functional properties is listed in table 6.2. The increase in thickness is sufficient to obtain a haze over 40% without compromising total transmittance, which is close to 80%. We point out that total transmittance can be controlled by choosing the combination of equivalent thicknesses of the two layers. Transmittance and haze spectra are presented in figure 6.5.a, where total transmittance (dotted line) shows a flat profile in the red-nIR ($\approx$ 80%) and decreases in the blue-UV due to interband electronic transitions, but also in the IR due to free carrier absorption in the conduction band. Light scattering (diffuse transmittance, dashed line) is

maximum in the visible (≈ 35%) giving rise to a haze (dotted line) of the order of 40%.

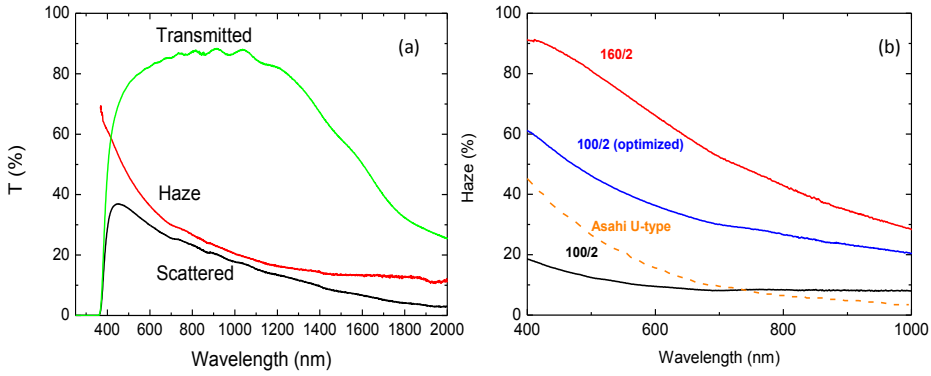

Figure 6.5: *(a) Optical transmittance spectra of the optimized graded architecture shown in fig. 6.3. Total transmittance (green), diffuse transmittance (red) and haze (black) are reported in the 250 nm - 2000 nm wavelength range. (b) Haze spectra of the investigated graded AZO layers, shown with a reference 980 nm FTO Asahi U-type glass [163].*

The sheet resistance of this film is around 160 Ω/□, with a carrier mobility of around 2.5 cm^2/Vs. This is a confirmation of the fact that electrical transport occurs in the compact layer alone: a compact AZO film of the same thickness (200 nm) grown at 2 Pa on a smooth substrate has a sheet resistance which is lower by a factor 5 ($R_S \approx 30\Omega/\square$), with a carrier mobility of about 13 cm^2/Vs (5 times higher than the graded film as well).

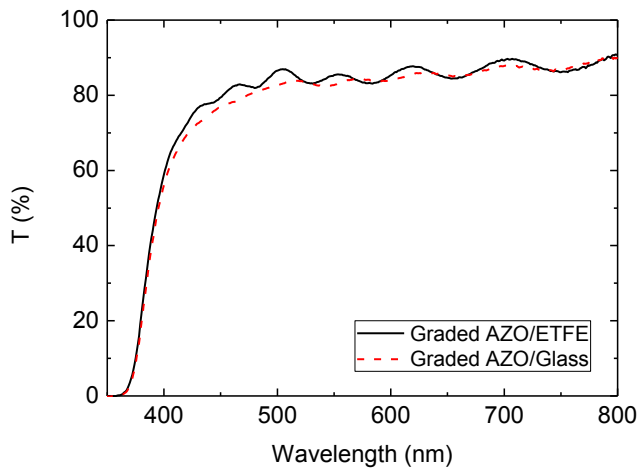

Figure 6.6: *Optical transmittance spectra of identical functionally graded AZO films deposited on glass (red dashed line) and on ETFE (black solid line).*

The properties of the films grown on flexible ETFE substrates were also measured: no significant difference was found in optical properties (both transmittance and haze varied by less than 4% with respect to glass substrates, as shown in figure 6.6) whereas the sheet resistance was uniformly increased by a factor 2.5, reaching an optimal value of 400 $\Omega/\square$ in the optimized films. This increase in resistivity is reasonably due to a decrease in connectivity, as confirmed by SEM analysis. It is worthwhile to point out that this value does not significantly increase upon bending, probably because of a damping of strain due to the porous structure and buffer layer below the compact film. A photograph of a graded film grown on ETFE is reported in the inset in fig. 6.4.

6.2 Surface morphology and functional properties

The connection between morphology and carrier mobility was investigated in detail by synthesizing graded AZO layers similar to the optimized structure reported in figure 6.4, with controlled surface roughness, to determine whether it is possible to state that the morphology of the porous layer drives carrier mobility in the compact layer.

In order to do so, small variations of the bottom layer deposition pressure and time were performed: the deposition of the compact layer is strongly influenced by the underlying porous structure, therefore the morphology of the top layer is directly connected with the properties of the bottom layer. Cross-sectional SEM images of functionally graded AZO layers with increasing porosity (i.e., deposition pressure or time) of the bottom layer are reported in figure 6.7. The details (deposition pressure and time for the compact and porous layers) and the average thickness (taken from multiple SEM measurements) are also reported in the figure. The effects of deposition time and pressure are visible both in terms of thickness (increasing both with pressure and time) and of surface morphology: in figure 6.7.a the compact layer is smoother and more uniformly connected, and as pressure and time are increased (b-c) the top layer evolves towards a more wavy and corrugated surface. This is in agreement with the AFM images presented in fig. 6.7.d-f, from which surface roughness values were calculated. Both Roughness average (Ra, mean value of the absolute displacement from average height data of on 10x10, 20x20 and 50x50 μm^2 AFM images) and root mean square (Rms, their standard deviation) are shown. Ra values increase from about 40 nm to about 60 nm as a result of the devised deposition conditions, and Rms values accordingly increase from 50 nm to 80 nm. Surface grain area was also calculated: results indicate that the area of the surface domains, increasing from 0.1 μm^2 to 0.4 μm^2 with increasing surface roughness, traces the characteristic size of the underlying nanotree forest. The difference in surface grain size is clearly visible from AFM images. For comparison, SEM images of the same samples at the same scale are shown in the figure insets. Roughness values on glass and silicon substrates were comparable (i.e. within the standard deviation of the data). The average roughness Ra value has been used as an indicator to perform a quantitative analysis of optical and electrical properties, and its variations can be controlled through the morphology of the bottom porous layer alone, since the surface properties of the compact layer are strongly influenced by the underlying

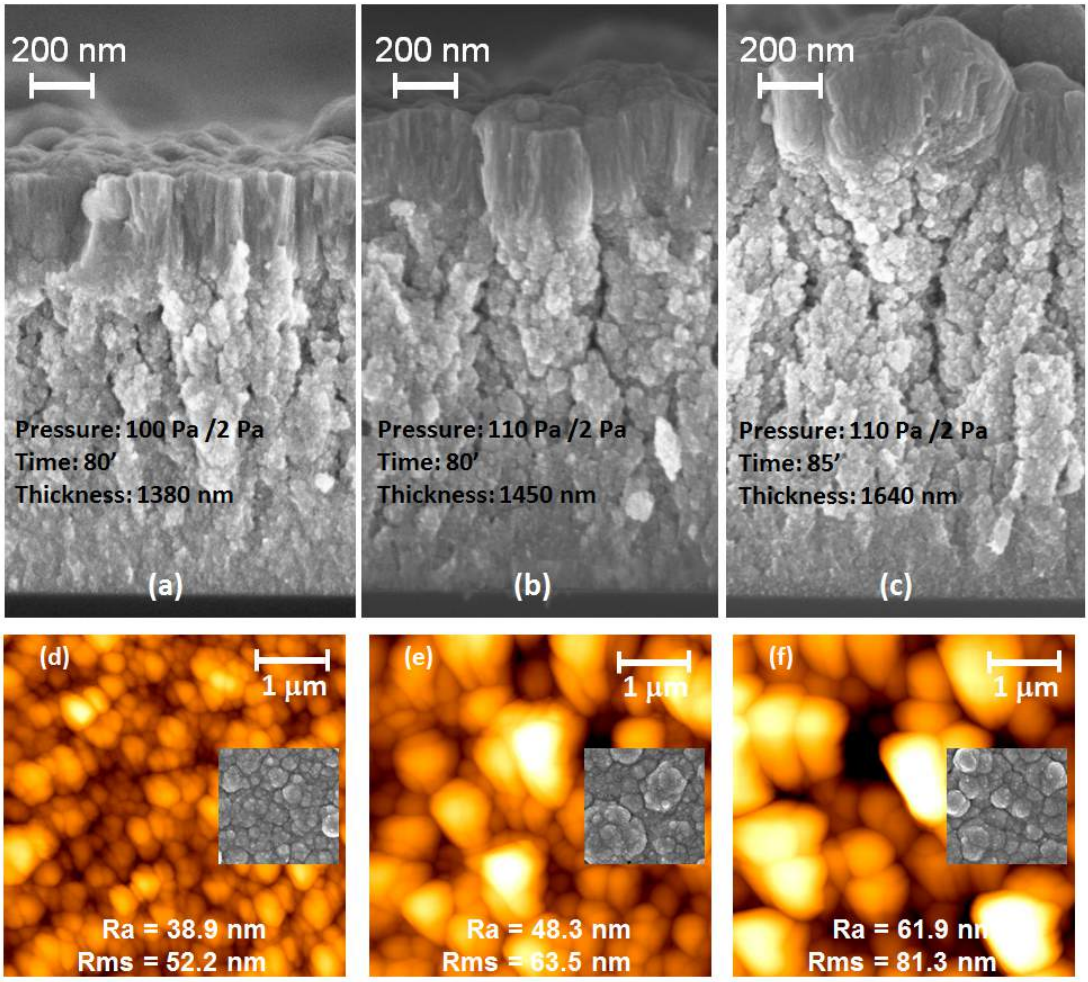

Figure 6.7: *(a-c) Cross sectional SEM images of samples with different surface morphology. The deposition pressures and times are also presented, along with the average thickness values. (d-f) 5 µm × 5 µm tapping mode AFM images of graded AZO layers, for the same samples, with the measured Roughness average (Ra) and Root mean square (Rms). The insets show top SEM views of the same samples at the same scale, for comparison [164].*

material, provided that the transition between the two layers occurs in a smooth and gradual way.

Figure 6.8 shows the effects of surface roughness on electrical and optical properties. The values of resistivity here presented were calculated from sheet

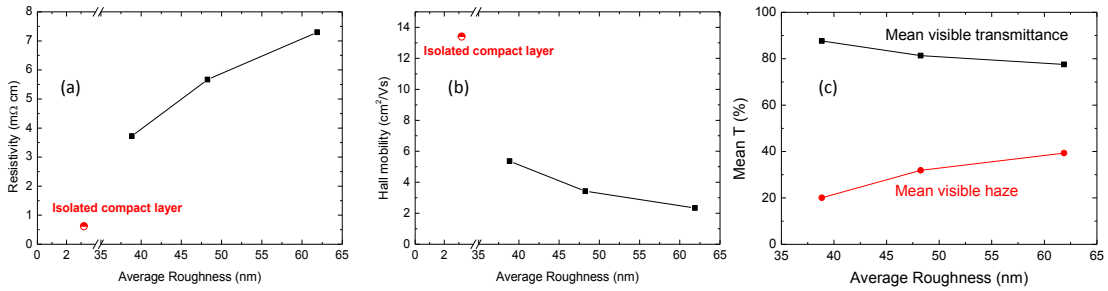

Figure 6.8: *Electrical resistivity (a) and carrier mobility (b) as a function of average surface roughness. Resistivity is of the order of $10^{-3}\Omega$ cm and increases with surface roughness, carrier mobility is of the order of few cm^2/Vs and decreases accordingly. Resistivity and mobility values of an isolated compact layer (half-filled red dots) are reported in correspondence of its roughness for comparison. (c) Optical transmittance (black squares) and haze (red dots) averaged in the 400 nm-700 nm wavelength range, as a function of average surface roughness [164].*

resistance using an equivalent thickness of 300 nm for the compact layer, under the hypothesis that electrical conduction occurs in the compact layer only. Electrical resistivity, of the order of 10^{-3} Ω cm, increases by a factor 2 with the examined increase of surface roughness, and carrier mobility values decrease accordingly by the same amount. The concentration of charge carriers exhibits small variations (from 3.15 to 3.6 $\cdot 10^{20}$ cm^{-3}), indicating a significant correlation between morphology and electrical properties, mainly affecting mobility. As widely discussed in the previous chapters, carrier concentration in doped ZnO is influenced by intentional and unintentional dopants, and therefore variations in morphology should leave it virtually unaffected. The in-plane effective carrier mobility, on the other hand, is affected by grain boundaries (possibly smaller crystal grain size) and lack of uniform connectivity, which can increase significantly as the compact layer changes from a uniform, flat film to a wavy corrugated surface (see figure 6.7). The trend in mobility as a function of surface roughness allows to state that carrier mobility in graded AZO is morphology-limited, and morphology can almost fully account for the measured increase in electrical resistivity. Optical transmittance (fig. 6.8.c) exhibits a small decrease with increasing surface roughness, showing mean values decreasing from almost 90% to almost 80% in the visible range. This variation can be mainly ascribed to an

increase in thickness, as can be seen from the SEM images of figure 6.7: if the absorption coefficient is considered rather than the transmittance, values do not vary significantly and are of the order of 1400 cm^{-1}. The variations in haze are more significant, indicating that morphology affects light scattering more heavily than optical transmittance: the mean value of haze in the visible range is doubled from 20% to 40% with the variations of morphology described above in terms of porosity, thickness and surface roughness. Besides the increase in porosity, part of this increase may be also due to light deflection at the film/air interface as a consequence of surface roughness.

To summarize, this functionally graded AZO architecture allows to obtain transparent scattering electrodes, whose properties can be fine-tuned by small morphology variations, and whose whole synthesis process is performed in one step at room temperature, without any kind of post-treatment and hence providing full compatibility with flexible substrates.

6.3 Light harvesting properties

In the framework of advanced solutions for solar cells, semiconducting polymers offer excellent light harvesting capabilities and good charge carrier mobility in the same material. However, in contrast to inorganic absorbers, the energy bands are relatively narrow, and low band gap polymers tend to incompletely absorb light in the visible region of the spectrum. Also, in contrast to inorganic absorbers, a heterojunction is required between the light absorbing polymer and an electron acceptor in order to ionize the photoinduced excitons. For all organic solar cells, 'panchromaticity' is achieved by employing an electron acceptor which also absorbs visible light. However, the choice of effective visible absorbing electron acceptors is currently limited to one, namely (6,6)-phenyl-C70-butyric acid methyl ester (C70-PCBM), or derivatives thereof, which is both challenging to isolate and purify and also limited in its own spectral width. The beneficial effects of the scattering layer on the material performance in photovoltaic devices have been tested by evaluating the increase in absoprtion of PCPDTBT[1], a low bandgap polymer [165] employed in state-of-the-art organic photovoltaics as an electron donor [166]. As anticipated in section 1.3, theoretical studies [128] predict maximum device efficiency if the active medium thickness is below 100 nm. For these reasons, in order to investigate the benefits deriving from light scattering, a 40 nm thick layer of PCPDTBT was spin-coated on an optimized 100/2 Pa graded AZO film and on a 200 nm thick compact AZO layer for comparison. An example of cross-sectional SEM image of the obtained structure is presented in fig. 6.9.a, where it is possible to notice how the polymer adheres to the compact layer without infiltrating into the porous part. Optical absorption properties were measured in the two systems, and the substrate and AZO contributions were subtracted to analyze the effects of haze. The spectra are reported in figure 6.9. The optical density of the polymer deposited on the graded system is significantly increased (up to 100%) in the 400 nm - 600 nm region with respect to the compact one. This corresponds to an increase in light harvesting efficiency from 36% to 60% in the short wavelength absorption peak[2]. In this wavelength range the polymer absorption is lower than in the red-NIR regions, and the haze of the graded structure is maximum (see figure 6.5). It is thus possible to state that the increase in optical density is due to an increase in optical path due to the improved light scattering of the graded structure. This benefit can be expected

[1] Poly[2,1,3-benzothiadiazole-4,7-diyl[4,4-bis(2-ethylhexyl)-4H-cyclopenta[2,1-b:3,4-b']dithiophene-2,6-diyl]]

[2] Light harvesting efficiency is defined as 1-10^{-OD}, where OD is the optical density.

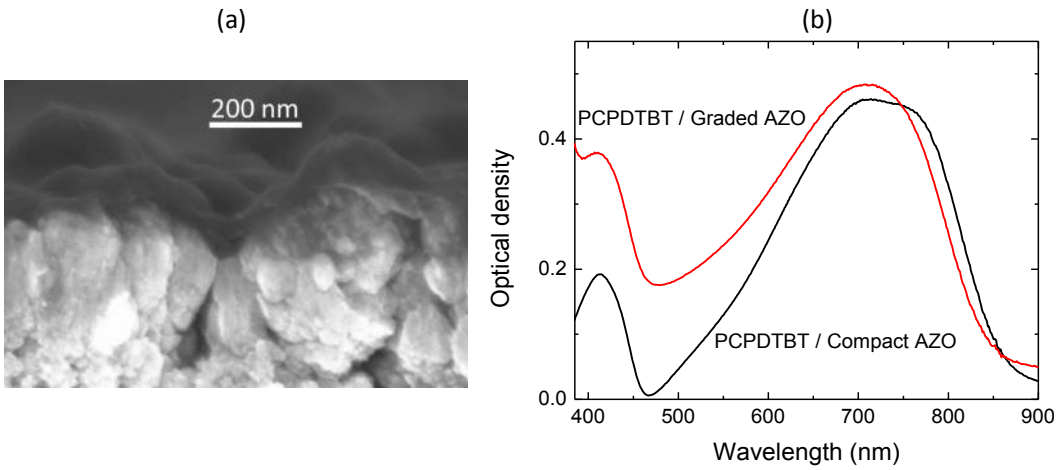

Figure 6.9: *(a) SEM image of a 40 nm PCPDTBT layer spin-coated on a graded AZO film. No infiltration of the polymer into the porous layer is observed. (b) Optical density of a PCPDTBT layer on a compact AZO film (black, solid) and on a 100/2 graded AZO film (red, dashed). The absorption of substrate and AZO was subtracted from the curves [163].*

to increase further if the incidence angle is varied from the normal direction.
It is also possible to point out that, as discussed in section 4.1, the spectral behaviour of haze can be modified by varying the pressure and gas flow rate during the synthesis of hierarchical AZO layers: the approach presented in the present chapter can be considered as a proof of concept which can be adapted to maximize light harvesting in other spectral regions, if other absorbing materials are considered.

7 Conclusions and perspectives

The requirements for transparent electrodes in new-generation PV devices have gone beyond the conventional combination of electrical conductivity and optical transparency typical of flat Transparent Conducting Oxide (TCO) layers. Large surface area, effective light management (scattering and trapping), preferential charge transport direction, mechanical flexibility and room temperature synthesis are among the most important properties suitable for applications of novel transparent electrodes and photoanodes. These requirements have been addressed in the present work, leading to the development of nanostructured Al-doped ZnO (AZO) layers synthesized at room temperature by Pulsed Laser Deposition (PLD). The structure/property relation was first investigated by obtaining different structures and morphologies, identifying the effects of the deposition parameters (e.g. O_2 background pressure during deposition) which can be varied to achieve control of structural and functional properties.

State-of-the-art compact AZO layers, with electrical resistivity of the order of $4.5 \cdot 10^{-4} \Omega\,\mathrm{cm}$ (sheet resistance 9 $\Omega/\square$) and mean visible transmittance of 85% were obtained at an optimal O_2 deposition pressure of 2 Pa, where a compromise between electron donor-type defects and local structural order permits the filling of the conduction band without excessively decreasing carrier mobility and optical transparency. At higher deposition pressures (> 100 Pa), the morphology evolves towards a hierarchical assembly of nanoparticles which resembles a forest of nanotrees with mesoscale porosity: this morphology is optimal for light scattering (haze $> 80\%$) and optical transmittance ($> 85\%$) but the lack of continuous conduction paths is detrimental for electrical resistivity, which reaches values of the order of $10^6\ \Omega\,\mathrm{cm}$. All the depositions were performed also on flexible ETFE layers,

obtaining full compatibility with polymer substrates of interes for organic PV.

The understanding of the structure/property relation, supported by investigations on the effects of thermal treatments in different atmospheres and comparisons with undoped ZnO, allowed to devise two approaches to obtain separate control of electrical and optical properties in order to combine them into multifunctional AZO layers. The first approach aims at an independent control of morphology and defect concentration (i.e. ZnO stoichiometry) by performing PLD in mixed Ar:O_2 atmospheres. If the total deposition pressure is maintained at high ($>$ 100 Pa) values, forest-like morphologies optimized for light management can be obtained. The O_2 partial pressure can be varied to obtain control of stoichiometry, which directly influences electrical properties. In fact, electrical resistivity, optical transmittance and haze all increase with O_2 partial pressure. With this approach, at O_2:Ar partial pressure ratios in the 2%-6% range, it was possible to decrease the resistivity of mesoporous AZO nano-forests by up to 5-6 orders of magnitude, maintaining optical transparency and haze at high values, which can be further adjusted by varying film thickness. The electrical properties of electrically conducting nano-forests were also investigated in terms of cross-plane electrical transport, finding a similar dependence on oxygen partial pressure.

The second approach consists in the synthesis of functionally graded AZO layers, constituted by a mesoporous forest-like structure which evolves into a compact transparent conducting layer. This architecture can be synthesized in a single PLD process, by decreasing the O_2 pressure during deposition. In the obtained graded AZO structures, the bottom porous layer acts as a (transparent) light scatterer, and the top compact layer as a (transparent) electrical conductor. Analyzing the influence of the morphology of the porous layer on the electrical properties of the compact layer allowed us to find an optimal graded architecture, with resistivity of the order of $10^{-3}\ \Omega\,\mathrm{cm}$, optical transparency of about 80% and haze of about 40%. This optimal structure (deposited also on ETFE, where it exhibited mechanical stability upon bending) was tested by evaluating the benefits of haze on the absorption profile of a low bandgap polymer employed in organic PV solar cells as an electron donor (PCPDTBT). The test demonstrated a significant increase (up to 100%) in the spectral region where the polymer absorption is lower and AZO haze is maximum.

Among the possible future perspectives deriving from this work, it is possible to cite a deeper study of local chemistry taking advantage of preliminary results from Scanning Photo Electron Microscopy, which pointed at a somewhat surprising

distribution of the Al dopant atoms in the film cross section, with a tendency to segregate to the top part of the nano-forest regardless of deposition conditions and without any thermal treatments.

Another development, as a natural consequence of the test performed on graded AZO with PCPDTBT, is the fabrication and test of a full PV device, to evaluate the benefits deriving from the obtained increase in PCPDTBT absorption on short circuit current density and device efficiency. Preliminary tests of compatibility in novel perovskite-based solar cells are also under way, with the aim to take advantage of the morphology of mesoporous AZO layers.

Since the most recent developments of research on transparent electrodes involve networks of quasi-1d structures, it would be interesting to investigate the possibility to cover low-cost nonconducting networks (e.g., polymer nanowires) with a thin AZO layer to make them free-standing transparent conducting nanowire networks. Preliminary tests of compatibility have already been performed in this direction.

Finally, the discovery of a complex interplay between defects and functional properties suggests that further work may be dedicated to understanding defect chemistry/physics by deeper investigations of Raman spectroscopy, photoluminescence measurements and X-ray photoemission spectroscopy.

Acknowledgements

ARRIVATI a questo punto, sarebbe il momento di ringraziare tutte le persone che mi hanno aiutato, sostenuto, supportato e sopportato in questi tre anni. Ma questa volta vorrei evitare di fare un elenco di nomi e motivazioni, sprofondando nella mia solita incontrollabile emotività.
Perché, da un certo punto di vista, tutto si riduce a riconoscere qualcosa di molto semplice e al tempo stesso piuttosto profondo: sono una persona fortunata. Forse una delle persone più sfacciatamente fortunate della storia. E la mia fortuna si riassume nell'avere avuto in sorte una famiglia che mi ha insegnato quali sono le cose più importanti *che ci fanno vivere*, degli amici che hanno condiviso con me l'inverosimile (e forse anche di più), dei colleghi che mi hanno saputo capire (e so che non è sempre stato facile), dei relatori che - più che da professori - mi hanno seguito con un cuore competente da fratelli maggiori, e una persona che in soli tre anni ha trasformato la mia vita in un nuovo, meraviglioso percorso insieme.
E capite che, con questa consapevolezza, guardare al passato è dolcemente rassicurante, e pensare al futuro porta un'impazienza altrettanto dolce.
Grazie, quindi, senza troppe altre parole. Ho amato questi tre anni di vita, e di sicuro è stato anche merito vostro.

Milano, luglio 2014 P. G.

A

Experimental details

THIS Appendix lists the technical details and specifications of the experimental instrumentation employed during this work. The relevant physical processes involved in the synthesis and measurement processes are described in chapter 3. For practical instructions concerning the deposition procedures for AZO layers with the apparatus employed in the present work, the reader is referred to ref. [143].

A.1 Pulsed Laser Deposition apparatus

The PLD system employed for the synthesis of AZO layers is shown in figure A.1 and it is constituted by a Continuum-Quantronix Powerlite 8010 pulsed Q-switched Nd:YAG laser, with two frequency multipliers to obtain the 4th harmonic wavelength of 266 nm. The pulse duration was $\approx$ 6 ns, the energy per pulse 75 mJ, the repetition rate 10 Hz. The laser spot size on the target was varied with a plano-convex lens with focal length=50 mm. The target was a solid sintered 2%wt. Al_2O_3 blend (Lesker). The substrates (soda-lime glass, (100) Si, Ti, ETFE) were mounted on a rotating substrate holder which was placed off-axis and rotated during deposition in order to increase the deposited area. The deposition chamber was evacuated to $< 10^{-3}$ Pa prior to each deposition with pumping system constituted by a Varian dryscroll pump and a Turbomolecular pump. The gas flow was supplied by mks 2179a digital system, with 100 sccm and 1000 sccm mass flow controllers. Deposition rates were measured with an Infcon XTC/2 Quartz Crystal Microbalance, and pre-deposition cleaning was performed with a Mantis Dep RFMAx60 Ion Gun (Ar plasma accelerated at 500 V, radiofrequency

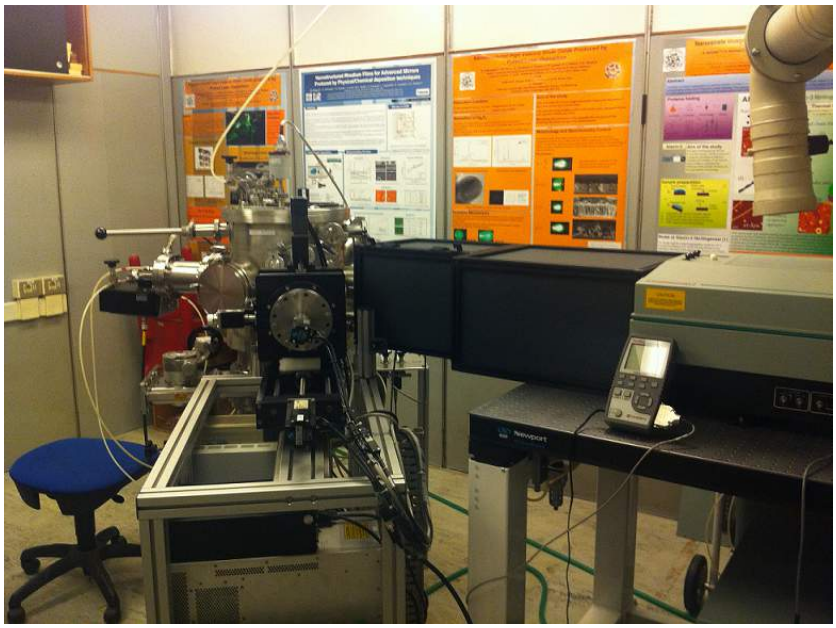

Figure A.1: *Pulsed Laser Deposition apparatus*

power 200 W).

A.2 Structural and functional characterization

Scanning Electron Microscopy was performed with a Zeiss SUPRA40 Field Emission SEM, equipped with Oxford Energy Dispersive X-ray Spectroscopy. Atomic Force Microscopy images were acquired with a Thermomicroscopes Autoprobe CP II using Veeco RTESPA tips (spring constant 20-80 N/m, resonance frequency 200-300 kHz). X-Ray Diffraction was performed in $\theta - 2\theta$ configuration with a Bruker D8 Advance Diffractometer (Cu $K_{\alpha 1}$, $\lambda = 1.5406$ Å).

In-plane electrical properties were measured in the 2-point (for resistivities of 100 Ω cm and higher) and 4-point probe (for resistivities up to 100 Ω cm) configurations with a Keithley K2400 Source/Measure Unit as a current generator (from 100 nA to 10 mA), an Agilent 34970A voltage meter (6 $\frac{1}{2}$ digits, sensitivity 1 nV) and a 0.57 T Ecopia permanent magnet. A homemade analog commutator was used to exchange the current carrying and voltage measuring electrodes, which were constituted spring loaded Au pogo pins mounted on an Ecopia PCB board. In the case of thick porous films (2 μm), due to difficulties in applying contacts onto the porous surface, the current was injected from the bottom (i.e. at the substrate/film interface) through evaporated Au contacts.

Cross-plane electrical measurements were performed inside a Dual Beam (FIB-

SEM) system using a two-probe setup: one electrode was fixed on the ITO substrate by silver paste, the second electrode was a tungsten tip mounted on a piezo nanomanipulator that could be moved around on the AZO film. The electrodes were connected to a Keithley sourcemeter supplying the bias voltage and measuring the current down to a sensitivity of 0.01 pA. On each sample, as a first check, an I-V curve was measured on the ITO substrate. Because of the porosity of the sample, the approach of the tip onto the AZO film was a critical step, therefore it was controlled under live SEM imaging in order to obtain similar conditions for each measurement. After lifting up the probe, an SEM image was taken to measure the tip contact area.

Relative variations in stoichiometry were estimated with spatially resolved X-ray photoemission spectroscopy performed at the ESCA microscopy beamline of the Elettra Synchrotron facility in Trieste, Italy. Synchrotron source X-ray beam is focused on the sample to a diameter of about 130 nm using Fresnel zone plate optics, and the sample can be raster scanned with respect to the microprobe. Photoemission spectra were measured with a 650 eV photon energy with 0.2 eV energy resolution.

Optical characterization was performed with a UV-vis-NIR PerkinElmer Lambda 1050 spectrophotometer in the range 250 nm $\div$ 2000nm, with a 150 mm diameter Spectralon-coated integrating sphere (reflectance $> 95\%$ in the 250-2000 nm range, $> 99\%$ in the 400-1500 nm range). The detector was a R6872 photomultiplier in the UV-vis and an InGaAs photodetector in the NIR. For reflectance measurements, the specimen was mounted with a 8° inclination to let specular reflected light be detected. For transmittance measurements, the incident beam was made to hit the sample on the glass or ETFE side, to allow for an easier correction of the substrate contribution. Tauc plots and related fits were realized with the MATLAB software.

B

Envelope analysis

The envelope analysis method [31] employs the following analytical expression for the optical transmittance of a thin film in a low absorption region:

$$\frac{16n_s^2n^2x}{(1+n)^2(n+n_s)^2-2x\cos(\gamma)\left[(n^2-1)(n^2-n_s^2)\right]+x^2(n-1)^2(n-n_s)^2x^2} \tag{B.1}$$

where n_s and n are the substrate and film refractive indices, x is the absorption factor:

$$x = e^{-\frac{4\pi k}{\lambda}d} \tag{B.2}$$

and the oscillating term depends on both film thickness and refractive index:

$$\gamma = \frac{4\pi nd}{\lambda} \tag{B.3}$$

The following hypotheses must hold for the validity of eq. B.1:

- The film must be weakly absorbing in the examined spectral region.
- Film thickness must be uniform in the probed area (This was guaranteed by applying a 3 mm-diameter mask).
- Light absorption by the substrate must not be normalized.

The maxima and minima of T in eq. B.1 can then be obtain by letting $\cos(\gamma) = \pm 1$:

$$\begin{aligned} T_{max} &= \frac{16n_sn^2x}{\left[(1+n)(n+n_s)-(n-1)(n-n_s)x\right]^2} \\ T_{min} &= \frac{16n_sn^2x}{\left[(1+n)(n+n_s)+(n-1)(n-n_s)x\right]^2} \end{aligned} \tag{B.4}$$

These equations can be used to obtain, at a given wavelength corresponding to a stationary point, the values of k and n, if the interpolated T'_{max} and T'_{min} values

are calculated. T'_{max} and T'_{min} are, respectively, the values of the maxima envelope where T has a minimum and vice versa. If a dimensionless parameter N' is defined:

$$N' = \frac{1}{2}(1 + n_s^2) + 2n_s \frac{T'_{max} - T_{min}}{T'_{max} T_{min}} \tag{B.5}$$

eqs. B.4 can be rearranged to give

$$n = \sqrt{\left(N' + \sqrt{N'^2 - n_s^2}\right)} \tag{B.6}$$

and

$$x = \frac{(n+1)(n+n_s)}{(n-1)(n-n_s)} \frac{\sqrt{\frac{T'_{max}}{T_{min}}} - 1}{\sqrt{\frac{T'_{max}}{T_{min}}} + 1} \tag{B.7}$$

And analogously for any given pair of (T'_{min}, T_{max}). If we now call n_1 and n_2 the refractive indices calculated from B.6 at two wavelengths λ_1 e λ_2 where two adjacent maxima (or minima) are present, we obtain

$$d = \frac{\lambda_1 \lambda_2}{2(n_1 \lambda_2 - n_2 \lambda_1)} \tag{B.8}$$

These equations were combined in an iterative self-consistent MATLAB code, structured as follows:

- The experimental points of maxima and minima of the oscillations were acquired from transmittance spectra.
- T'_{max} and T'_{min} were calculated with a MATLAB interpolating algorithm.
- Eqs. B.5-B.7 were used to calculate n and x at every stationary point. I valori di n, x e T' appena calcolati costituiscono i dati iniziali del processo autoconsistente vero e proprio.
- At every iteration step, eq. B.8 is used (with d as a known parameter), to recalculate n_1^* e n_2^*[1]:

$$n_1^* = n_1 - a\left(-n_1 + n_2 \frac{\lambda_1}{\lambda_2} + \frac{\lambda_1}{2d}\right) \tag{B.9}$$

  and analogously for n_2^*. Inspection of eq. B.8 shows that the term in brackets in eq. B.9 must go to zero upon convergence. The parameter a $(0 < a < 1)$ was introduce to control the iteration steps and avoid divergence.

[1]The asterisk denotes the next iteration step

- With the calculated values of n_1^* e n_2^*, T' is recalculated, leading to new x and n values at both wavelengths, moving to the next iteration cycle.
- After 1000 cycles, if $|n - n^*| < 10^{-4}$, and the last calculated T' values are compatible with the experimental spectrum, the obtained values of n e k are accepted.

List of Figures

List of Tables

Bibliography

[1] Abdelilah Slaoui and Reuben T Collins. A dvanced Inorganic Photovoltaics. *MRS Bulletin*, 32:211–218, 2007.

[2] E Lorenzo. Energy collected and delivered by photovoltaic modules. In A. Luque and S. Hegedus, editors, *Handbook of Photovoltaic Science and Engineering*, Hoboken, NJ, USA, 2003. John Wiley & Sons, Ltd.

[3] Jenny Nelson. *The physics of solar cells.* Imperial College Press, London, UK, 2003.

[4] Neil W. Ashcroft and David N. Mermin. *Solid State Physics.* Thomson Learning, Toronto, Canada, January 1976.

[5] K. Bädeker. Über die elektrische leitfähigkeit und die thermoelektrische kraft einiger schwermetallverbindungen. *Annalen der Physik*, 327(4):749–766, 1907.

[6] David S Ginley and Clark Bright. Transparent Conducting Oxides. *MRS Bulletin*, 25:15–18, 2000.

[7] J C C Fan and J B Goodenough. X-ray photoemission spectroscopy studies of Sn-doped indium-oxide films. *Journal of Applied Physics*, 48(8):3524–3531, 1977.

[8] I Hamberg and CG Granqvist. Evaporated Sn doped In_2O_3 films: Basic optical properties and applications to energy efficient windows. *Journal of Applied physics*, 60:123–159, 1986.

[9] Elvira Fortunato, David Ginley, Hideo Hosono, and David C Paine. Transparent Conducting Oxides for Photovoltaics. *MRS Bulletin*, 32:242–247, 2007.

[10] Claes G Granqvist. Transparent conductors as solar energy materials : A panoramic review. *Solar Energy Materials and Solar Cells*, 91:1529–1598, 2007.

[11] Akshay Kumar and Chongwu Zhou. The race to replace tin-doped indium oxide: which material will win? *ACS nano*, 4(1):11–4, January 2010.

[12] Tadatsugu Minami. Transparent conducting oxide semiconductors for transparent electrodes. *Semiconductor Science and Technology*, 20:S35–S44, 2005.

[13] RG Gordon. Criteria for choosing transparent conductors. *Mrs Bulletin*, (25):52–57, 2000.

[14] Tadatsugu Minami. New n-Type Transparent Conducting Oxides. *MRS Bulletin*, 25:38–44, 2000.

[15] G Exarhos and X Zhou. Discovery-based design of transparent conducting oxide films. *Thin Solid Films*, 515(18):7025–7052, June 2007.

[16] Hiroshi Kawazoe and Hiroshi Yanagi. Transparent p-Type Conducting Oxides : Design and Fabrication of p-n Heterojunctions. *MRS Bulletin*, (25):28–36, 2000.

[17] Hideo Hosono. Recent progress in transparent oxide semiconductors: Materials and device application. *Thin Solid Films*, 515(15):6000–6014, May 2007.

[18] Hideo Hosono, Masahiro Yasukawa, and Hiroshi Kawazoe. Novel oxide amorphous semiconductors : transparent conducting amorphous oxides Possible Candidate for HMCs. *Journal of Non-Crystalline Solids*, 203:334–344, 1996.

[19] Johannes Krantz, Moses Richter, Stefanie Spallek, Erdmann Spiecker, and Christoph J. Brabec. Solution-Processed Metallic Nanowire Electrodes as Indium Tin Oxide Replacement for Thin-Film Solar Cells. *Advanced Functional Materials*, 21(24):4784–4787, December 2011.

[20] Jung-Yong Lee, Stephen T Connor, Yi Cui, and Peter Peumans. Solution-processed metal nanowire mesh transparent electrodes. *Nano letters*, 8(2):689–92, February 2008.

[21] F Wooten. *Optical properties in solids*. Academic Press, New York, NY, USA.

[22] Charles. Kittel. *Introduction to solid state physics*. Wiley, New York, NY, USA.

[23] Gordon Thomas. Invisible circuits. *Nature*, 389:907–8, June 1997.

[24] Elias Burstein. Anomalous Optical Absorption Limit in InSb. *Physical Review*, 93:632–633, 1954.

[25] B E Sernelius, K F Berggren, Z C Jin, I Hamberg, and C G Granqvist. Band-gap tailoring of ZnO by means of heavy Al doping. *Physical review B*, 1988.

[26] Anubha Jain, P Sagar, and R M Mehra. Band gap widening and narrowing in moderately and heavily doped n-ZnO films. *Solid-State Electronics*, 50:1420–1424, 2006.

[27] a. Abdolahzadeh Ziabari and S.M. Rozati. Carrier transport and bandgap shift in n-type degenerate ZnO thin films: The effect of band edge non-parabolicity. *Physica B: Condensed Matter*, 407(23):4512–4517, December 2012.

[28] Timothy J Coutts and David L Young. Characterization of Transparent Conducting Oxides. *MRS Bulletin*, 25:58–65, 2000.

[29] Kin Man Yu, Marie a. Mayer, Derrick T. Speaks, et al. Ideal transparent conductors for full spectrum photovoltaics. *Journal of Applied Physics*, 111(12):123505, 2012.

[30] A F Kohan, G Ceder, D Morgan, and Chris G Van De Walle. First-principles study of native point defects in ZnO. *Physical Review B*, 61(22):19–27, 2000.

[31] J C Manifacier, J Gasiot, and J P Fillard. simple method for the determination of the optical constants. *Journal of Physics E: Scientific Instruments*, 9:1002–1004, 1976.

[32] ON Mryasov and AJ Freeman. Electronic band structure of indium tin oxide and criteria for transparent conducting behavior. *Physical Review B*, 64(September 2000):2–4, 2001.

[33] Ç Kiliç and Alex Zunger. Origins of Coexistence of Conductivity and Transparency in SnO_2. *Phys. Rev. Lett.*, 88(9):95501, February 2002.

[34] J A Sans, A Segura, G Tobias, and E Canadell. Chemical effects on the optical band-gap of heavily doped ZnO : M III (M = Al , Ga , In): An investigation by means of photoelectron spectroscopy , optical measurements under pressure , and band structure calculations. *Physical Review B*, pages 1–9, 2009.

[35] Péter Ágoston and Karsten Albe. Intrinsic n-Type Behavior in Transparent Conducting Oxides: A Comparative Hybrid-Functional Study of In2O3, SnO2, and ZnO. *Physical Review Letters*, 103(24):245501, December 2009.

[36] Stephan Lany and Alex Zunger. Dopability, Intrinsic Conductivity, and Nonstoichiometry of Transparent Conducting Oxides. *Physical Review Letters*, 98(4):045501, January 2007.

[37] Anderson Janotti and Chris G. Van de Walle. Oxygen vacancies in ZnO. *Applied Physics Letters*, 87(12):122102, 2005.

[38] Wolfgang Körner and Christian Elsässer. First-principles density functional study of dopant elements at grain boundaries in ZnO. *Physical Review B*, 81(8):1–12, February 2010.

[39] Franz Urbach. The long-wavelength edge of photographic sensitivity and of the electronic absorption of solids. *Phys. Rev.*, 92:1324–1324, Dec 1953.

[40] R. C. Rai. Analysis of the Urbach tails in absorption spectra of undoped ZnO thin films. *Journal of Applied Physics*, 113(15):153508, 2013.

[41] S. Schönau, F. Ruske, S. Neubert, and B. Rech. Analysis of Urbach-like absorption tails in thermally treated ZnO:Al thin films. *Applied Physics Letters*, 103(19):192108, 2013.

[42] Andriy Zakutayev, Nicola H. Perry, Thomas O. Mason, David S. Ginley, and Stephan Lany. Non-equilibrium origin of high electrical conductivity in gallium zinc oxide thin films. *Applied Physics Letters*, 103(23):232106, 2013.

[43] Anderson Janotti and Chris G Van de Walle. Fundamentals of zinc oxide as a semiconductor. *Reports on Progress in Physics*, 72(12):126501, December 2009.

[44] S. Lany, A. Zakutayev, T. O. Mason, et al. Surface Origin of High Conductivities in Undoped In_2O_3 Thin Films. *Phys. Rev. Lett.*, 108:016802, Jan 2012.

[45] P P Edwards, A Porch, M O Jones, D V Morgan, and R M Perks. Basic materials physics of transparent conducting oxides. *Dalton Transactions*, pages 2995–3002, 2004.

[46] Alain P. Roth, James B. Webb, and Digby F. Williams. Band-gap narrowing in heavily defect-doped zno. *Phys. Rev. B*, 25:7836–7839, Jun 1982.

[47] Takenori Yamamoto and Takahisa Ohno. Screened hybrid density functional study on Nb- and Ta-doped TiO_2. *Physical Review B*, 85(3):033104, January 2012.

[48] N Mott. On metal-insulator transitions. *Journal of Solid State Chemistry*, 88(1):5–7, September 1990.

[49] Hiroyuki Fujiwara and Michio Kondo. Effects of carrier concentration on the dielectric function of ZnO : Ga and In 2 O 3 : Sn studied by spectroscopic ellipsometry : Analysis of free-carrier and band-edge absorption. *Physical Review B*, 71:075109, 2005.

[50] K Ellmer. Resistivity of polycrystalline zinc oxide films: current status and physical limit. *Journal of Physics D: Applied Physics*, 34:3097–3108, 2001.

[51] T. Makino, Y. Segawa, a. Tsukazaki, a. Ohtomo, and M. Kawasaki. Electron transport in ZnO thin films. *Applied Physics Letters*, 87(2):022101, 2005.

[52] J Steinhauser, S Faÿ, N Oliveira, et al. Electrical transport in boron doped polycrystalline zinc oxide thin films. *Physica status solidi (a)*, 1987(8):1983 – 1987, 2008.

[53] T. Makino, Y. Segawa, a. Tsukazaki, a. Ohtomo, and M. Kawasaki. Majority-carrier mobilities in undoped andn -type doped ZnO epitaxial layers. *Physica Status Solidi (C)*, 3(4):956–959, March 2006.

[54] J. R. Bellingham, W. a. Phillips, C. J. Adkins, and Madingley Road. Intrinsic performance limits in transparent conducting oxides. *Journal of Materials Sciences Letters*, 11(5):263–265, 1992.

[55] David S Ginley, Hideo Hosono, and David C (editors) Paine. *Handbook of Transparent Conductors*. Springer, New York, NY, USA, 2011.

[56] Klaus Ellmer. Past achievements and future challenges in the development of optically transparent electrodes. *Nature Photonics*, 6(12):809–817, November 2012.

[57] Alan E Delahoy and Sheyu Guo. Transparent Conducting Oxides for Photovoltaics. In A. Luque and S. Hegedus, editors, *Handbook of Photovoltaic Science and Engineering*, Hoboken, NJ, USA, 2011. John Wiley & Sons, Ltd.

[58] Yuzo Shigesato, Satoru Takaki, and Takeshi Haranoh. Electrical and structural properties of low resistivity tin-doped indium oxide films. *Journal of Applied Physics*, 71(7):3356, 1992.

[59] A. Suzuki, T. Matsushita, T. Aoki, Y. Yoneyama, and M. Okuda. Pulsed Laser Deposition of Transparent Conducting Indium Tin Oxide Films in Magnetic Field Perpendicular to Plume. *Japanese Journal of Applied Physics*, 40:401, April 2001.

[60] H Agura. Low resistivity transparent conducting Al-doped ZnO films prepared by pulsed laser deposition. *Thin Solid Films*, 445(2):263–267, December 2003.

[61] P.K Song, M Watanabe, M Kon, a Mitsui, and Y Shigesato. Electrical and optical properties of gallium-doped zinc oxide films deposited by dc magnetron sputtering. *Thin Solid Films*, 411(1):82–86, May 2002.

[62] V Assunção, E Fortunato, A Marques, et al. Influence of the deposition pressure on the properties of transparent and conductive ZnO: Ga thin-film produced by r.f. sputtering at room temperature. *Thin Solid Films*, 427:401–405, 2003.

[63] Bo-Huei Liao, Chien-Cheng Kuo, Pin-Jen Chen, and Cheng-Chung Lee. Fluorine-doped tin oxide films grown by pulsed direct current magnetron sputtering with an Sn target. *Applied optics*, 50(9):C106–10, March 2011.

[64] Robert Kykyneshi, Jin Zeng, and David P. Cann. Transparent Conducting Oxides based on Tin Oxide. In David S. Ginley, Hideo Hosono, and David C. Paine, editors, *Handbook of Transparent Conductors*, New York, NY, USA, 2011. Springer.

[65] J. Wienke and a.S. Booij. ZnO:In deposition by spray pyrolysis - Influence of the growth conditions on the electrical and optical properties. *Thin Solid Films*, 516(14):4508–4512, May 2008.

[66] P Nunes, E Fortunato, P Tonello, et al. Effect of different dopant elements on the properties of ZnO thin films. *Vacuum*, 64(3-4):281–285, January 2002.

[67] Yutaka Sawada, Chikako Kobayashi, Shigeyuki Seki, and Hiroshi Funakubo. Highly-conducting indium tin oxide transparent films fabricated by spray CVD using ethanol solution of indium (III) chloride and tin (II) chloride. *Thin Solid Films*, 409(1):46–50, April 2002.

[68] P Nagels. Electronic Transport in Amorphous Semiconductors. *Topics of Applied Physics*, 36, 1985.

[69] Hideo Hosono. Transparent Amorphous Oxide Semiconductors for Flexible Electronics. In David S. Ginley, Hideo Hosono, and David C. Paine, editors, *Handbook of Transparent Conductors*, New York, NY, USA, 2011. Springer.

[70] David S. Ginley and John D. Perkins. Transparent Conductors. In David S. Ginley, Hideo Hosono, and David C. Paine, editors, *Handbook of Transparent Conductors*, New York, NY, USA, 2011. Springer.

[71] Robert L. Z. Hoye, Kevin P. Musselman, and Judith L. MacManus-Driscoll. Research Update: Doping ZnO and TiO2 for solar cells. *APL Materials*, 1(6):060701, 2013.

[72] Taro Hitosugi, Yutaka Furubayashi, Atsuki Ueda, et al. Ta-doped Anatase TiO 2 Epitaxial Film as Transparent Conducting Oxide. *Japanese Journal of Applied Physics*, 44(No. 34):L1063–L1065, August 2005.

[73] Thomas O Mason, Steven P Harvey, and Kenneth R. Poeppelmeier. Ternary and Multinary Materials: Crystal/Defect Structure-Property Relationships. In David S. Ginley, Hideo Hosono, and David C. Paine, editors, *Handbook of Transparent Conductors*, New York, NY, USA, 2011. Springer.

[74] Hideo Hosono. Non conventional Materials. In David S. Ginley, Hideo Hosono, and David C. Paine, editors, *Handbook of Transparent Conductors*, New York, NY, USA, 2011. Springer.

[75] Teresa M. Barnes, Matthew O. Reese, Jeremy D. Bergeson, et al. Comparing the Fundamental Physics and Device Performance of Transparent, Conductive Nanostructured Networks with Conventional Transparent Conducting Oxides. *Advanced Energy Materials*, 2(3):353–360, March 2012.

[76] Sukang Bae, Hyeongkeun Kim, Youngbin Lee, et al. Roll-to-roll production of 30-inch graphene films for transparent electrodes. *Nature nanotechnology*, 5(8):574–8, August 2010.

[77] H. Ohta. Junctions. In David S. Ginley, Hideo Hosono, and David C. Paine, editors, *Handbook of Transparent Conductors*, New York, NY, USA, 2011. Springer.

[78] Atsushi Kudo, Hiroshi Yanagi, Hideo Hosono, and Hiroshi Kawazoe. $SrCu_2O_2$: A p-type conductive oxide with wide band gap. *Applied Physics Letters*, 73(2):220, 1998.

[79] E Fortunato, P Barquinha, and R Martins. Oxide semiconductor thin-film transistors: a review of recent advances. *Advanced Materials*, 24(22):2945–86, June 2012.

[80] Geoffroy Hautier, Anna Miglio, Gerbrand Ceder, Gian-Marco Rignanese, and Xavier Gonze. Identification and design principles of low hole effective mass p-type transparent conducting oxides. *Nature communications*, 4:2292, January 2013.

[81] Takaya Akashi, Tsuyoshi Itoh, Itaru Gunjishima, Hiroshi Masumoto, and Takashi Goto. Thermoelectric Properties of Hot-pressed Boron Suboxide (B6O). *Materials Transactions*, 43(7):1719–1723, 2002.

[82] JA Selvan and AE Delahoy. A new light trapping TCO for nc-Si: H solar cells. *Solar energy materials and solar cells*, 90:3371–3376, 2006.

[83] Hairen Tan, Rudi Santbergen, Arno H M Smets, and Miro Zeman. Plasmonic light trapping in thin-film silicon solar cells with improved self-assembled silver nanoparticles. *Nano letters*, 12(8):4070–6, August 2012.

[84] JD Beach and BE McCandless. Materials challenges for CdTe and CuInSe2 photovoltaics. *MRS bulletin*, 32(March), 2007.

[85] Michael Grätzel. Recent advances in sensitized mesoscopic solar cells. *Accounts of chemical research*, 42(11):1788–98, November 2009.

[86] Dana C. Olson and David S. Ginley. Nanostructured TCOs (ZnO, TiO_2 and Beyond). In David S. Ginley, Hideo Hosono, and David C. Paine, editors, *Handbook of Transparent Conductors*, New York, NY, USA, 2011. Springer.

[87] Nafiseh Memarian, Isabella Concina, Antonio Braga, et al. Hierarchically assembled ZnO nanocrystallites for high-efficiency dye-sensitized solar cells. *Angewandte Chemie (International ed. in English)*, 50(51):12321–5, December 2011.

[88] F Sauvage, F Di Fonzo, a Li Bassi, et al. Hierarchical TiO2 photoanode for dye-sensitized solar cells. *Nano letters*, 10(7):2562–7, July 2010.

[89] Henry J. Snaith. Perovskites: The Emergence of a New Era for Low-Cost High-Efficiency Solar Cells. *Journal of Physical Chemistry Letters*, 4:3623, 2013.

[90] Klaus Ellmer and Andreas Klein. Zno and its applications. In Klaus Ellmer, Andreas Klein, and Bernd Rech, editors, *Transparent conductive zinc oxide - basics and applications in thin film solar cells*, Berlin, Germany, 2008. Springer Verlag.

[91] Ü Özgür, Ya I Alivov, C Liu, et al. A comprehensive review of ZnO materials and devices. *Journal of Applied Physics*, 98:1–103, 2005.

[92] G Sberveglieri, C Baratto, E Comini, et al. Synthesis and characterization of semiconducting nanowires for gas sensing. *Sensors and Actuators B: Chemical*, 121(1):208 – 213, 2007.

[93] E. M. C. Fortunato, P. M. C. Barquinha, a. C. M. B. G. Pimentel, et al. Fully Transparent ZnO Thin-Film Transistor Produced at Room Temperature. *Advanced Materials*, 17(5):590–594, March 2005.

[94] Safa Shoaee, Joe Briscoe, James R Durrant, and Steve Dunn. Acoustic enhancement of polymer/ZnO nanorod photovoltaic device performance. *Advanced materials*, 26(2):263–8, January 2014.

[95] Dirk Vogel, Peter Krüger, and Johannes Pollmann. Self-interaction and relaxation-corrected pseudopotentials for II-VI semiconductors. *Physical Review B*, 54(8):5495–5511, 1996.

[96] Peter Schroer, Peter Kriiger, and Johannes Pollmann. First-principles calculation of the electronic structure in the wurtzitic semiconductors ZnO and ZnS. *Physical Review B*, 47(12):6971–6980, 1993.

[97] Stephan Lany and Alex Zunger. Comment on Intrinsic n-type Behavior in Transparent Conducting Oxides: A Comparative Hybrid-Functional Study of In2O3, SnO2, and ZnO. *Physical Review Letters*, 106(6):069601, February 2011.

[98] Péter Ágoston, Karsten Albe, Risto M. Nieminen, and Martti J. Puska. Ágoston et al. Reply:. *Physical Review Letters*, 106(6):069602, February 2011.

[99] D. C. Look, J. W. Hemsky, and J. R. Sizelove. Residual Native Shallow Donor in ZnO. *Physical Review Letters*, 82:2552–2555, Mar 1999.

[100] D C Look, G C Farlow, Pakpoom Reunchan, et al. Evidence for Native-Defect Donors in n -Type ZnO. *Physical Review Letters*, 225502(November):1–4, 2005.

[101] K. Ellmer. Transparent Conductive Zinc Oxide and its Derivatives. In David S. Ginley, Hideo Hosono, and David C. Paine, editors, *Handbook of Transparent Conductors*, New York, NY, USA, 2011. Springer.

[102] Hajime Wagata, Naoki Ohashi, Ken-ichi Katsumata, et al. An aqueous solution process and subsequent UV treatment for highly transparent conductive ZnO films. *Journal of Materials Chemistry*, 22(38):20706, 2012.

[103] Klaus Ellmer. Electrical properties. In Klaus Ellmer, Andreas Klein, and Bernd Rech, editors, *Transparent conductive zinc oxide - basics and applications in thin film solar cells*, Berlin, Germany, 2008. Springer Verlag.

[104] J. Clatot, G. Campet, a. Zeinert, et al. Low temperature Si doped ZnO thin films for transparent conducting oxides. *Solar Energy Materials and Solar Cells*, 95(8):2357–2362, August 2011.

[105] S Takata, T Minami, and H Nanto. The stability of aluminium-doped ZnO transparent electrodes fabricated by sputtering. *Thin Solid Films*, 135(2):183 – 187, 1986.

[106] F. Ruske, M. Roczen, K. Lee, et al. Improved electrical transport in Al-doped zinc oxide by thermal treatment. *Journal of Applied Physics*, 107(1):013708, 2010.

[107] Klaus Ellmer. Electrical transport parameters of heavily-doped zinc oxide and zinc magnesium oxide single and multilayer films heteroepitaxially grown on oxide single crystals. *Thin Solid Films*, 496:104–111, 2006.

[108] Hideaki Agura, Akio Suzuki, Tatsuhiko Matsushita, Takanori Aoki, and Masahiro Okuda. Low resistivity transparent conducting Al-doped ZnO films prepared by pulsed laser deposition. *Thin Solid Films*, 445(2):263–267, December 2003.

[109] Akio Suzuki, Masataka Nakamura, Ryota Michihata, and Takanaori Aoki. Ultrathin Al-doped transparent conducting zinc oxide films fabricated by pulsed laser deposition. *Thin Solid Films*, 517(4):1478–1481, 2008.

[110] Hanna Saarenpää, Tapio Niemi, Antti Tukiainen, Helge Lemmetyinen, and Nikolai Tkachenko. Aluminum doped zinc oxide films grown by atomic layer deposition for organic photovoltaic devices. *Solar Energy Materials and Solar Cells*, 94:1379–1383, April 2010.

[111] Qifeng Zhang, Christopher S Dandeneau, Xiaoyuan Zhou, and Guozhong Cao. ZnO Nanostructures for Dye Sensitized Solar Cells. *Advanced Materials*, 21:4087–4108, 2009.

[112] J Hüpkes, J Müller, and B Rech. Texture etched zno:al for silicon thin film solar cells. In Klaus Ellmer, Andreas Klein, and Bernd Rech, editors, *Transparent conductive zinc oxide - basics and applications in thin film solar cells*, Berlin, Germany, 2008. Springer Verlag.

[113] Jing Yu Lao, Jian Guo Wen, and Zhi Feng Ren. Hierarchical ZnO Nanostructures. *Nano Letters*, 2(11):1287, 2002.

[114] E. Comini, C. Baratto, G. Faglia, et al. Quasi-one dimensional metal oxide semiconductors: Preparation, characterization and application as chemical sensors. *Progress in Materials Science*, 54(1):1–67, January 2009.

[115] Seung H Ko, Daeho Lee, Hyun W Kang, et al. Nanoforest of Hydrothermally Grown Hierarchical ZnO Nanowires for a High Efficiency Dye-Sensitized Solar Cell. *Nano Letters*, 11:666–671, 2011.

[116] T. Holloway, R. Mundle, H. Dondapati, et al. Al-doped ZnO aligned nanorod arrays for opto-electronic and sensor applications. *Proceedings of SPIE*, 8344:83440A–83440A–10, 2012.

[117] D Calestani, F Pattini, F Bissoli, et al. Solution-free and catalyst-free synthesis of ZnO-based nanostructured TCOs by PED and vapor phase growth techniques. *Nanotechnology*, 23(19):194008, May 2012.

[118] Cheng-Yu Wang, Chuan-Pu Liu, Hui-Wen Shen, et al. Growth and Valence Excitations of ZnO:M(Al, In, Sn) Hierarchical Nanostructures. *The Journal of Physical Chemistry C*, 114(42):18031–18036, October 2010.

[119] Ye Sun, Katherine E Addison, and Michael N R Ashfold. Growth of arrays of Al-doped ZnO nanocones by pulsed laser deposition. *Nanotechnology*, 18(49):495601, December 2007.

[120] R Könenkamp, L Dloczik, K Ernst, and C Olesch. Nano-structures for solar cells with extremely thin absorbers. *Physica E*, 14:219–223, 2002.

[121] L. Vayssieres. Growth of Arrayed Nanorods and Nanowires of ZnO from Aqueous Solutions. *Advanced Materials*, 15(5):464–466, March 2003.

[122] JM Lackner. Industrially-styled room-temperature pulsed laser deposition of ZnO: Al films. *Thin Solid Films*, 494:302 – 306, 2006.

[123] J. Clatot, G. Campet, a. Zeinert, C. Labrugère, and a. Rougier. Room temperature transparent conducting oxides based on zinc oxide thin films. *Applied Surface Science*, 257(12):5181–5184, April 2011.

[124] Weifeng Yang, Zhengyun Wu, Zhuguang Liu, et al. Room temperature deposition of Al-doped ZnO films on quartz substrates by radio-frequency magnetron sputtering and effects of thermal annealing. *Thin Solid Films*, 519(1):31–36, October 2010.

[125] E.V. Johnson, P. Prod'homme, C. Boniface, et al. Excimer laser annealing and chemical texturing of ZnO:Al sputtered at room temperature for photovoltaic applications. *Solar Energy Materials and Solar Cells*, 95(10):2823–2830, October 2011.

[126] D Dellasega, A Facibeni, F Di Fonzo, et al. Nanostructured Ag 4 O 4 films with enhanced antibacterial activity. *Nanotechnology*, 19:475602, 2008.

[127] Doo-Hyun Ko, John R. Tumbleston, Abay Gadisa, et al. Light-trapping nano-structures in organic photovoltaic cells. *Journal of Materials Chemistry*, 21(41):16293, 2011.

[128] Patrick Boland, Keejoo Lee, and Gon Namkoong. Device optimization in PCPDTBT:PCBM plastic solar cells. *Solar Energy Materials and Solar Cells*, 94(5):915–920, May 2010.

[129] S Nicolay, M Despeisse, F Haug, and C Ballif. Control of LPCVD ZnO growth modes for improved light trapping in thin film silicon solar cells. *Solar Energy Materials and Solar Cells*, 95(3):1031–1034, 2011.

[130] Lars Müller-Meskamp, Yong Hyun Kim, Teja Roch, et al. Efficiency Enhancement of Organic Solar Cells by Fabricating Periodic Surface Textures using Direct Laser Interference Patterning. *Advanced Materials*, 24(7):906–910, February 2012.

[131] Shih-Shou Lo, Chen-Yu Lin, and Der-Jun Jan. Transparent conductive oxide layer with monolayer closed-pack Al-doped ZnO spheres and their application to a-Si thin-film solar cells. *Optics letters*, 36(18):3678–80, September 2011.

[132] Qian Huang, Yang Liu, Susu Yang, Ying Zhao, and Xiaodan Zhang. Hydrogen mediated self-textured zinc oxide films for silicon thin film solar cells. *Solar Energy Materials and Solar Cells*, 103:134–139, August 2012.

[133] K Jäger, O Isabella, R a C M M van Swaaij, and M Zeman. Angular resolved scattering measurements of nano-textured substrates in a broad wavelength range. *Measurement Science and Technology*, 22(10):105601, October 2011.

[134] D.B. Chrisey and G.K. Hubler. *Pulsed laser deposition of thin films*. Wiley-interscience publication. J. Wiley, 1994.

[135] R Eason. *Pulsed Laser Deposition of Thin Films*. Wiley, Hoboken, NJ, USA, 2007.

[136] Carlo S Casari and Andrea Li Bassi. Pulsed Laser Deposition of Nanostructured Oxides: from Clusters to Functional Films. In William T Arkin,

editor, *Advances in Lasers and Optics Research*, volume 7, chapter 2, pages 65–100. Nova Science Publishers, Inc, Hauppage, NY, 2012.

[137] M Lorenz. PLD of ZnO films. In Klaus Ellmer, Andreas Klein, and Bernd Rech, editors, *Transparent conductive zinc oxide - basics and applications in thin film solar cells*, Berlin, Germany, 2008. Springer Verlag.

[138] Salvatore Amoruso, Bo Toftmann, and Jø rgen Schou. Thermalization of a UV laser ablation plume in a background gas: From a directed to a diffusionlike flow. *Physical Review E*, 69(5):1–6, May 2004.

[139] David B. Geohegan, Alex a. Puretzky, Gerd Duscher, and Stephen J. Pennycook. Time-resolved imaging of gas phase nanoparticle synthesis by laser ablation. *Applied Physics Letters*, 72(23):2987, 1998.

[140] L.J. Van der Pauw. A method of measuring specific resistivity and Hall effect of discs of arbitrary shape. *Philips Research Reports*, 13(1):1–9, 1958.

[141] J Tauc. Optical properties and electronic structure of amorphous Ge and Si. *Materials Research Bulletin*, 3:37–46, 1968.

[142] D Bruce Buchholz, Jun Liu, Tobin J Marks, Ming Zhang, and Robert P H Chang. Control and Characterization of the Structural, Electrical, and Optical Properties of Amorphous Zinc-Indium-Tin Oxide Thin Films. *ACS Applied Materials and Interfaces*, 1(10):2147–2153, 2009.

[143] Paolo Gondoni, Matteo Ghidelli, Fabio Di Fonzo, Andrea Li Bassi, and Carlo S Casari. Fabrication of nano-engineered transparent conducting oxides by pulsed laser deposition. *Journal of Visualized Experiments : JoVE*, (72):e50297, January 2013.

[144] P Gondoni, M Ghidelli, F Di Fonzo, et al. Structure-dependent optical and electrical transport properties of nanostructured Al-doped ZnO. *Nanotechnology*, 23:365706, 2012.

[145] P Gondoni, V Russo, C E Bottani, A Li Bassi, and C S Casari. Tuning Hierarchical Cluster Assembly in Pulsed Laser Deposition of Al-doped ZnO. *MRS Symposium Proceedings*, 1497, 2013.

[146] P. Gondoni, M. Ghidelli, F. Di Fonzo, et al. Structural and functional properties of Al:ZnO thin films grown by Pulsed Laser Deposition at room temperature. *Thin Solid Films*, 520(14):4707–4711, May 2012.

[147] V Russo, M Ghidelli, P Gondoni, C S Casari, and A Li Bassi. Multi-wavelength Raman scattering of nanostructured Al-doped zinc oxide. *Journal of Applied Physics*, 115:073508, 2014.

[148] P. Gondoni, M. Ghidelli, F. Di Fonzo, et al. Highly Performing Al:ZnO Thin Films Grown by Pulsed Laser Deposition at Room Temperature. *Nanoscience and Nanotechnology Letters*, 5(4):484–486, April 2013.

[149] M Gerosa and C E Bottani. Multiple light scattering and near-field effects in a fractal treelike ensemble of dielectric nanoparticles. *Phys. Rev. B*, 87:195312, May 2013.

[150] R Swanepoel. Determination of surface roughness and optical constants of inhomogeneous amorphous silicon films. *Journal of Physics E: Scientific Instruments*, 17:896, 1984.

[151] Z Qiao, C Agashe, and D Mergel. Dielectric modeling of transmittance spectra of thin ZnO:Al films. *Thin Solid Films*, 496(2):520–525, 2006.

[152] S Brehme, F Fenske, W Fuhs, et al. Free-carrier plasma resonance effects and electron transport in reactively sputtered degenerate ZnO : Al films. *Thin Solid Films*, 342:167–173, 1999.

[153] J. G. Lu, S. Fujita, T. Kawaharamura, et al. Carrier concentration dependence of band gap shift in n-type ZnO:Al films. *Journal of Applied Physics*, 101(8):083705, 2007.

[154] Bin-Zhong Z Dong, Hao Hu, Guo-Jia J Fang, et al. Comprehensive investigation of structural, electrical, and optical properties for ZnO:Al films deposited at different substrate temperature and oxygen ambient. *Journal of Applied Physics*, 103(7):073711, 2008.

[155] Nurul Islam, T B Ghosh, K L Chopra, and H N Acharya. XPS and X-ray diffraction studies of aluminum-doped zinc oxide transparent conducting films. *Thin Solid Films*, 280:20–25, 1996.

[156] J.J. Yeh. *Atomic Calculation of Photoionization Cross-Sections and Asymmetry Parameters*. Gordon and Breach Sciene Publishers, 1993.

[157] J.J. Yeh and I. Lindau. Atomic subshell photoionization cross sections and asymmetry parameters: $1 \leq z \leq 103$. *Atomic Data and Nuclear Data Tables*, 32:1–155.

[158] David R Penn. Quantitative chemical analysis by ESCA. *Journal of Electron Spectroscopy and Related Phenomena*, 9:29–40, 1976.

[159] Mirjam Theelen, Twan Boumans, Felix Stegeman, et al. Physical and chemical degradation behavior of sputtered aluminum doped zinc oxide layers for Cu (In , Ga) Se 2 solar cells. *Thin Solid Films*, 550:530–540, 2014.

[160] Mandar M Shirolkar, Changshan Hao, Shiliu Yin, et al. behavior of dilutely aluminum doped ZnO thin film Influence of surface null potential on nonvolatile bistable resistive switching memory behavior of dilutely aluminum doped ZnO thin film. *Applied Physics Letters*, 243501, 2013.

[161] Shanshan Peng, Fei Zhuge, Xinxin Chen, et al. memory Mechanism for resistive switching in an oxide-based electrochemical metallization memory. *Applied Physics Letters*, 072101, 2012.

[162] Fauzia Jabeen, Silvia Rubini, Faustino Martelli, et al. Contactless monitoring of the diameter-dependent conductivity of GaAs nanowires. *Nano Research*, 3(10):706–713, September 2010.

[163] P Gondoni, P Mazzolini, V Russo, et al. Enhancing light harvesting by hierarchical functionally graded transparent conducting Al-doped ZnO nano- and mesoarchitectures. *Solar Energy Materials and Solar Cells*, 128:248–253, 2014.

[164] P Gondoni, P Mazzolini, A Pillado Pérez, et al. Morphology-driven electrical and optical properties in graded hierarchical transparent conducting Al:ZnO. *Materials Research Society Symposium Proceedings*, 1699E, in press, 2014.

[165] G Grancini, M Maiuri, D Fazzi, et al. Hot exciton dissociation in polymer solar cells. *Nature materials*, 12(1):29–33, January 2013.

[166] Sarah R. Cowan, Natalie Banerji, Wei Lin Leong, and Alan J. Heeger. Charge Formation, Recombination, and Sweep-Out Dynamics in Organic Solar Cells. *Advanced Functional Materials*, 22(6):1116–1128, March 2012.